

國立臺灣大學工學院應用力學研究所  
博士論文

Institute of Applied Mechanics

College of Engineering

National Taiwan University

Doctoral Dissertation



研製分佈式感應子及壓電致動器應用之光壓電材料  
Developing Optopiezoelectric Materials for Distributed  
Sensors and Piezoelectric Actuators

張雯琪

Wen-Chi Chang

指導教授：李世光 博士

王安邦 博士

Advisor: Chih-Kung Lee, Ph.D.

An-Bang Wang, Ph.D.

中華民國 104 年 7 月

July, 2015





國立臺灣大學博士學位論文  
口試委員會審定書

研製分佈式感應子及壓電致動器應用之光壓  
電材料

Developing Optopiezoelectric Materials for  
Distributed Sensors and Piezoelectric Actuators

本論文係張雯琪君（學號：F98543004）在國立臺灣大學應用力學研究所完成之博士學位論文，於民國 104 年 7 月 8 日承下列考試委員審查通過及口試及格，特此證明

口試委員：

李世光 李世光 王安邦 王安邦  
(指導教授)

謝宗霖 謝宗霖

林致廷 林致廷


許聿翔 許聿翔

饒達仁 饒達仁

謝志文 謝志文

所長 張家歐 張家歐

## 謝誌



過去六年來，每次讀著學長姊、同學與學弟妹的畢業論文謝誌，不斷想像輪到自己寫致謝時的心情！首先我由衷地感謝我的指導教授李世光老師與王安邦老師。每當我面對實驗或研究生涯規畫的煩惱，不知該如何解決，李老師總會提供許多寶貴意見使我覺得豁然開朗，讓我逐漸成為一位對光機電系統有更深體驗的學生。另外，感謝王老師時常關心我的研究生活，而老師身體力行的學者精神，更讓我學習做研究的態度。接著，我要感謝團隊中的林致廷老師、吳文中老師與許聿翔老師，謝謝您們時常幫助我解決實驗問題，才使我逐步完成本篇論文。而我也要感謝口試委員謝宗霖教授、饒達仁教授與謝志文博士，感謝您們對本篇論文給予良好建議。

接著，我要感謝文清學長、育諺學長與順區學長，學長們總是 open-minded 告訴我如何規畫實驗與研究生活，畢業後仍時常關心我的狀況，讓我備感溫馨。我也要謝謝實驗室一同奮鬥的 Bio 組伙伴宜靜、佩紋、柏翰、齡雅、信互、佳縉、存勗等，大家一起為實驗努力、討論的經驗，將是我永遠美好的回憶。此外，也感謝在 433 大家庭的好朋友仁傑、承義、建君、富程、泓緯、則翔、冠宇、君恬、淳惠與佩漪學姊等，以及工科 109 的立仁、欣潔、育正與俊良學長等，因為有你們大家的陪伴，我的研究生生活也增添許多快樂的氣氛。

最後要感謝我的家人與甫諭，感謝你們一路支持，本論文也才得以完成，謹以此文獻給每位曾經幫助我的人！

民國 104 年 7 月

## 中文摘要



微操控技術於近年來蓬勃發展於微機電設備、生物晶片以及微流體系統。自十九世紀末，原子力學顯微鏡、光鉗與磁鉗被實現於操控單一細胞或原子；熱泳、介電泳與介電濕潤等非接觸式操控技術也相繼被提出，來提高控制待測物的力量與效率，並且降低傷害樣品的風險。近年來，許多感光複合材料相繼被開發並應用於操控技術中，使用快速變換的光照圖樣，改變晶片中局部電場或熱場，進而達成操控微物體的效果。然而，傳統的光調變技術，僅提供或感測奈米牛頓等級的力學場，故本論文提出光壓電複合材料，將光敏材料與壓電材料結合，藉由照光圖樣局部調變壓電的電場與力學場，並將驅動或感測的力學場數量級提升 $10^6$ 數量級。本論文於第三章，以直流偏壓 175 伏特驅動微流道系統中的壓電片，有效侷限蠕蟲運動範圍。於第四章，使用感光染料(spiropyran)/液晶複合壓電片(PZT)，研製光壓電懸臂樑致動器，探討其位移與頻率隨紫外光(365 nm,  $0.7 \text{ mW/cm}^2$ )照射而上升及偏移數十赫茲之機制。此外，發展光壓電感測器 P(VDF-TrFE)/TiOPc，提出摻入 TiOPc 濃度為 10%重量百分濃度，可使材料具有最佳光調變壓電的表現。並且於第五章，複合壓電 PZT 與 40% w. t. TiOPc/ 樹脂，研製量測誤差小於 10%的光壓電彎曲感測器，並驗證此感測器具有快速動態調變、反應效率佳、不影響待測物振動行為等優點，因此更能夠改善傳統力學感測器因佈點位置差異造成的誤差。本論文透過探討壓電片於流體中的效率、研製並了解光壓電致動器與感測器的表現，所取得的模擬、實驗及分析結果，將能作為未來創新光壓電或光壓電流體應用之參考。

關鍵字：蠕蟲侷限微流道、光壓電、光敏材料。





## Abstract

The micro-/ nano mechanical manipulation has been recently progressively developed for micromechanical equipment, biochips, and microfluidic devices. Since the end of the 19th century, the atomic force microscopy, optical tweezers, and magnetic tweezers have been proposed to control single cell or atom. Some indirect control methods, such as optothermal mechanism, opto-electrowetting (OEW) and optical dielectrophoresis (ODEP) techniques, provide us with larger force, better efficiency, and less damage on the objects. In these years, many optical sensitive composite materials are integrated into control systems; the electrical or thermal field can be modulated by light pattern for manipulating particles or droplets. However, these conventional optical control techniques deliver actuating or sensing force only in the nN range. In this dissertation, the optopiezoelectric actuator or sensor can modulate mN force by varying the distribution of the illuminated light pattern. In *Chapter 3*, a PZT actuator is triggered with 175 DC voltage in microfluidic device to efficiently trap living *C. elegans*. In *Chapter 4*, the optopiezoelectric cantilever beam actuator of spiropyran/ liquid crystal- PZT performs UV (365 nm, 0.7 mW/cm<sup>2</sup>) modulated amplitude with few tens (Hz) frequency shift. And the P(VDF-TrFE)/ TiOPc optopiezoelectric sensors are fabricated and developed with an optimal 10 % w.t. TiOPc concentration. In traditional point bending sensor, the signal error is closely related to its position. Thus in *Chapter 5*, a full field optopiezoelectric bending sensor, PZT- 40% w.t. TiOPc/ resin, performs less than 10% error with numerical analysis. Without effects on the host structure, it has fast and easy modulation capability by using spatially distributed light illumination patterns. Overall, this thesis discusses the piezoelectric effect in

microfluidics, developing and understanding the optopiezoelectric performance. We expect the simulation, experimental and analytical results can provide some evidences and references for future innovative optopiezoelectric or optopiezoelectric fluidics application.

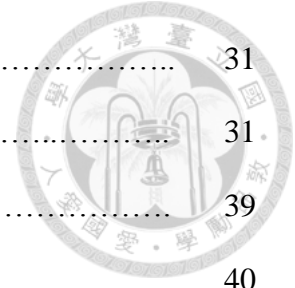
Keywords: Worm immobilization microfluidics, Optopiezoelectric, Photosensitive material.



# Contents

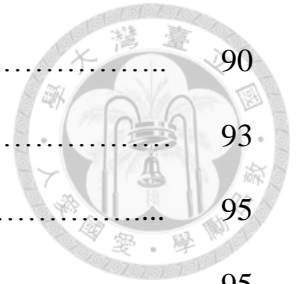


口試委員會審定書	#
誌謝	i
中文摘要	ii
Abstract	iv
Contents	vi
List of figures	ix
List of tables	xvi
<b>Chapter 1 Introduction</b> .....	1
1.1 Micro-/ nano mechanical manipulation .....	1
1.2 Optical manipulation for small objects .....	3
1.3 Piezoelectric manipulation and control system .....	11
1.4 Optopiezoelectric control system .....	15
1.5 Motivation and purpose .....	17
<b>Chapter 2 Material</b> .....	19
2.1 Piezoelectric material .....	19
2.1.1 Lead Zirconium Titanate (PZT) .....	19
2.1.2 Piezoelectric polymer .....	20
2.2 Photoconductive material .....	24
2.2.1 Spiropyran .....	24
2.2.2 Titanyl Phthalocyanine (TiOPc) .....	26
<b>Chapter 3 A living worm trapper by PZT actuator</b> .....	28
3.1 Introduction .....	28



3.2	Theory .....	31
3.2.1	A linear piezoelectric thin plate actuator .....	31
3.2.2	Laplace pressure .....	39
3.3	Simulation .....	40
3.4	Device fabrication .....	50
3.5	Experimental results .....	51
3.6	Discussion and future work .....	54
<b>Chapter 4</b>	<b>Optopiezoelectric material .....</b>	<b>55</b>
4.1	Optopiezoelectric actuator .....	56
4.1.1	Experimental setup .....	56
4.1.2	Results .....	60
4.1.3	Discussion .....	63
4.2	Optopiezoelectric sensor .....	65
4.2.1	Material and film preparation .....	66
4.2.2	Characterization methods .....	67
4.2.3	Physical properties .....	68
4.2.4	Sensing performance .....	79
4.2.5	Discussion .....	82
<b>Chapter 5</b>	<b>Optopiezoelectric bending sensor .....</b>	<b>83</b>
5.1	Device fabrication and experimental setup .....	83
5.2	Experimental results .....	86
5.2.1	Material characteristics .....	86
5.2.2	Bending sensor .....	87

5.3	Numerical calculation and curve fitting .....	90
5.4	Discussion .....	93
<b>Chapter 6</b>	<b>Conclusion and future work .....</b>	<b>95</b>
6.1	Conclusion .....	95
6.2	Future work .....	96
<b>Reference</b>	.....	<b>98</b>
<b>List of publications</b>	.....	<b>107</b>



## List of figures

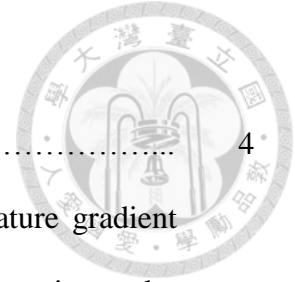
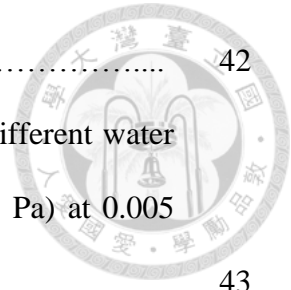


Figure 1-1.	Thermocapillary mechanism of to push the droplet. ....	4
Figure 1-2.	(a) The 1.53 mm radius bubble migration with temperature gradient $G=2.77$ K/ mm [19]. (b) The bubbles aggregation experiment by Hiroki Kasumi <i>et al.</i> [21]. ....	4
Figure 1-3.	(a) Schematic processes of laser excited bubble cavitation [22]. (b) Schematic of the cell sorter within few microseconds response [23]. (c) The localized cell concentrator by acoustically activating the optothermally bubbles [24]. ....	5
Figure 1-4.	The scheme of (a) a typical OEW device [29], (b) open optoelectrowetting (o-OEW) device [34], and (c) Single-sided continuous optoelectrowetting (SCOEW) working principle with its equivalent circuit model [35]. ....	7
Figure 1-5.	(a) The ODEP device for massive and parallel particles manipulation [28]. (b) The scheme of ODEP mechanism [38]. ....	9
Figure 1-6.	The frequency response figure (not to scale) of OEW and ODEP [41]. ....	10
Figure 1-7.	Piezoelectric effect in microfluidic device for (a) pumping [46], (b) sorting [47], (c) mixing [49], and (d) pressure monitoring [54]. ....	11
Figure 1-8.	Distributed piezoelectric actuators or sensors for vibration controlling systems. ....	14
Figure 1-9.	Light modulated optopiezoelectric controlling system. ....	16
Figure 1-10.	Overview of optical actuators and sensors for mechanical system. ....	18

Figure 2-1.	The working function of positive and converse piezoelectric effect. ....	20
Figure 2-2.	Molecular conformations and unit cells of the two common polymorphs of PVDF [86]. .....	22
Figure 2-3.	Schematic of random crystal lamellae in PVDF polymer. ....	22
Figure 2-4.	Schematic structure of the molecule chain of P(VDF-TrFE) copolymer in all-trans conformation with a ratio of VDF and TrFE of 75 : 25.....	23
Figure 2-5.	The spiropyran chemical structure and some related applications. ....	24
Figure 2-6.	The physical properties of titanyl phthalocyanine (TiOPc). ....	26
Figure 2-7.	Operation principle of the light-induced electric field for small particles manipulation by Shih-Mo Yang <i>et al.</i> [107]. ....	27
Figure 3-1.	The worm image [113]. ....	28
Figure 3-2.	Methods for worm immobilization. ....	30
Figure 3-3.	The scheme of the living worm trapper with PZT actuator. ....	31
Figure 3-4.	The relationship between stress, strain, electric field, and electric displacement. ....	33
Figure 3-5.	(a) The deformation of a buzzer with a DC voltage, and (b) the single layer piezoelectric actuator. ....	35
Figure 3-6.	The unimorph piezoelectric plate before and after deformation. ....	38
Figure 3-7.	Interface between two immiscible fluids. ....	39
Figure 3-8.	The x- and y- directional velocities, (a) $u$ and (b) $v$ , when the oil bulges expand from inlet pressure 103500 Pa at time=0.005s. ....	41
Figure 3-9.	The volume fraction of water and oil bulges with different oil inlet pressures (103100 Pa, 103500 Pa, 103900 Pa, 104300 Pa) at 0.005	

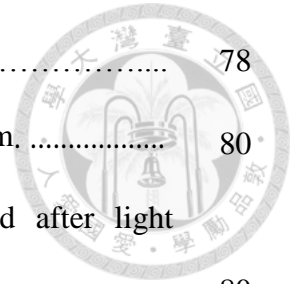


second. ....	42
Figure 3-10. The volume fraction of water and FC-43 droplets with different water inlet pressures (102700, 103500 Pa, 104300 Pa, 105100 Pa) at 0.005 second. ....	43
Figure 3-11. (a) The structure of the $\pi$ -channel structure. (b) A real case of an extremely large bubble blocking the water channel due to Laplace pressure. ....	44
Figure 3-12. The deformation measurement from laser vibrometer (Keyence, LK-H080). ....	45
Figure 3-13. The x-directional velocity simulation of (a) the donut structure and (c) the fingers-donut structure with 150 $\mu$ m channel height. The water is static, and the oil inlet pressure is 261300 Pa. Figure (b) and (d) are the photos with water droplet at the bottom in the donut and 45 $^\circ$ fingers-donut structure, respectively. ....	45
Figure 3-14. (a) The flow direction in the donut. (b)~(f) The pushing flow velocity of the donut structure from 0.001 s to 0.005 s. ....	47
Figure 3-15. The flow direction in the donut. And the pushing flow x-directional velocity of the 30 $^\circ$ , 45 $^\circ$ , and 60 $^\circ$ fingers-donut structures from 0.001 s to 0.005 s. ....	48
Figure 3-16. The comparison of the flow at the junctions of (a) 45 $^\circ$ and (b) 60 $^\circ$ fingers-donut structure at 0.005s. ....	49
Figure 3-17. (a) The fabrication process to make a microfluidic channel device with the fingers-donut structure. (b) Photos of the front and back view of the	

	fingers-donut structure with 150 $\mu\text{m}$ channel height. ....	51
Figure 3-18.	The steps of making oil/ water interface. (a) Let oil fill anywhere in the channel, and then (b) pumping water into the channel. (c) The schematic of the device and the initial oil/ water interface after blocking the oil inlet. ....	52
Figure 3-19.	Schematic of the worm that was (a) pumped by the pipette and swam into the donut structure and (b) trapped inside the water droplet. (c) The microscope image of a trapped living worm in a water droplet. ....	53
Figure 3-20.	The NMR spectrum of a tube of cured PDMS. ....	54
Figure 4-1.	The (a) double-layers and (b) single-layer photoconductive piezoelectric composite structures. ....	55
Figure 4-2.	(a) The cell structure and (b) the SP/ LC color changes with UV illumination. ....	56
Figure 4-3.	AVID system and its opto-mechanical setup. ....	58
Figure 4-4.	The spectra of SP/ LC with different light exposure. ....	60
Figure 4-5.	The photo of the optopiezoelectric actuator (SP/ LC- PZT) and its structure specification. ....	62
Figure 4-6.	The impedance of the optopiezoelectric actuator (SP/ LC- PZT) before and after UV illumination. The insert scheme is the equivalent circuit of (SP/ LC – PZT) [71]. ....	62
Figure 4-7.	The free-end deformation of the SP/ LC-PZT before and after UV illumination was measured by AVID. ....	63

Figure 4-8.	The scheme of the mechanism of a double-layers optopiezoelectric cantilever beam actuator. ....	64
Figure 4-9.	The deformation of a PZT buzzer with only right half electrode triggered with 20 DC voltage. (a) COMSOL simulation; (b) Electrical speckle pattern interferometry (ESPI) measurement. ....	65
Figure 4-10.	SEM images of (a) P(VDF-TrFE) and (b)-(d) P(VDF-TrFE)/ 0.5 wt%, 2.5 wt%, 5 wt% TiOPc powder surface morphology. (e) TiOPc powder. ....	69
Figure 4-11.	FTIR transmission spectra of P(VDF-TrFE) and P(VDF-TrFE)/ TiOPc composite film. ....	70
Figure 4-12.	XRD patterns of (a) P(VDF-TrFE) film before and after annealing. (b) P(VDF-TrFE) and P(VDF-TrFE)/ TiOPc composite film. ....	72
Figure 4-13.	Hysteresis loops of P(VDF-TrFE) and P(VDF-TrFE)/ TiOPc composite film. ....	73
Figure 4-14.	UV-Vis spectra of P(VDF-TrFE) and P(VDF-TrFE)/ TiOPc composite film. ....	75
Figure 4-15.	(a) Impedance variation of P(VDF-TrFE)/ TiOPc composite film. (b) Schematic of the stimulated electrons cause the impedance variation. ..	76
Figure 4-16.	The (a) resistance and (c) capacitance values of Sample 3 and Sample 6, as well as (b, d) their variation before and after illumination. ....	76
Figure 4-17.	Impedance of P(VDF-TrFE)/ 10% TiOPc at 750nm and 450nm. ....	78
Figure 4-18.	(a) The equivalent circuit of the composite. (b) Simulation and experimental results of the impedance before and after 750nm	



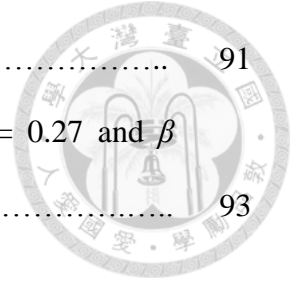


illumination. ....	78
Figure 4-19. Experimental set-up of photosensitive piezoelectric system. ....	80
Figure 4-20. Frequency spectra of the cantilever beam before and after light illumination. ....	80
Figure 4-21. (a) Obtained charges from the photosensitive composite piezoelectric sensor with white light illumination. (b) Scheme of charge cancellation after light illumination. ....	81
Figure 5-1. (a) The structure and (b) mechanism of PZT-TiOPc double layers optopiezoelectric sensor. ....	85
Figure 5-2. The experimental setup of an optopiezoelectric sensor for measuring bending angle. ....	85
Figure 5-3. The calculated impedance of a 40% TiOPc film from equation 5-1 with parameters in Table 5-1. ....	87
Figure 5-4. The free end deflection of the one-dimensional cantilever plate under different driving forces. ....	88
Figure 5-5. The illuminated beam from (a) 0~14 mm, (b) 0~28 mm, and (c) 0~42 mm. (d) The excitons of the static beam with light intensity (120 klux). (e) The charges of a vibration beam at 28.6 Hz, 0.22m N with light intensity (30 klux). ....	89
Figure 5-6. The obtained peak-to-peak charges coming from an Ag-electrode PZT beam at different shaking forces, and also charges from a PZT-TiOPc beam with different light illumination patterns. ....	89
Figure 5-7. The calculated charge at each section of a piezoelectric sensor	

(brass-PZT-Ag) ..... 91

Figure 5-8. The charge from measurement and expectation with  $\alpha=0.27$  and  $\beta$

$=0.55$ . ..... 93



## List of tables

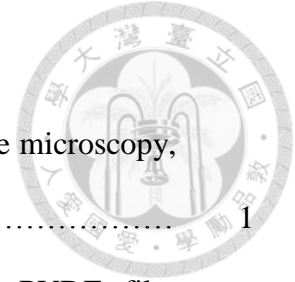
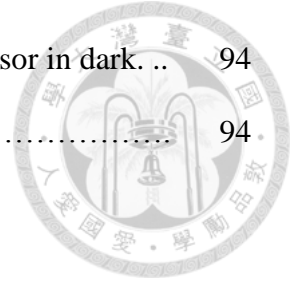


Table 1-1. Comparison of force spectroscopy techniques: atomic force microscopy, magnetic tweezers, and optical tweezers [2][3]. .....	1
Table 2-1. The piezoelectric properties comparison of PZT and PVDF film [81]. .....	21
Table 2-2. Comparisons of PVDF and P(VDF-TrFE) [81]. .....	23
Table 3-1. The parameters and variables in (equation 1~ 4). .....	32
Table 3-2. IEEE compact matrix notation [125]. .....	33
Table 3-3. Specifications and material properties of the $\pi$ -channels structure. ....	41
Table 4-1. Infrared active modes of P(VDF-TrFE) and TiOPc. ....	71
Table 4-2. Relationship between piezoelectric efficiency $d_{33}$ values and corona charging voltage of P(VDF-TrFE) and P(VDF-TrFE)/ TiOPc composite film. ....	74
Table 5-1. The resistor and capacitor changes of a 40% TiOPc in resin of different thicknesses [73]. .....	86
Table 5-2. Simulation of the ratio of the slope variation, surface potential at different sections. ....	91
Table 5-3. The calculated charge at each section from measured $Q_{0-42}$ with shaking forces 0.04 mN to 0.22 mN. ....	91
Table 5-4. The piezoelectric peak-to-peak charges of a general sensor and PZT-TiOPc sensor. ....	92
Table 5-5. The inversely calculated charges of a piezoelectric sensor from the measured charges of optopiezoelectric sensor. ....	94

Table 5-6. The measured surface potential of the optopiezoelectric sensor in dark. ... 94

Table 5-7. Comparison of the calculated and simulated bending slope. .... 94



# Chapter 1. Introduction



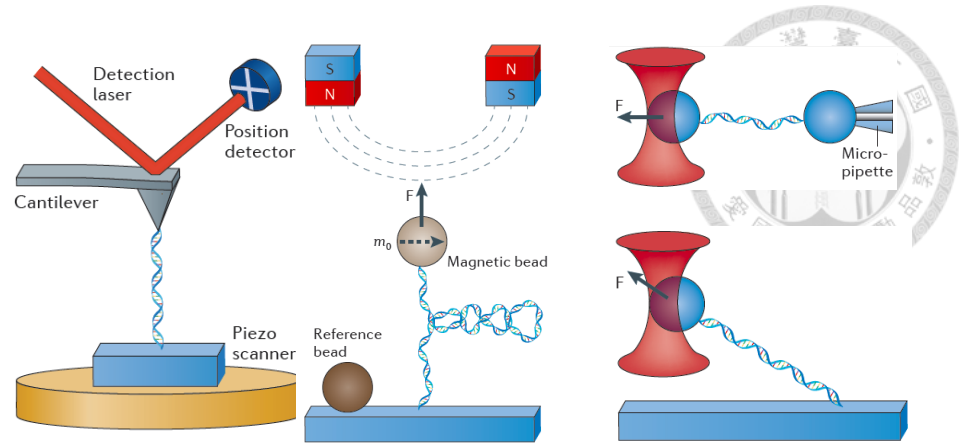
## 1.1 Micro-/nano mechanical manipulation

In recent years, mechanical manipulation has been widely developed in the bioengineering and microsystem fields to control small objects [1]. The most powerful and common techniques include atomic force microscopy (AFM), magnetic tweezers and optical tweezers (Table 1-1) [2].

Table 1-1. Comparison of force spectroscopy techniques: atomic force microscopy, magnetic tweezers, and optical tweezers [2][3].

	<b>Atomic force microscopy</b>	<b>Magnetic tweezers (electromagnetic tweezers)</b>	<b>Optical tweezers</b>
<b>Spatial resolution (nm)</b>	0.5~1	5~10 (2~10)	0.1~2
<b>Temporal resolution (s)</b>	$10^{-3}$	$10^{-1} \sim 10^{-2}$ ( $10^{-4}$ )	$10^{-4}$
<b>Force range (pN)</b>	$10 \sim 10^4$	$10^{-3} \sim 10^2$ ( $0.01 \sim 10^4$ )	$0.1 \sim 10^2$
<b>Displacement range (nm)</b>	$0.5 \sim 10^4$	$5 \sim 10^4$ ( $5 \sim 10^5$ )	$0.1 \sim 10^5$
<b>Probe size (<math>\mu\text{m}</math>)</b>	100~250	0.5~5	0.25~5
<b>Features</b>	High resolution imaging	Force clamp; Bead rotation	Low noise; drift dumbbell geometry
<b>Limitation</b>	Large high-stiffness probe; Large minimal force; Non specific	No manipulation (Force hysteresis)	Photo damage; Sample heating; Non specific

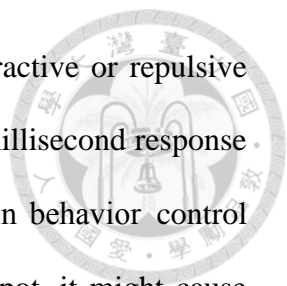
## Single-molecule manipulation



Atomic force microscopy (AFM), which was commercialized in 1998 [4], is the most commonly used scanning probe microscope (SPM). This near field technique is based on the van der Waals force between a sharp metal tip and the atoms on the sample surface. It can measure surface roughness in atomic scale resolution. In the past decades, it provides many applications in molecular metrology and biological sciences [5, 6, 7, 8]. However AFM measurements are generally at the high-force scale, its minimal force (10 pN) is too large, and it cannot provide 3D or long distance control [9].

By comparison, the magnetic tweezers, which can control the magnetic beads by permanent or electrical magnets, can measure and apply very low forces at fN. Its typical application is for cell manipulation and DNA topology [10, 11]. In addition, magnetic tweezers can also apply torques by rotating the magnetic fields [12, 13]. However, the magnetic tweezers are not as popular as AFM or optical tweezers. Because the permanent magnet configuration lacks the manipulation ability, and the electromagnet coils have significant hysteresis as a function of current [2].

Combining part of the advantages of AFM and magnetic tweezers, laser optical tweezers were proposed for particle manipulation in the 70s. Due to momentum



conservation, a highly focused laser beam provides a pico-newton attractive or repulsive force on the dielectric beads. It also gives 3D manipulation within a millisecond response for particle's nanometer transportation, ablation, and even electron spin behavior control [14, 15, 16, 17]. But its major drawback was the high power laser spot, it might cause photo damage on the specimens. Furthermore, the direct optical force can only generate very weak force (pico Newton range). To bypass some of the limitations mentioned above, some more effective optical mechanisms and other indirect optical control techniques such as optothermal mechanism and optoelectronic tweezers are widely adopted for particle and cell manipulation.

## **1.2 Optical manipulation for small objects**

Starting in 1980s, to overcome the force limitation of optical tweezers, an optothermal mechanism was found to provide a much larger force to allow faster droplet manipulation (cm/ s) [18]. One typical phenomenon is thermocapillary, which is based on the Marangoni effect (Figure 1-1). The local illuminated area has higher temperature and smaller surface stress. It means the droplet can be pumped toward the dark and cold side due to its larger surface stress. In this decade, thermocapillary can be used for fast transportation, trapping, and sorting the droplets in microfluidic studies (Figure 1-2) [19, 20, 21].

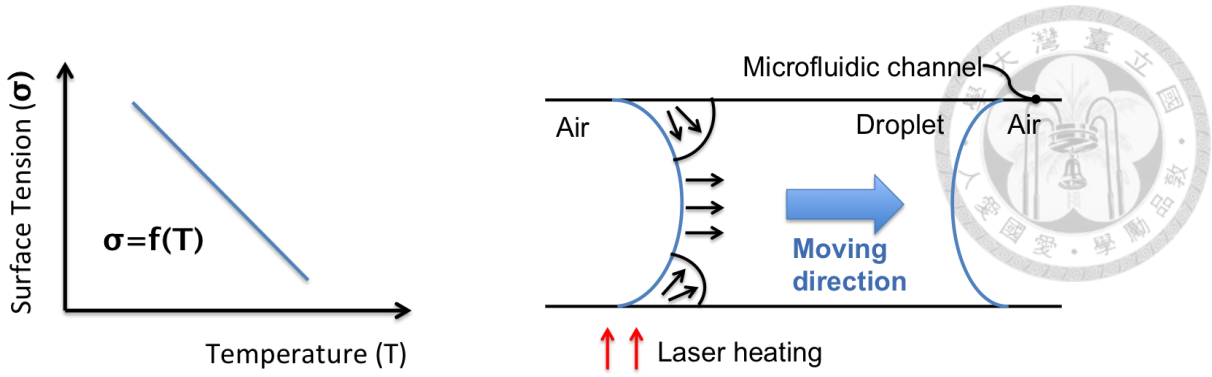
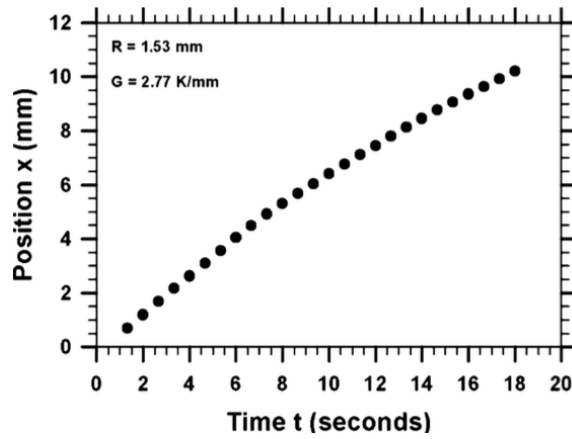


Figure 1-1. Thermocapillary mechanism of to push the droplet.

(a)



(b)

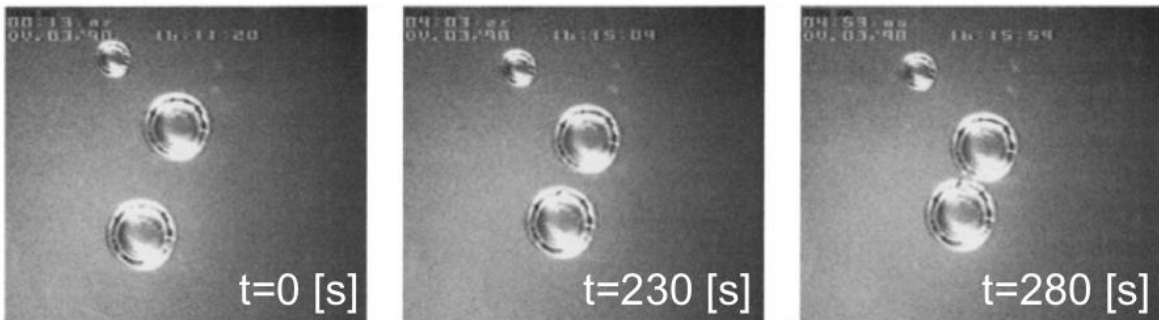
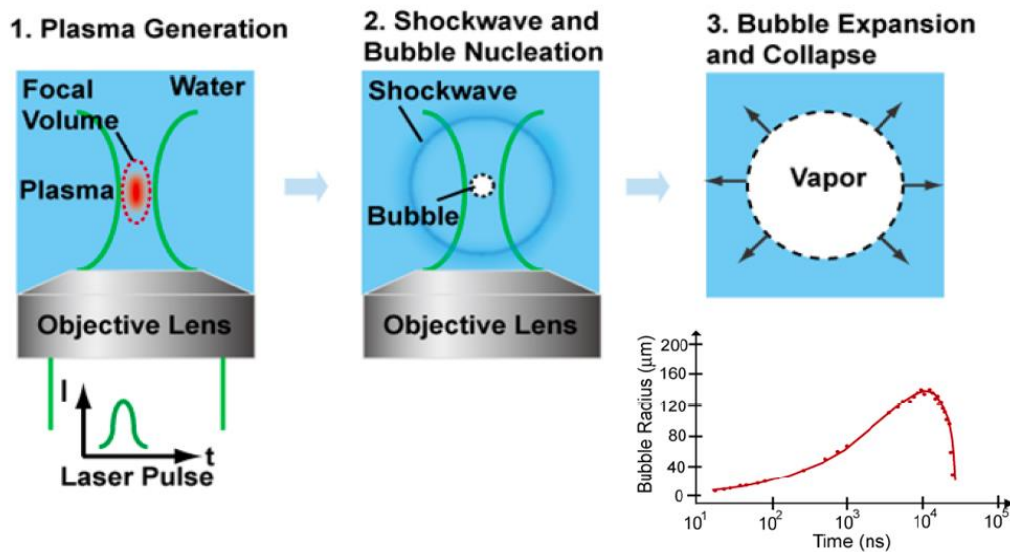


Figure 1-2. (a) The 1.53 mm radius bubble migration with temperature gradient  $G=2.77$  K/mm [19]. (b) The bubbles aggregation experiment by Hiroki Kasumi *et al.* [21].



However, the high power pulse laser still generates undesirable heat on the specimens. Another optothermal mechanism, optothermal cavitation bubbles, was proposed around 1990s. The high power pulse laser is also used as a heating source. This focused laser produces a rapidly expanding vapor bubble in the water through nonlinear optical absorption. And then the explosive evaporation occurs when a thin layer of liquid reaches the critical temperatures in a very short period of time (Figure 1-3a) [22]. Nowadays, this pressure impulse made from the thermal-bubble is widely applied in biological chips (Figure 1-3b, 1-3c) [23, 24, 25, 26].

(a)



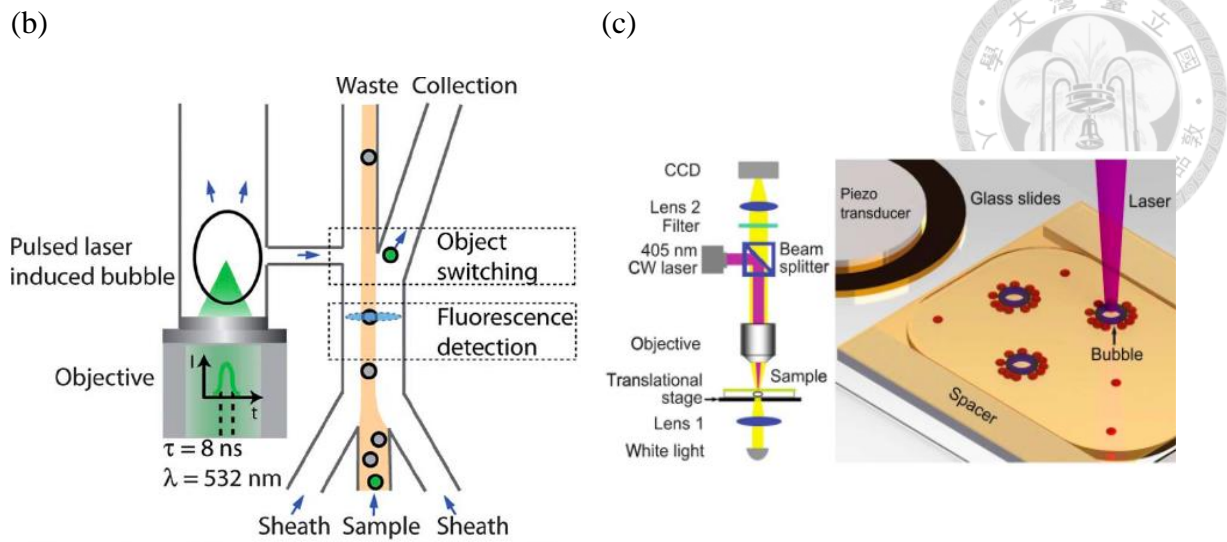


Figure 1-3. (a) Schematic processes of laser excited bubble cavitation [22]. (b) Schematic of the cell sorter within few microseconds response [23]. (c) The localized cell concentrator by acoustically activating the optothermally bubbles [24].

Although the optothermal cavitation bubbles mechanism, can indirectly generate larger force on the specimens without photo damage, the researchers continue to pursue a lower-cost and lower-power light source to access the opto-mechanical control. Since 2000s, opto-electrowetting (OEW) and optical dielectrophoresis (ODEP) techniques have been proposed to move liquid droplets and microparticles with high performance, reliability, simplicity, and fast response. Instead of the expensive and high power (hundred milliwatts to watt) laser, the OEW and ODEP are set up with the liquid crystal displays or projectors [27].

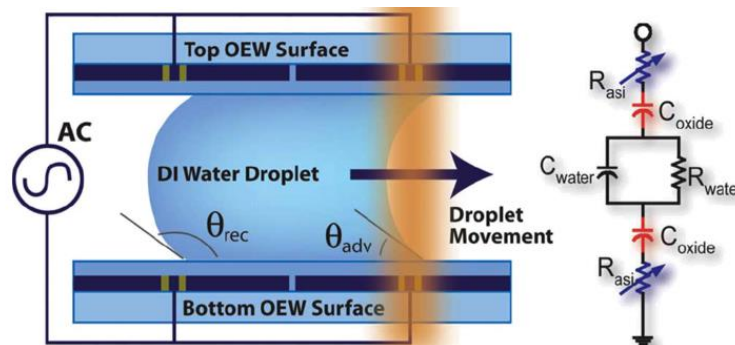
The opto-electrowetting (OEW), which was proposed by Chiou *et al.* in 2003 [28], now is an effective method for manipulating micro droplets. (Figure 1-4a) depicts a typical OEW device; the droplet is sandwiched between a top hydrophobic surface and a bottom OEW surface [29, 30, 31, 32]. The bottom OEW structure is made by an

electrodes array on a photoconductive material. In the light illuminating area, the electric conductivity of the photoconductive layer increases, causing more voltage across the droplet. Base on the relationship between the contact angle  $\theta$  and the applied voltage across the droplet in equation 1-1 [33], the contact angle of the droplet decrease and it moves toward the dark side.

$$\cos\theta = \cos\theta_0 + \frac{1}{2\gamma} \frac{\epsilon_r \epsilon_0}{t} V^2 \quad (1-1)$$

In equation 1-1,  $\theta_0$  is the original contact angle,  $\gamma$  is the surface tension between the droplet and surrounding medium,  $\epsilon_0$  is vacuum permittivity,  $\epsilon_r$  is the dielectric constant,  $t$  is the thickness of the dielectric layer, and  $V$  is the voltage. Recently, many modified OEW techniques are proposed for integrating with other microfluidic components. For example, Chuang *et al.* presented an open optoelectrowetting (o-OEW) device with a translational speed up to 3.6 mm/ s (Figure 1-4b) [34]. Park *et al.* proposed the single-sided continuous optoelectrowetting (SCOEW) to overcome the droplet size limitation in the sandwich OEW device (Figure 1-4c) [35].

(a)



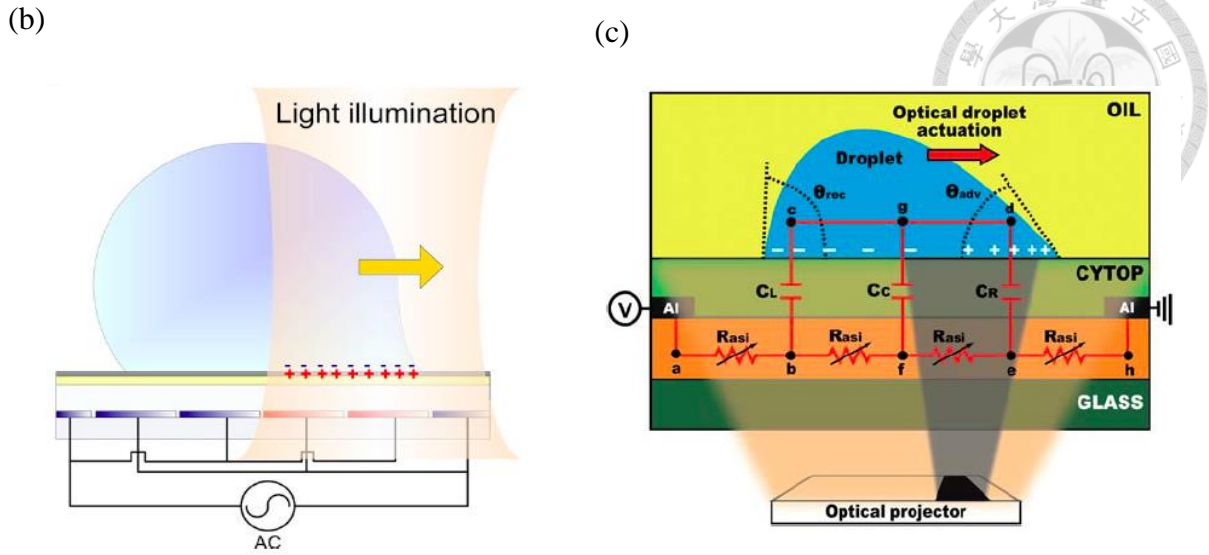
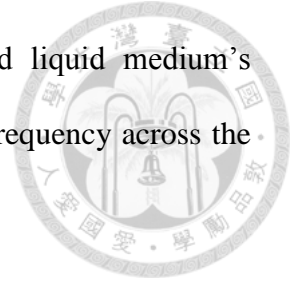


Figure 1-4. The scheme of (a) a typical OEW device [29], (b) open optoelectrowetting (o-OEW) device [34], and (c) Single-sided continuous optoelectrowetting (SCOEW) working principle with its equivalent circuit model [35].

Optical dielectrophoresis (ODEP) is another optoelectronic manipulation method, which was first proposed by Chiou *et al.* in 2005 for the parallel manipulation of single particles in (Figure 1-5a) [28]. Recently this technique is widely used in microfluidic and biological chips for cell patterning [36], sorting [37, 38], transfection [39], and separation [40]. An ODEP device consists of top and bottom transparent electrodes, and the bottom electrode is a photoconductive layer (Figure 1-5b). The photoconductive layer is used as localized virtual electrodes with incident light, making an intensive electric field in the bright area. Based on the conventional time average DEP force exerted on a sphere in a fluidic medium (equation 1-2), the particles in the aqueous can be collected in the bright areas. In this equation,  $R$  is the particle radius,  $\epsilon_m$  denotes the permittivity of the liquid medium,  $E_{rms}$  is the root-mean square magnitude of the electric field.  $K(\omega)$  is the



Clausius-Mossotti (CM) factor, which is related to the particle and liquid medium's permittivity ( $\epsilon_p$  and  $\epsilon_m$ ), conductivity ( $\sigma_p$  and  $\sigma_m$ ), and the applied frequency across the liquid medium ( $\omega$ ).

$$\langle \vec{F}_{DEP} \rangle \geq 2\pi R^3 \epsilon_m \text{Re}[K(\omega)] |\nabla |\vec{E}_{rms}|^2|$$

$$K^*(\omega) = \frac{\epsilon_p^* - \epsilon_m^*}{\epsilon_p^* + 2\epsilon_m^*}, \quad \epsilon_m^* = \epsilon_m + \frac{\sigma_m}{j\omega}, \quad \epsilon_p^* = \epsilon_p + \frac{\sigma_p}{j\omega} \quad (1-2)$$

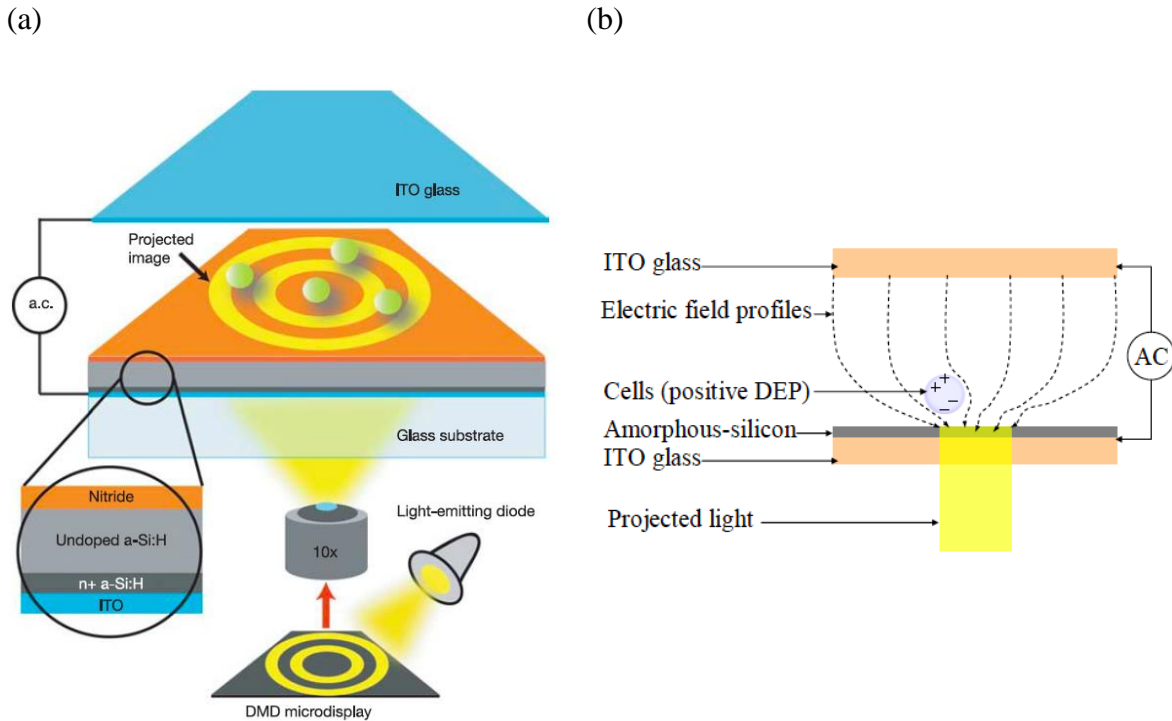


Figure 1-5. (a) The ODEP device for massive and parallel particles manipulation [27]. (b)

The scheme of ODEP mechanism [38].

Comparing the OEW and ODEP, due to their different working frequencies (10~20 kHz for OEW; 100~200 kHz for ODEP), the OEW is usually used for droplet manipulation,

but the ODEP can further control particles in microfluidic devices. In (Figure 1-6), below  $f_{min}$ , the impedance of the dielectric layer is larger than the dark impedance of the photoconductive layer (such as a-Si:H or TiOPc), so most of the voltage across the dielectric layer with or without light illumination. Between  $f_{min}$  and  $f_c$ , under illumination, the cross voltage switch from the photoconductive layer to the dielectric layer, causing OEW to occur. Between  $f_c$  and  $f_{max}$ , under illumination, the field now drops primarily across the liquid layer, resulting in OET. Above  $f_{max}$ , the impedance of the liquid becomes so low that it drops below  $Z_l$  inhibiting effective voltage switching [41].

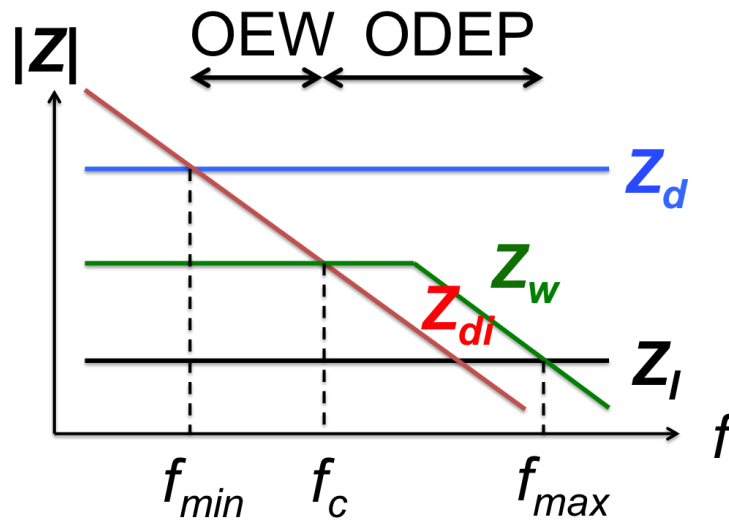
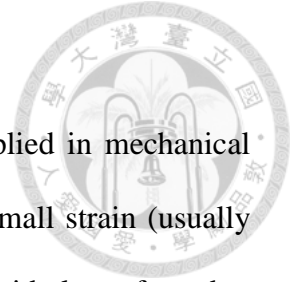


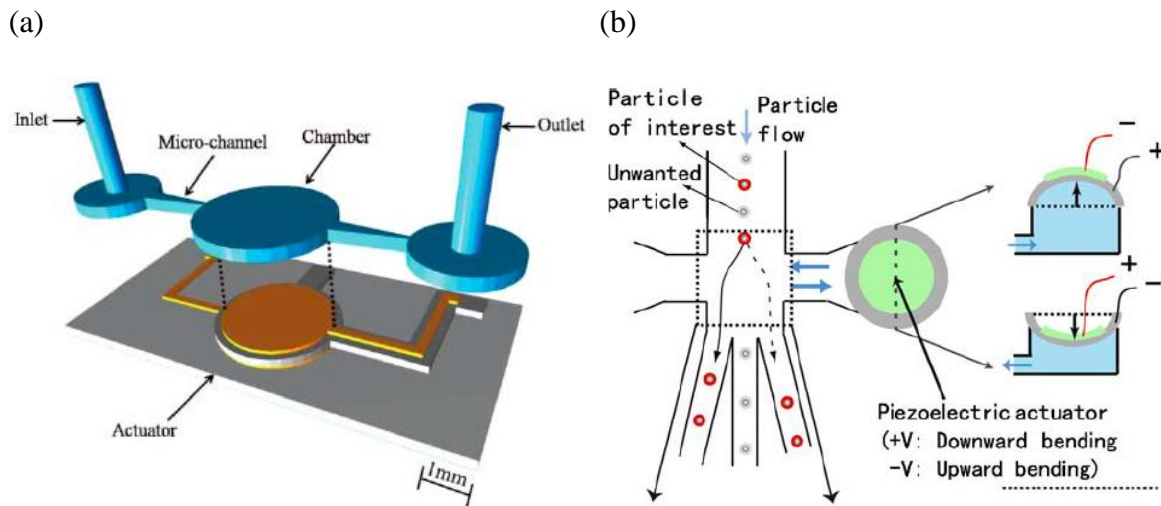
Figure 1-6. The frequency response figure (not to scale) of OEW and ODEP [41].

However, these conventional optoelectronic technologies are still only available for manipulation at nano-to sub-micro Newton scales. To obtain a better manipulation efficiency in a micro-environment, a much larger force should be discovered, developed and integrated with optical control.



### 1.3 Piezoelectric manipulations and control system

Over the last few decades, piezoelectric materials are widely applied in mechanical system as actuators or sensors. Piezoelectric actuators can generate small strain (usually  $<0.1\%$ ) and high stress (MPa) in a fast response time, so they can provide large force but small displacement, which can do suitable pumping [42, 43, 44, 45, 46], sorting [47, 48], or mixing in microfluidic devices [49, 50]. Furthermore, based on the direct piezoelectric effect [51], some flexible and transparent piezoelectric polymers are popularly used as pressure sensors in biological researches (Figure 1-7) [52, 53, 54, 55]. These polymer films have inertness to chemical agents, high sensitivity and electrical response over a wide frequency range.



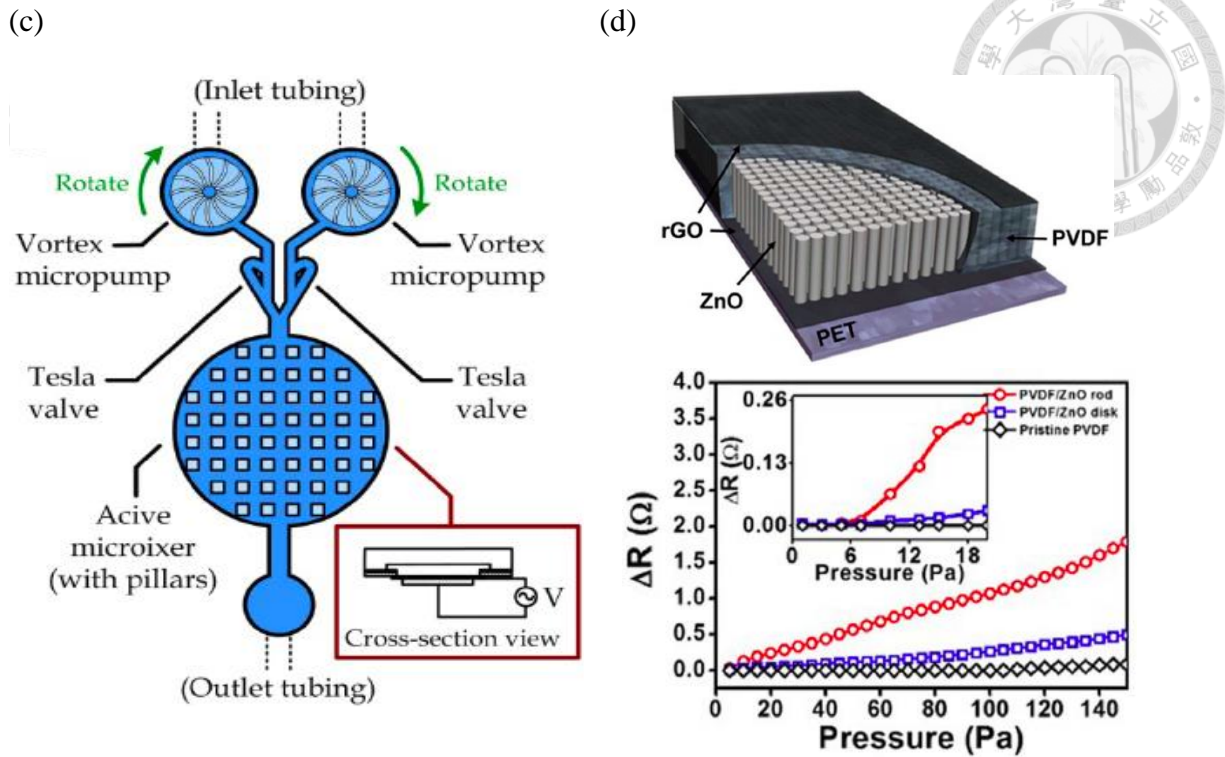
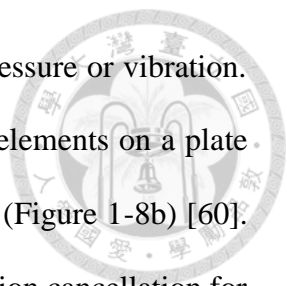


Figure 1-7. Piezoelectric effect in microfluidic device for (a) pumping [46], (b) sorting [47], (c) mixing [49], and (d) pressure monitoring [54].

Beside these vibration and deformation, the distributed piezoelectric elements or the so-called “smart-structures” provide the controlling ability in dynamic systems [56, 57]. Over the past 25 years, many researchers demonstrated the active control and adaptive structures with piezoelectric materials. Some early efforts focused on the integration of distributed sensors and actuators to target specific structural modes for application in sensing, actuation, or both. In 1989, Tzou *et al.* first derived the theories of distributed sensing and active vibration controlling for flexible shell structures [58]. In 1995, Qiu *et al.* controlled the bending moment of a circular cylindrical shell by the distributed inner and outer PVDF actuators with same values but opposite phases (Figure 1-8a) [59]. Some others studies discussed the interaction between the piezoelectric material and the structure



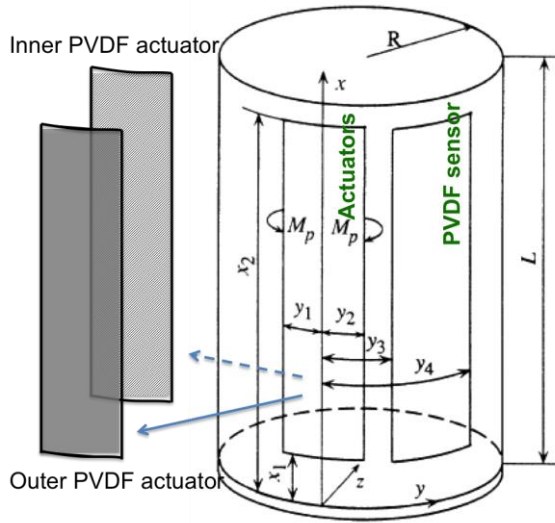


so that they could use the piezoelectric actuators to reduce the sound pressure or vibration. In 1991, Dimitriadis *et al.* demonstrated that bonding the piezoelectric elements on a plate could reduce the harmonic sound transmitted or radiated from the plate (Figure 1-8b) [60]. In 2008, Kozié'n *et al.* analyzed the possibility to active noise and vibration cancellation for the realistic machine structure with the distributed piezoelectric elements [61]. Recently, dell'Isola *et al.* proposed a damage detector which electric signals come from the state variables of the main structure and a distributed set of piezoelectric patches [62]. Wang *et al.* integrated piezoelectric actuating and sensing elements to be a cantilever-based oscillating type MEMS dc current sensor [63].

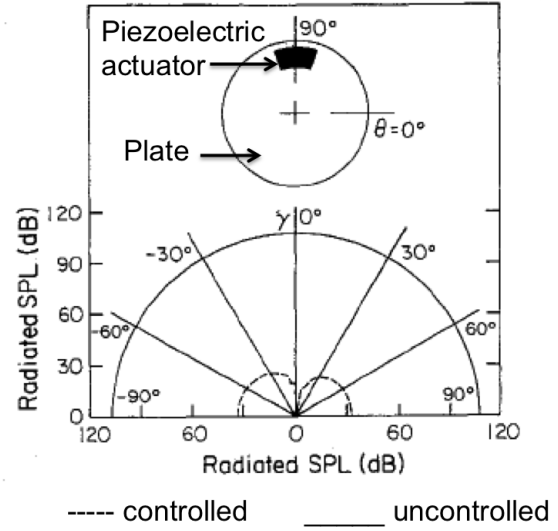
Particularly in 1989, Lee and Moon introduced the patterned electrode on a continuous piezoelectric film to measure some specific vibration modals [64, 65, 66]; these sensors with the spatial distribution electrodes are denoted as modal sensors (Figure 1-8c) [67]. In 2001, Hsu and Lee further designed the miniature Autonomous Phase-gain ROTation/ linear Piezoelectric Optimal Sensing (APROPOS) for a fundamental a free-fall motion [68]. They also proposed a no-phase delay low-pass filter to tailor the sensor transfer function with a symmetric weighting electrode (Figure 1-8d) [69].



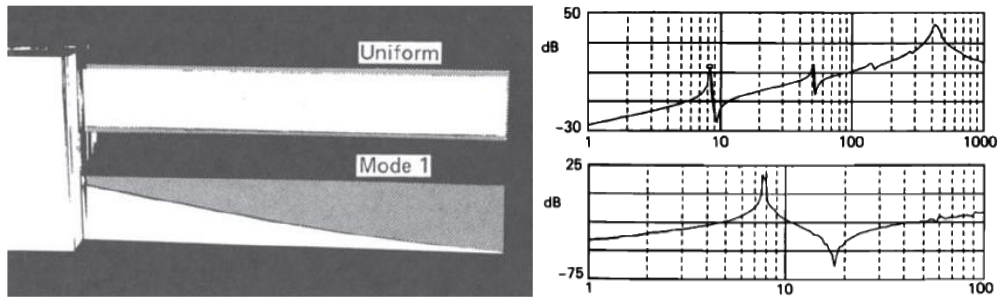
(a)



(b)



(c)



(d)

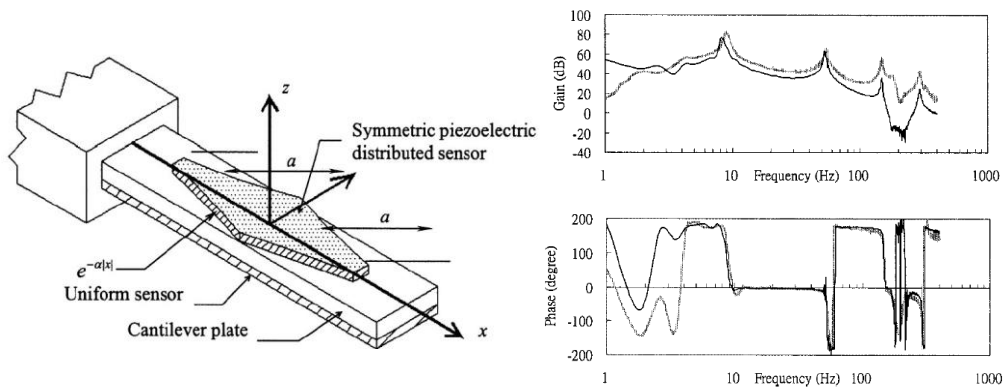


Figure 1-8. Distributed piezoelectric actuators or sensors for vibration controlling systems.

(a) Configuration of a bending control model by Qiu *et al.* [59]. (b) The sound pressure pattern of a plate vibration with and without piezoelectric actuators controlling [60]. (c) The uniform and mode 1 electrode patterns and their respective transfer functions [66]. (d) The schematic of a symmetric piezoelectric distributed sensor and its transfer function (dark line) versus a uniform sensor (gray line) [69].

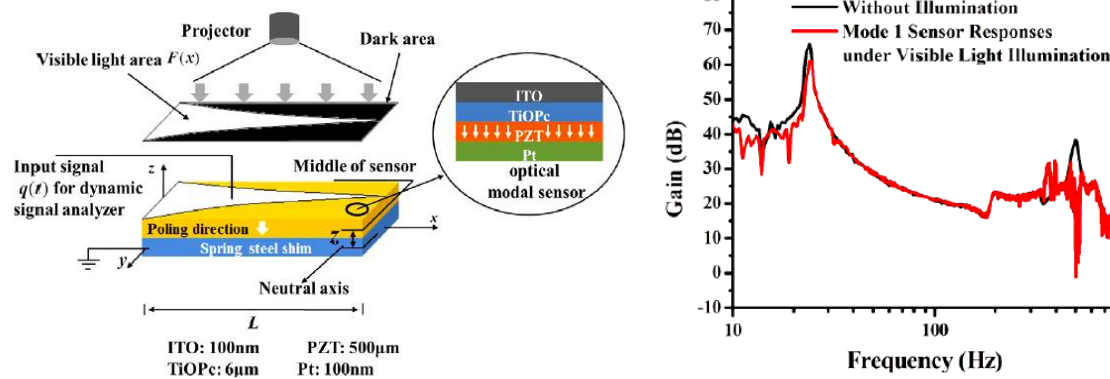
## 1.4 Optopiezoelectric control system

Based on the promising efficiency of piezoelectric actuators and sensors, it might be possible to develop an optical piezoelectric coupled mechanism for larger force control with novel opto-piezoelectric materials [49, 70]. Taking the convertible advantage of photoconductive materials, some photoconductive molecules are integrated with piezoelectric devices as optical virtual electrodes. In 2011, Chen *et al.* proposed an optically induced piezoelectric vibration control mechanism, which was achieved with a coupling of spiropyran-doped liquid crystal on PZT plates [71, 72] (Figure 1-9a). They made a mixture of liquid crystals (LC) and spiropyran (SP), then coated it onto a PZT plates as a virtual electrode. With UV light illumination, the spiropyran transfers to a polar molecule, and the impedance decreases more than one order of magnitude. Moreover the rod-like liquid crystals can host these doped spiropyran in a good alignment. Thus this photosensitive mixture, LC/SP, can be UV patterned for demonstrating a reversible optical controlled modal sensor.

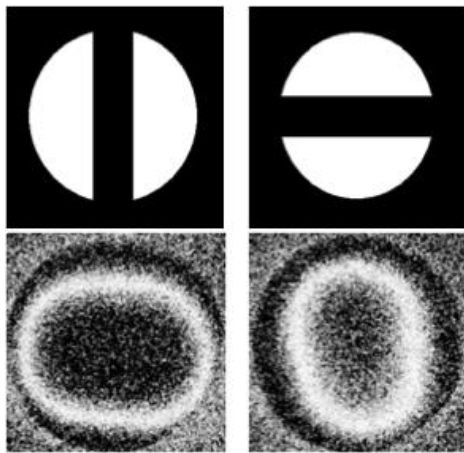
In 2013, Huang designed a deformable mirror using a spatially modulated TiOPc/ PZT actuator [73]. A white light triggered photoconductive material, TiOPc, was coated on the

PZT buzzer as virtual electrode. By projecting different light patterns, the spatially distributed actuating forces made this TiOPc/PZT actuator deforms in respective shapes (Figure 1-9b). One year later, Chang *et al.* proposed an optical spatially modulated TiOPc/ piezo buzzer actuator driven by optical patterns (Figure 1-9c) [74]. By varying light illumination pattern, the spatial force enhancement was found to change the acoustic beam pattern and directivity.

(a)



(b)



(c)

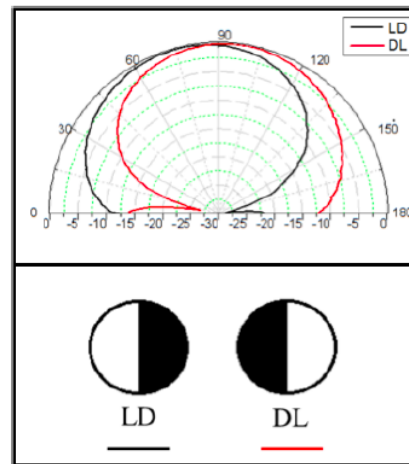


Figure 1-9. Light modulated optopiezoelectric controlling system. (a) Schematic of the TiOPc thin film-based optically modulated first modal sensor system [71, 72]. (b) The spatial deformations from a spatial illuminated PZT plate by the electronic speckle pattern interferometry (ESPI) measurement [73]. (c) The acoustic beam pattern directivity of “light/ dark (LD)” and “dark/ light (DL)” of a piezoelectric speaker [74].

## 1.5 Motivation and purpose

These previous studies demonstrated the performance of piezoelectric sensors and actuators. They also showed the possibility of light controlled piezoelectric devices. In this study, we further discuss the capability of optical piezoelectric manipulation for distributed sensors and piezoelectric actuators. In *Chapter 3*, a NMR compatible *C. elegant* trapper will be proposed for demonstrating the performance of PZT in microfluidic device. In *Chapter 4*, a novel photoconductive piezoelectric composite (P(VDF-TrFE)/TiOPc) will be developed and analyzed. This lead-free composite is better than PZT to be a biocompatible microfluidic chip substrate. Furthermore in *Chapter 5*, we will compare the mechanical sensing ability between this composite (P(VDF-TrFE)/TiOPc) and a double layers structure (TiOPc-PZT) through a bending sensor.

Overall, we try to set out a path to achieve the optical piezoelectric manipulation and sensing (Figure 1-10). In this thesis, we demonstrate the ability of piezoelectric devices in microfluidic devices, and then developing the optopiezoelectric material for further optopiezoelectric microfluidic application.

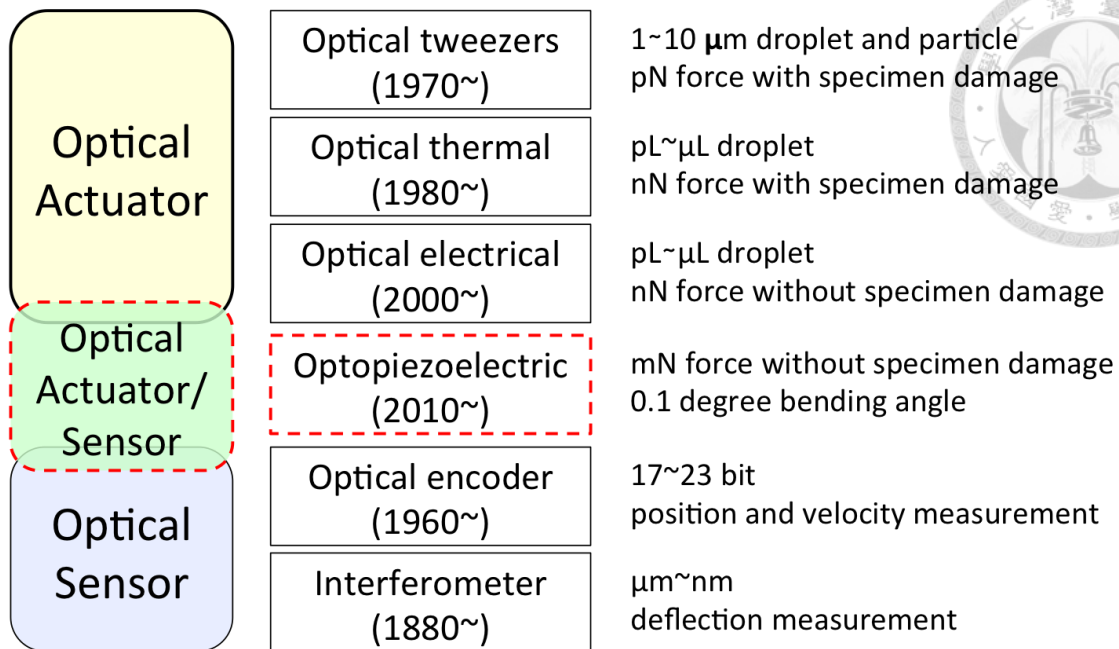


Figure 1-10. Overview of optical actuators and sensors for mechanical system.

## Chapter 2. Material



In this chapter, piezoelectric material and photoconductive material used in this study are discussed. In *Chapter 3*, we will integrate piezoelectric ceramic (PZT) into microfluidic device. In *Chapter 4*, optopiezoelectric actuator made of a spiropyran/ liquid crystal (SP/ LC) material layer on a PZT laminate will be examined. The optopiezoelectric sensor composed of piezoelectric polymer (P(VDF-TrFE) and photoconductive particles, titanyl phthalocyanine (TiOPc), are to be explored as well. In this chapter, the physical and chemical properties and applications of these materials are detailed.

### 2.1 Piezoelectric material

The piezoelectric effect was discovered by Pierre and Jacques Curie in 1880. But practical applications started after 1940s when sonars development started. Piezoelectric materials can be used as an actuator to transfer electrical signal into mechanical deformation (direct effect), or it can be used as a sensor to transform vibrations into electrical energy (converse effect) (Figure 2-1). The basic but detailed piezoelectric theory will be discussed in *Chapter 3*.

#### 2.1.1 Lead Zirconium Titanate (PZT)

The most commercialized and widely applied piezoelectric material is lead zirconate titanate (PZT) ( $\text{Pb}[\text{Zr}_{(x)}\text{Ti}_{(1-x)}]\text{O}_3$ ). PZT has excellent piezoelectric properties, high Curies temperature ( $>150^\circ\text{C}$ ), high spontaneous polarization (remnant charge  $> 50 \mu\text{C}/\text{cm}^2$ )

and high electromechanical coupling coefficient ( $d_{31}$ ,  $d_{33}$  equal to few hundreds pC/N). It has become the basis of many important industrial products. Over the years, PZT has been applied in underwater sensors [75, 76], biosensors [77, 78], and energy harvesters [79, 80], etc.

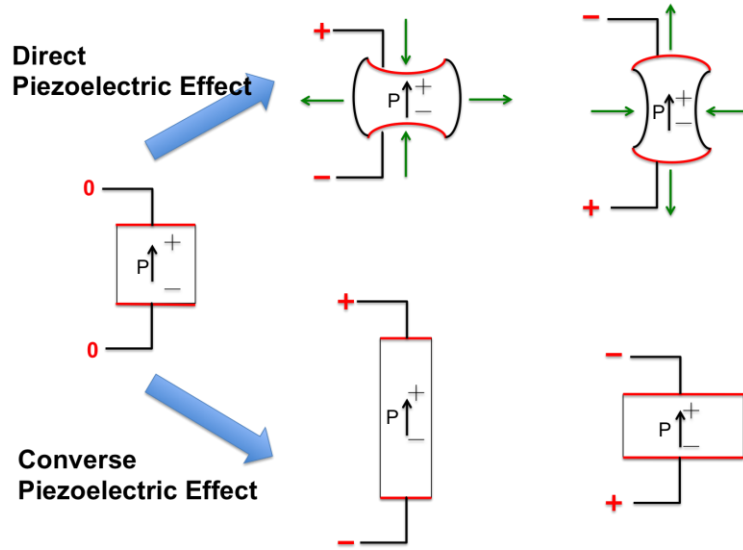
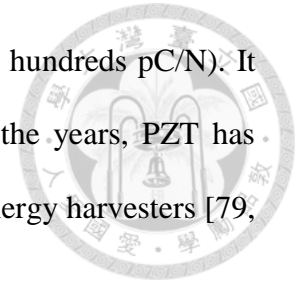


Figure 2-1. The working function of positive and converse piezoelectric effect.

### 2.1.2 Piezoelectric polymer

Piezoelectric polymers have been discovered for more than 40 years, but in recent years they have progressively developed due to its flexible, lightweight and transparent advantages. The properties of polymers are very different from PZT in (Table 2-1). The piezoelectric polymers have much higher piezoelectric stress constant ( $g_{31}$ ), which indicates that they are much better sensors than ceramics [81]. Polymers also typically possess high dielectric breakdown and high operating field strength, which means they can withstand much higher driving fields than ceramics. Furthermore, with spin coating or electro spinning process, different mechanical properties and applications of the piezoelectric



polymer can be fabricated by using the sol-gel processes [82, 83]. Thus piezoelectric polymers surely establish its technical applications and useful device configurations.

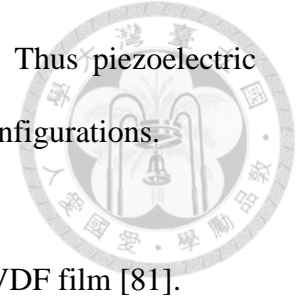


Table 2-1. The piezoelectric properties comparison of PZT and PVDF film [81].

Property	PZT	PVDF
Density ( $10^3\text{kg/m}^3$ )	7.5	1.78
Relative Permittivity $\epsilon/\epsilon_0$	1200	12
$d_{31}$ (pC/N)	110	23
$g_{31}$ ( $10^{-3}\text{V}\cdot\text{m/N}$ )	10	216
$k_{31}$ (%)	30	12
Acoustic Impedance ( $\text{Mkg/m}^2\cdot\text{sec}$ )	30	2.7
Features	Brittle, heavy, toxic	Flexible, lightweight, low mechanical impedance

Nowadays, Poly(vinylidene fluoride) (PVDF) is one of the most applied piezoelectric polymers. It was found in 1969 to have a very large piezoelectric coefficient 6- 7 pC/N [84, 85]. Its chemical structure of (-CH<sub>2</sub>-CF<sub>2</sub>-) repeat units provides large chain flexibility. The highly repulsive forces of the fluorine atoms making the polymer polarized naturally (Figure 2-2). The most common and thermodynamically stable phase is the  $\alpha$ -phase, which has a trans-gauche (TGTG') conformation and does not show a net lattice polarization, i.e., this phase presents no piezoelectric effect. After stretching and poling processes, the  $\alpha$ -phase transfers to  $\beta$ -phase in an all-trans (TTTT) zig-zag conformation (Figure 2-3). The C-F dipoles all align in the same direction providing the  $\beta$ -phase PVDF a spontaneous lattice polarization, which is necessary to ferroelectric effect [86].

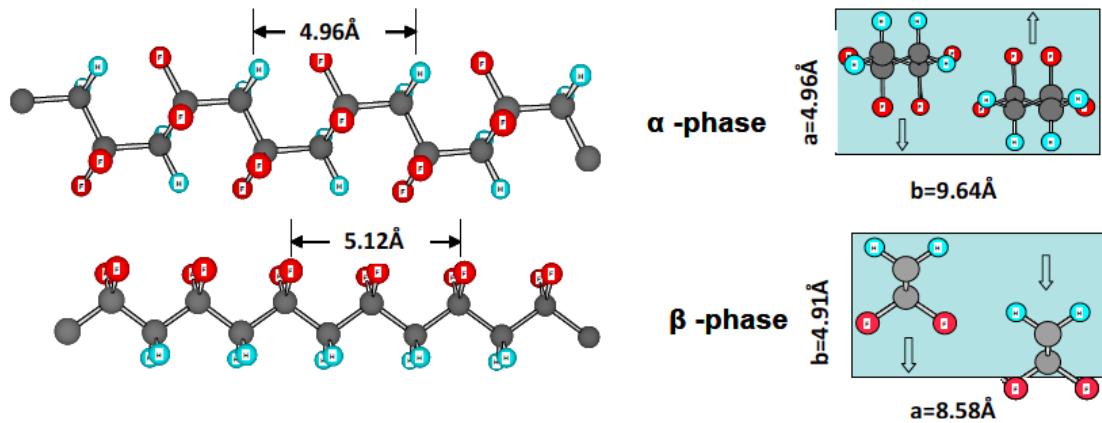


Figure 2-2. Molecular conformations and unit cells of the two common polymorphs of PVDF [86].

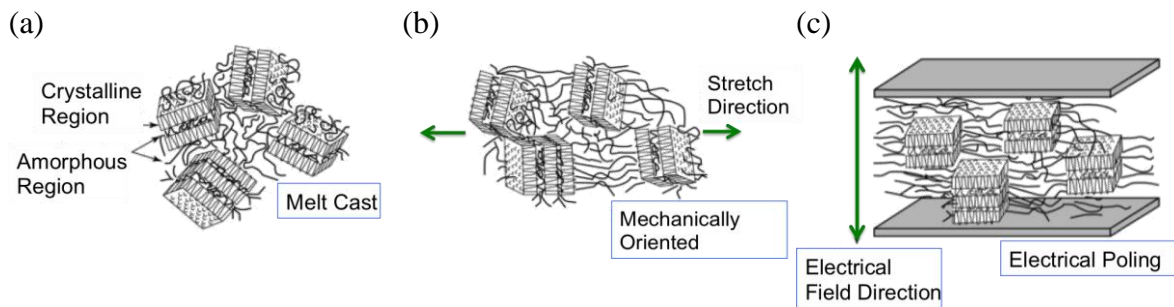


Figure 2-3. Schematic of random crystal lamellae in PVDF polymer: (a) the morphology after the film is melt cast; (b) the film orientation after stretching; and (c) after poling through the film thickness [87].

In the last decade, copolymers of PVDF with trifluoroethylene (TrFE) (-CHF-CF<sub>2</sub>-) containing different mole fractions of both components have been studied extensively. It is because they exhibit certain advantages over pure PVDF. P(VDF-TrFE) is synthesized by copolymerization VDF and TrFE monomers (Figure 2-4). Due to the higher repulsive forces of one more fluorine atoms, the ferroelectric phase is inherent in the copolymer at

room temperature. Unlike typical PVDF must be stretched, P(VDF-TrFE) can achieve  $\beta$ -phase conformation by only poling with a high electric field (in the order 50 MV/m) [88~92]. More piezoelectric properties of PVDF and P(VDF-TrFE) are compared in (Table 2-2).

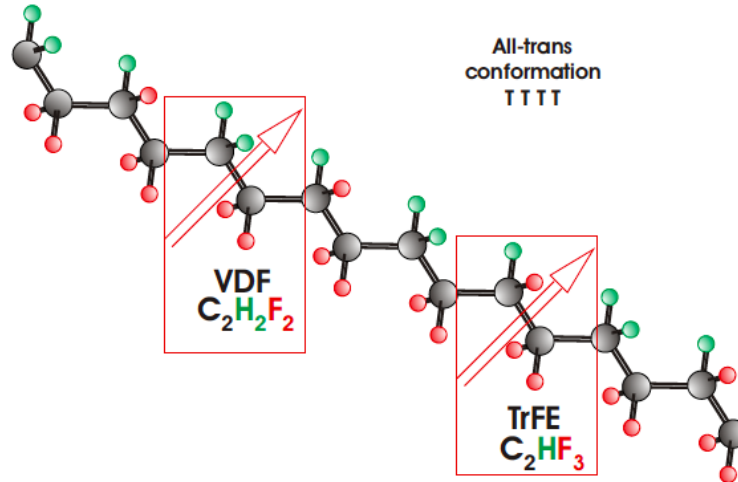
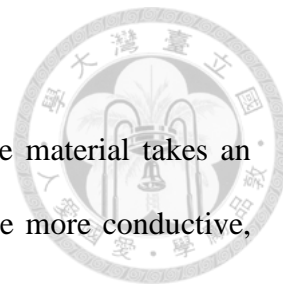


Figure 2-4. Schematic structure of the molecule chain of P(VDF-TrFE) copolymer in all-trans conformation with a ratio of VDF and TrFE of 75 : 25.

Table 2-2. Comparisons of PVDF and P(VDF-TrFE) [81]

Parameter	Symbol and Unit	PVDF	P(VDF-TrFE)
Young's modulus	( $10^9$ N/m <sup>2</sup> )	2~4	3~5
Relative Permittivity $\epsilon/\epsilon_0$		12	7
Breakdown voltage	(V/ $\mu$ m), DC at 25° C	2000	2000
Maximum Operating Voltage	(V/ $\mu$ m), DC at 25° C	750	750
Operating Temperature Range	(°C)	-40~60	-20~70
Electromechanical coupling factor	$k_{31}$ (%)	12	20
Piezoelectric Strain Constant	$d_{31}$ (pC/N) $d_{33}$ (pC/N)	23 -33	11 -38
Piezoelectric Stress Constant	$g_{31}$ ( $10^{-3}$ V•m/N) $g_{33}$ ( $10^{-3}$ V•m/N)	216 -330	162 -542



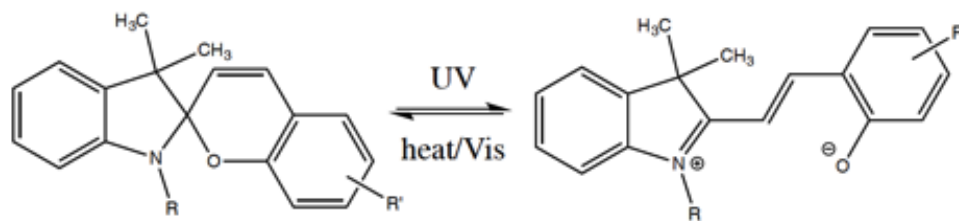
## 2.2 Photoconductive material

For developing an optopiezoelectric material, the photoconductive material takes an important role for light-spatial modulation. These materials should be more conductive, i.e. their electrical impedance decreases after light illumination.

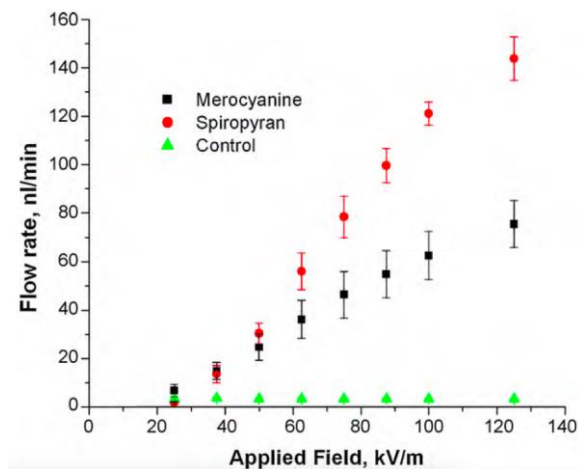
### 2.2.1 Spiropyran

Spiropyran has been a popular photochromic material in photosensitive devices due to its advantageous physical and chemical properties [93, 94, 95]. This molecular can be transformed from a spiropyran (SP) state into a merocyanine (MC) state under UV irradiation, and it is reversible by visible light irradiation or heating (Figure 2-5a). More specifically, the carbon-oxygen bond of the spiropyran is opened during transformation, which provides good ionic conductivity. Furthermore, the color also changes from light purple to a darker one under irradiation. Thus, the spiropyran molecules have widely applications include optical memories, sensors and transistors in (Figure 2-5b~ 2-5d) [96~100].

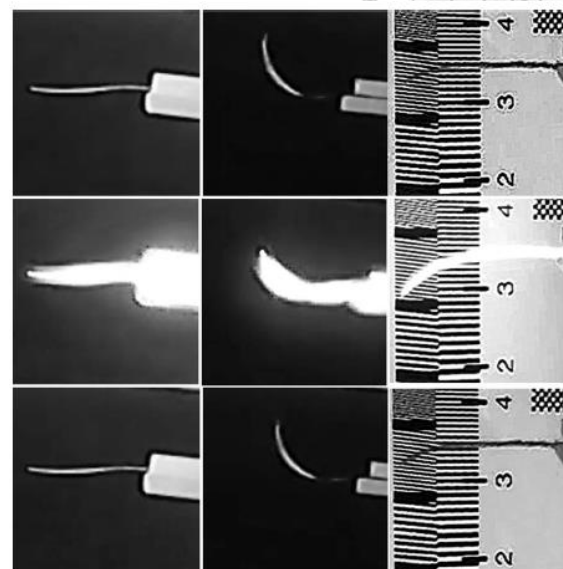
(a)



(b)



(c)



(d)

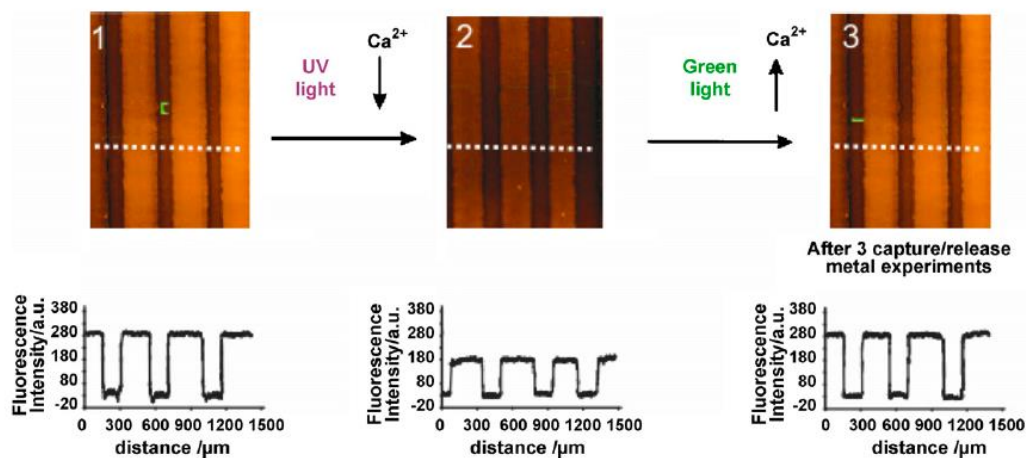
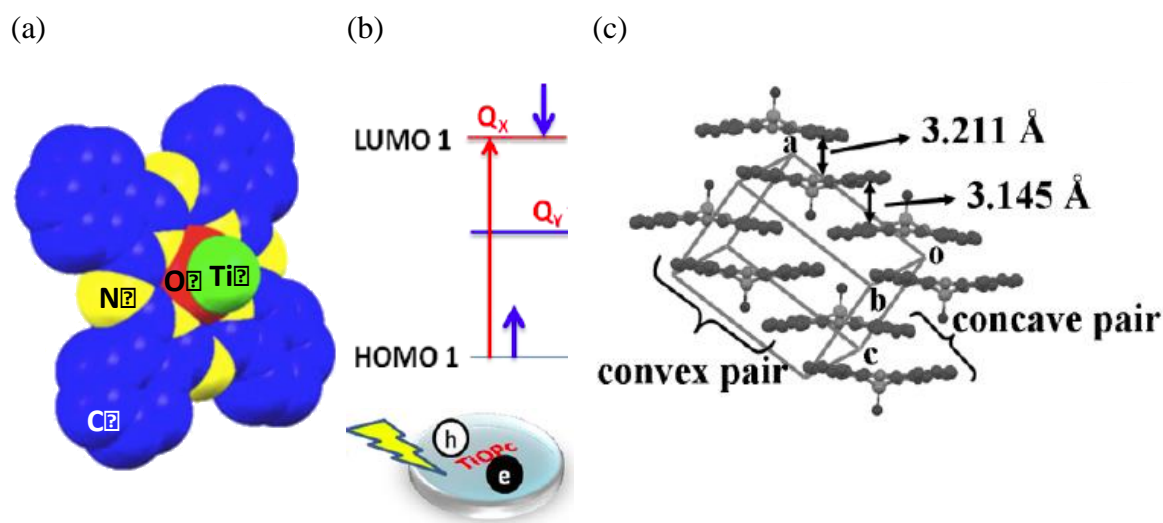


Figure 2-5. The spiropyran chemical structure and some related applications. (a) The reversible process. (b) The flow rate of photo-controllable electroosmotic in both SP and MC form, and the poly(styrene-co-divinylbenzene) monolith using 1mM HCl as the electrolyte [98]. (c) A light activated shape memory made of spiropyran doped ethylene-vinyl acetate copolymers [99]. (d) A spiropyran modified micro-fluidic chip channels for controlling and detecting metal ion accumulation and release [100].

## 2.2.2 Titanyl Phthalocyanine (TiOPc)

In this study, we also considered titanyl phthalocyanine (TiOPc), which is an organic photovoltaic material. TiOPc is a non-planar phthalocyanines (Pcs) with the Ti=O located slightly above (ca. 0.3Å) the ring, orthogonal to the molecular plane (Figure 2-6a). Upon photo excitation, an electron can either move from HOMO to LUMO within a molecule (Figure 2-6b) [101]. These surprisingly close  $\pi$ - $\pi$  molecular contacts indicate a TiOPc has a broadening of the absorbance spectrum toward the near IR region. (Figure 2-6c, 2-6d) [102]. And its high hole mobility (over 1.0 cm<sup>2</sup> V<sup>-1</sup> s<sup>-1</sup>) and on/off ratio make it the most efficient organic photoconductors used in more than 90% of the laser printers (Figure 2-6e) [103]. Recently, because of its characteristics of strong illumination absorption from the visible to the IR region [104~ 106], it is also been taken in optoelectronic chip for the dynamic manipulation [107~ 109] and solar cells [110~ 112] (Figure 2-7).



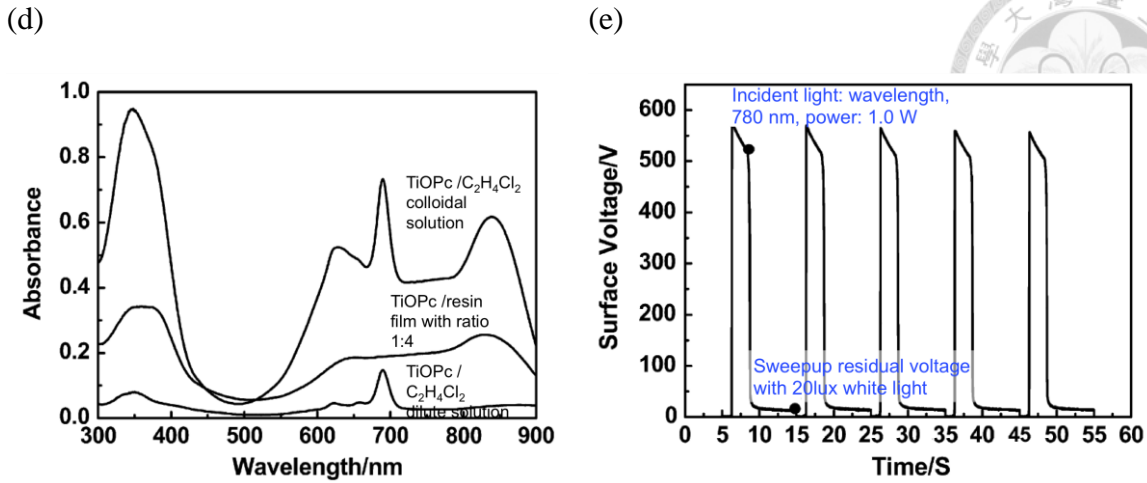


Figure 2-6. The physical properties of titanyl phthalocyanine (TiOPc). (a) Schematic molecular model. (b) Molecular stacking of a-TiOPc crystal showing the p-stacking structure with concave pair and convex pair with significant molecular overlaps and very short intermolecular distances [102]. (c) Schematic explaining charges excitons in TiOPc [102]. (d) UV-vis spectra of TiOPc in the colloidal solution and resin film made by Wei Chao *et al.* [103]. (e) The photo-induced discharging curve of a TiOPc film made by Wei Chao *et al.* [103].

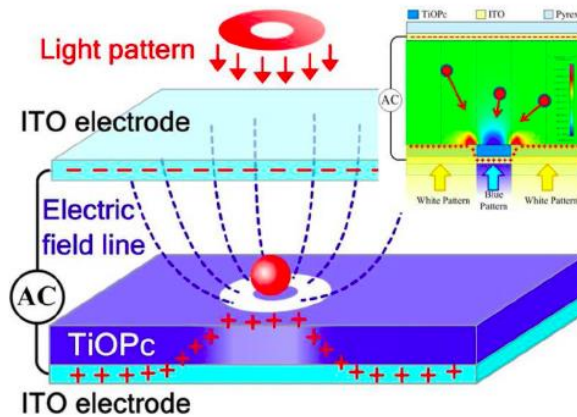


Figure 2-7. Operation principle of the light-induced electric field for small particles manipulation by Shih-Mo Yang *et al.* [107].



## Chapter 3. A living worm trapper by PZT actuator

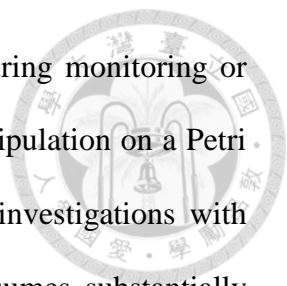
### 3.1 Introduction

*Caenorhabditis elegans* (*C. elegans*) (Figure 3-1) is a 1-mm long transparent roundworm. It has a two weeks lifespan and is one of the simplest organisms for understanding cell division directly under the microscope. In the early 1960s, Sydney Brenner declared the use of *C. elegans* as a model to trace how genes made bodies and their behavior. In 2002, Sydney Brenner, H. Robert Horvitz and John E. Sulston received the Nobel Prize in Physiology or Medicine for their discoveries concerning "*genetic regulation of organ development and programmed cell death*" (an extract from The Nobel Assembly at Karolinska Institutet, 7, October, 2002). Now the *C. elegans* has become a widely used model organism in biology.



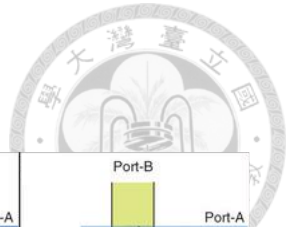
Figure 3-1. The worm image [113]



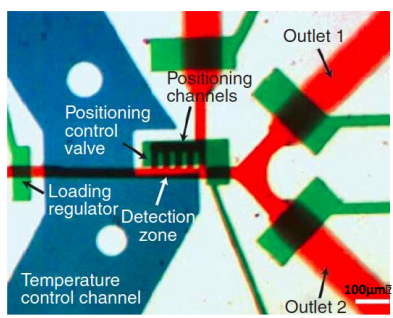


Studies of *C. elegans* often require immobilizing the worm during monitoring or giving stimulation. Traditional techniques were based on manual manipulation on a Petri dish or a multiwall plate, and permanent immobilization for further investigations with cyanoacrylate glue or anesthetics [114, 115]. The first method consumes substantially long time, and the irreversible glues may have some toxicity. The second method gives unavoidably internal biochemical of the worm during injecting the anesthetics [116]. Currently microfluidics and micro-electromechanical system (MEMS) devices provide powerful tools and great advance for worm immobilization.

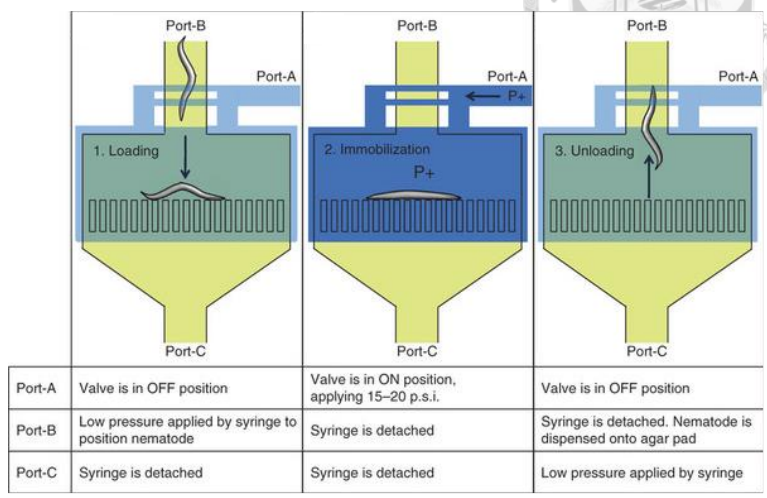
Besides using these micro chambers and pillars [117, 118], the worm immobilization can be accomplished by temperature [119] or pressure control [120], mechanical [121, 122], electrical [123], and acoustic modulation [124] (Figure 3-2a~ 3-2d). But all these methods must maintain the pressure, temperature, or electric field continuously in order to keep the worm immobilized. They need to maintain the operation field poses a drawback for instrument such as nuclear magnetic resonance (NMR) that does not have enough spaces in the detection area for the electric wires or fluidic tubes. In this chapter, we develop an on demand piezoelectric worm trapper, which can efficiently trap the *C. elegans*, and keep it immobilized by hydrostatic equilibrium without using any wires, tubes, and connectors.



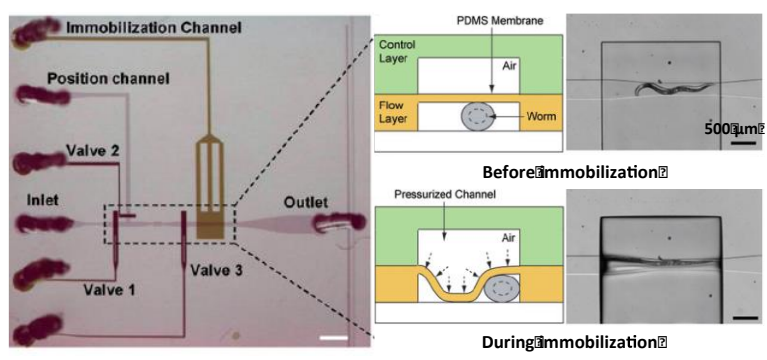
(a)



(b)



(c)



(d)

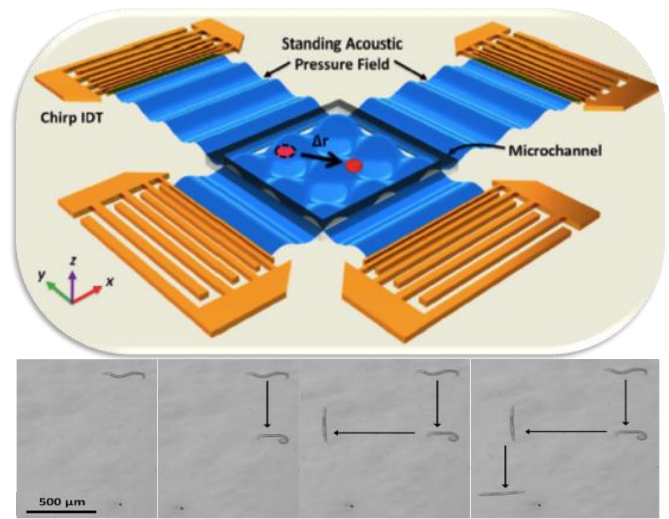




Figure 3-2. Methods for worm immobilization: (a) by transiently cooling them on-chip to  $\sim 4\text{ }^{\circ}\text{C}$  [119], (b) by controlling valves states sequence [120], (c) by mechanical clamping [121], and (d) by acoustic resonance wave [122].

## 3.2 Theory

In this worm trapper, the worms are immobilized between oil bulges, which are pushed from the piezoelectric generated pressure (Figure 3-3). The related theories include the piezoelectric plate actuator and Laplace pressure.

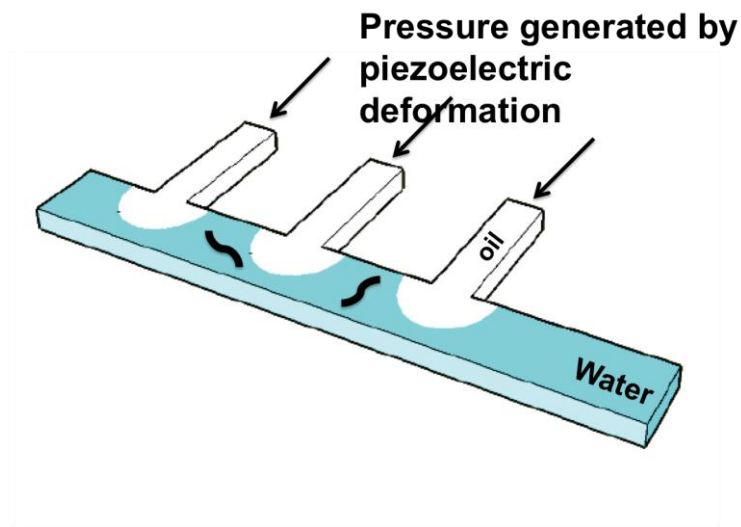
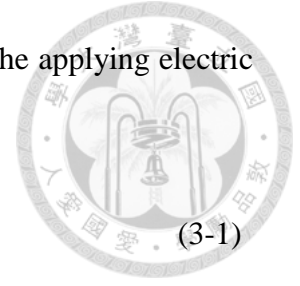


Figure 3-3. The scheme of the living worm trapper with PZT actuator.

### 3.2.1 A linear piezoelectric thin plate actuator

The piezoelectric constitutive equations are used to calculate the transfer efficiency between electrical and mechanical signals [125]. In these equations, the piezoelectric

materials are assumed to be a linear material, which is only true when the applying electric field is small. There are four types of the equations as listed below:



$$\text{Stress-Electric field type: } \begin{cases} T_p = c_{pq}^D S_q - h_{kp} D_k \\ E_k = -h_{kq} S_q + \beta_{ki}^S D_i \end{cases} \quad (3-1)$$

$$\text{Strain-Electric field type: } \begin{cases} S_p = s_{pq}^D T_q + g_{kp} D_k \\ E_k = -g_{kq} T_q + \beta_{ki}^T D_i \end{cases} \quad (3-2)$$

$$\text{Strain-Charge type: } \begin{cases} S_p = s_{pq}^E T_q + d_{kp} E_k \\ D_k = d_{kq} T_q + \varepsilon_{ki}^T E_i \end{cases} \quad (3-3)$$

$$\text{Stress-Charge type: } \begin{cases} T_p = c_{pq}^D S_q - e_{kp} E_k \\ D_k = e_{kq} S_q + \varepsilon_{ki}^S E_i \end{cases} \quad (3-4)$$

The parameters and variables are detailed in (Table 3-1), and the subscripts refer to IEEE compact matrix notation in (Table 3-2) [125]. The relationships between the variables can also be represented as (Figure 3-4).

Table 3-1. The parameters and variables in (equation 1~ 4).

Symbol	Name	Unit	Relationship	
$T_p$	Stress	Pa	/	
$S_p$	Strain	1		
$E_k$	Electric field	V/m		
$D_k$	Electric displacement	C/ m <sup>2</sup>		
$\varepsilon_{ki}^S, \varepsilon_{ki}^T$	Dielectric or permittivity constant matrix	F/m		
$\beta_{ki}^S, \beta_{ki}^T$	Impermittivity constant matrix	m/F		
$c_{pq}^E, c_{pq}^D$	Elastic stiffness matrix	Pa		
$s_{pq}^E, s_{pq}^D$	Elastic compliance matrix	1/Pa		
$d_{kp}, d_{kq}$	Piezoelectric strain/ charge constant	C/N		$d_{kp} = \varepsilon_{ki}^T g_{ip}$
		m/V		$d_{kp} = e_{kq} s_{qp}^E$
$e_{kp}, e_{kq}$	Piezoelectric stress/ charge constant	N/Vm	$e_{kp} = d_{kq} c_{qp}^E$	
		C/ m <sup>2</sup>	$e_{kp} = \varepsilon_{ki}^S h_{ip}$	
$g_{kp}, g_{kq}$	Piezoelectric strain/ voltage constant	Vm/N	$g_{kp} = \beta_{ki}^T d_{ip}$	
		m <sup>2</sup> /C	$g_{kp} = h_{kq} s_{qp}^D$	
$h_{kp}, h_{kq}$	Piezoelectric stress/ voltage constant	V/m	$h_{kp} = \beta_{ki}^S e_{ip}$	
		N/C	$h_{kp} = g_{kq} c_{qp}^D$	

Table 3-2. IEEE compact matrix notation [125].

$ij$ or $kl$	$p$ or $q$
11	1
22	2
33	3
23, 32	4
13, 31	5
12, 21	6

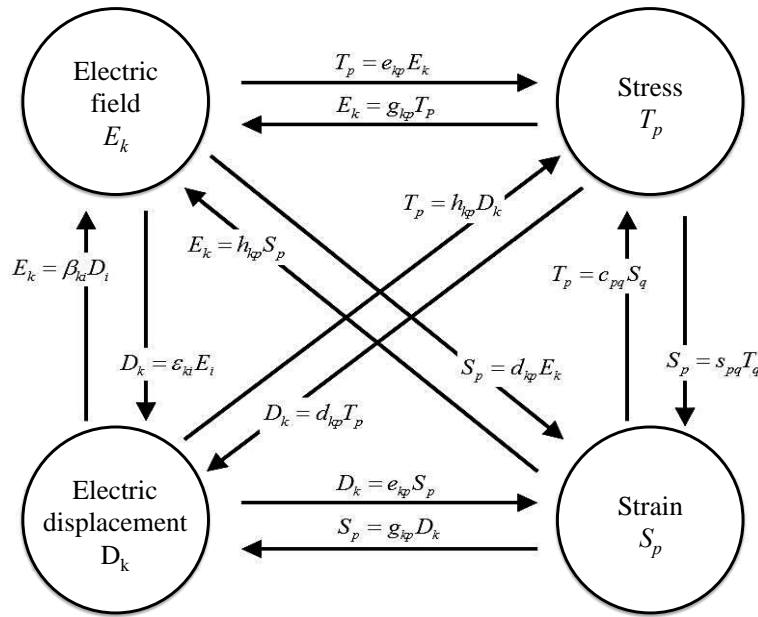


Figure 3-4. The relationship between stress, strain, electric field, and electric displacement.

In this study, we used a commercial buzzer (Figure 3-5a), which is composed of a PZT plate ( $\phi=17.5\text{mm}$ ;  $h=200\mu\text{m}$ ) glued onto a brass plate ( $\phi=12.5\text{mm}$ ;  $h=100\mu\text{m}$ ) as an actuator. With applied voltage, the PZT material stretches, and the stress transfers to the connected brass layer. The deformation can be clearly analyzed by a simplified modal (Figure 3-5b) [126, 127]. The displacement at the interface can be represented as (equation 3-5):



$$\begin{aligned}
 u_3(x_1, x_2, x_3, t) &\equiv u_3^{(0)}(x_1, x_2, t) \\
 u_1(x_1, x_2, x_3, t) &\equiv u_1^{(0)}(x_1, x_2, t) - x_3 u_{3,1}^{(0)} \\
 u_2(x_1, x_2, x_3, t) &\equiv u_2^{(0)}(x_1, x_2, t) - x_3 u_{3,2}^{(0)}
 \end{aligned}
 \tag{3-5}$$

$u_i^{(0)}$  and  $u_3^{(0)}$  are the stretch and bending displacement of the interface. From (equation 3-5), the strain can be expressed in terms of (equation 3-6):

$$\begin{aligned}
 S_1 &= u_{1,1}^{(0)} - x_3 u_{3,11}^{(0)} \\
 S_2 &= u_{2,2}^{(0)} - x_3 u_{3,22}^{(0)} \\
 2S_{12} = S_6 &= u_{1,2}^{(0)} + u_{2,1}^{(0)} - 2x_3 u_{3,12}^{(0)}
 \end{aligned}
 \tag{3-6}$$

For an isotropic piezoelectric plate, the strain and stress are related in (equation 3-7), which  $S_i$  is stress,  $T_i$  is strain,  $s_{ij}$  is elastic compliance constant,  $s_{66} = 2(s_{11} - s_{12})$ , and  $E_3 = -V / h_c$ . If the thickness of the plate is too thin to negligible, and the stress along z-direction  $T_3$  is zero, then (equation 3-7) can also be written as (equation 3-8) with elastic stiffness constant ( $c_{ij}$ ) and piezoelectric stress/ charge constant ( $e_{ij}$ ). Thus the piezoelectric constitutive (equation 3-3, 3-4) can be written as (equation 3-9).

$$\begin{aligned}
 S_1 &= s_{11}T_1 + s_{12}T_2 + s_{13}T_3 + d_{31}E_3 \\
 S_2 &= s_{12}T_1 + s_{11}T_2 + s_{13}T_3 + d_{31}E_3
 \end{aligned}
 \tag{3-7}$$

$$S_6 = s_{66}T_6$$

$$T_1 = c_{11}^p S_1 + c_{12}^p S_2 - e_{31}^p E_3 \tag{3-8}$$

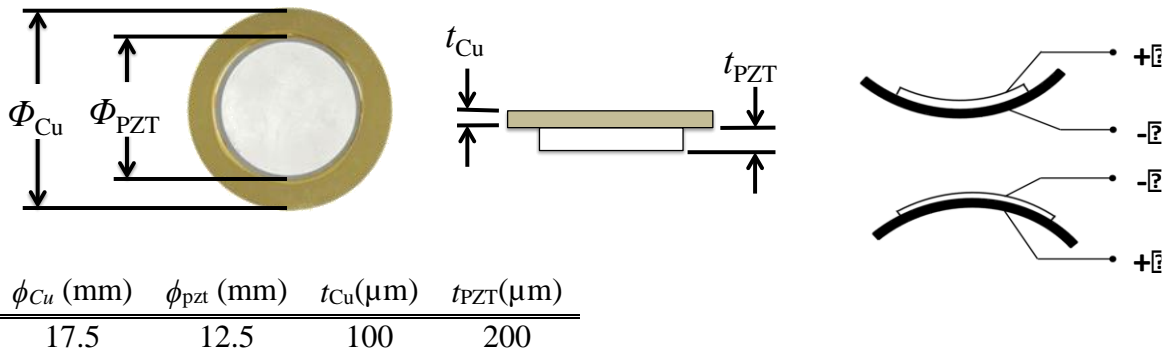


$$T_2 = c_{12}^p S_1 + c_{22}^p S_2 - e_{31}^p E_3$$

$$T_{12} = c_{66}^p S_6$$

$$D_3 = d_{31}(T_1 + T_2) + \epsilon_{33}^p E_3 = e_{31}^p (S_1 + S_2) + \epsilon_{33}^p E_3 \quad (3-9)$$

(a)



(b)

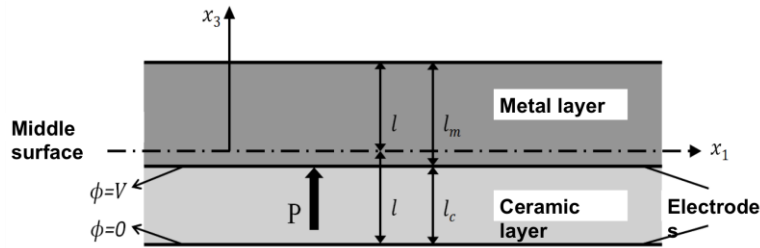


Figure 3-5. (a) The deformation of a buzzer with a DC voltage, and (b) the single layer piezoelectric actuator.

For an isotropic metal plate, its stress equation is the same as (equation 3-8). If the PZT layer is very thin, the electric field  $E_3$  is independent to the z-direction, the stretch can be written as (equation 3-10). The superscript “ $\wedge$ ” means the material parameters without applied electric field.

$$T_{11}^{(0)} = \int_{-l}^l T_{11} dx_3 = a_{11} u_{1,1}^{(0)} + a_{12} u_{2,2}^{(0)} + b_{11} u_{3,11}^{(0)} + b_{12} u_{3,22}^{(0)} - l_c e_{31}^p E_3 \quad (3-10)$$



$$T_{22}^{(0)} = \int_{-l}^l T_{22} dx_3 = a_{12} u_{1,1}^{(0)} + a_{11} u_{2,2}^{(0)} + b_{11} u_{3,11}^{(0)} + b_{12} u_{3,22}^{(0)} - l_c e_{31}^p E_3$$

$$T_{12}^{(0)} = \int_{-l}^l T_{12} dx_3 = a_{66} (u_{1,2}^{(0)} + u_{2,1}^{(0)}) + 2b_{66} u_{3,12}^{(0)}$$

where

$$a_{11} = c_{11}^p l_c + \hat{c}_{11}^p l_m, \quad a_{12} = c_{12}^p l_c + \hat{c}_{12}^p l_m$$

$$a_{66} = c_{66}^p l_c + \hat{c}_{66}^p l_m = \frac{(a_{11} - a_{12})}{2}$$

$$b_{11} = \frac{1}{2} (c_{11}^p - \hat{c}_{11}^p) l_c l_m, \quad b_{12} = \frac{1}{2} (c_{12}^p - \hat{c}_{12}^p) l_c l_m$$

$$b_{66} = \frac{1}{2} (c_{66}^p - \hat{c}_{66}^p) l_c l_m = \frac{(b_{11} - b_{12})}{2}$$

The bending stress of the composite structure is shown in (equation 3-11):

$$T_{11}^{(1)} = \int_{-l}^l T_{11} x_3 dx_3 = -b_{11} u_{1,1}^{(0)} - b_{12} u_{2,2}^{(0)} - \gamma_{11} u_{3,11}^{(0)} - \gamma_{12} u_{3,22}^{(0)} + l_c l_m e_{31}^p E_3$$

$$T_{22}^{(1)} = \int_{-l}^l T_{22} x_3 dx_3 = -b_{12} u_{1,1}^{(0)} - b_{11} u_{2,2}^{(0)} - \gamma_{12} u_{3,11}^{(0)} - \gamma_{11} u_{3,22}^{(0)} + l_c l_m e_{31}^p E_3 \quad (3-11)$$

$$T_{12}^{(1)} = \int_{-l}^l T_{12} x_3 dx_3 = -b_{66} (u_{1,2}^{(0)} + u_{2,1}^{(0)}) - 2\gamma_{66} u_{3,12}^{(0)}$$

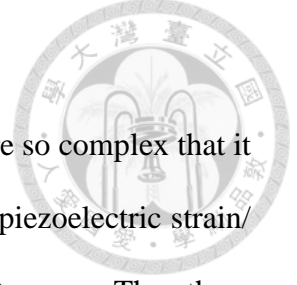
where

$$\gamma_{11} = \frac{c_{11}^p}{12} (l_c^3 + 3l_c l_m^2) + \frac{\hat{c}_{11}^p}{12} (l_m^3 + 3l_c^2 l_m)$$

$$\gamma_{12} = \frac{c_{12}^p}{12} (l_c^3 + 3l_c l_m^2) + \frac{\hat{c}_{12}^p}{12} (l_m^3 + 3l_c^2 l_m)$$

$$\gamma_{66} = \frac{c_{66}^p}{12} (l_c^3 + 3l_c l_m^2) + \frac{\hat{c}_{66}^p}{12} (l_m^3 + 3l_c^2 l_m) = \frac{(\gamma_{11} - \gamma_{12})}{2}$$





However, the tensors in the piezoelectric constitutive equation are so complex that it is difficult for calculation or analysis in a real case. For example, the piezoelectric strain/charge constant is a 3x6 tensor, and the elastic stiffness matrix is a 6x6 tensor. Thus there are some assumptions for easier calculation. Based on the thin plate structure, in the material, the longitudinal stress  $T_3$  and shear force  $T_4, T_5$  are much smaller than other stress at other directions. Thus  $T_3, T_4$  and  $T_5$  are negligible in (equation 3-4). Furthermore, the electric field is generally across the top and bottom electrodes, so only the longitudinal electric field  $E_3$ , should be considered. Then (equation 3-4) can be simplified to (equations 3-12 and 3-13):

$$\begin{cases} \begin{bmatrix} T_1 \\ T_2 \\ T_6 \end{bmatrix} = [c] \begin{bmatrix} S_1 \\ S_2 \\ S_6 \end{bmatrix} - [c] \begin{bmatrix} E_3 d_{31} \\ E_3 d_{32} \\ E_3 d_{33} \end{bmatrix} \\ D_3 = \epsilon_{33} E_3 + d_{31} T_1 + d_{32} T_2 \end{cases} \quad (3-12)$$

where  $[c]$  is a simplified elastic stiffness matrix, which is only related to Young's modulus ( $Y$ ) and Poisson ratio ( $\nu$ ), for an isotropic piezoelectric material:

$$[c] = \begin{bmatrix} Y/(1-\nu^2) & \nu Y/(1-\nu^2) & 0 \\ \nu Y/(1-\nu^2) & Y/(1-\nu^2) & 0 \\ 0 & 0 & Y/2(1+\nu) \end{bmatrix} \quad (3-13)$$

For a unimorph piezoelectric plate, the  $x$ - and  $y$ - directional deformation can be

represented  $u = u_o - z \frac{\partial w}{\partial x}$  as and  $v = v_o - z \frac{\partial w}{\partial y}$  in (Figure 3-6). The strain tensor can be

written as (equation 3-14). After substituting (equation 3-14) into (equation 3-12), it can be rewritten as (equation 3-15).



$$\begin{aligned} \begin{bmatrix} S_1 \\ S_2 \\ S_6 \end{bmatrix} &= \begin{bmatrix} \partial u / \partial x \\ \partial v / \partial y \\ \partial u / \partial y + \partial v / \partial x \end{bmatrix} = \begin{bmatrix} S_1^o \\ S_2^o \\ S_6^o \end{bmatrix} + z \begin{bmatrix} k_1 \\ k_2 \\ k_6 \end{bmatrix} \\ &= \begin{bmatrix} \partial u_o / \partial x \\ \partial v_o / \partial y \\ \partial u_o / \partial y + \partial v_o / \partial x \end{bmatrix} + z \begin{bmatrix} -\partial^2 w / \partial x^2 \\ -\partial^2 w / \partial y^2 \\ -2\partial^2 w / \partial x \partial y \end{bmatrix} \end{aligned} \quad (3-14)$$

$$\begin{cases} T_1 \\ T_2 \\ T_6 \end{cases} = [c] \begin{bmatrix} S_1^o \\ S_2^o \\ S_6^o \end{bmatrix} + z [c] \begin{bmatrix} k_1 \\ k_2 \\ k_6 \end{bmatrix} - E_3 [c] \begin{bmatrix} d_{31} \\ d_{32} \\ d_{36} \end{bmatrix} \quad (3-15)$$

$$D_3 = \varepsilon_{33} E_3 + d_{31} T_1 + d_{32} T_2$$

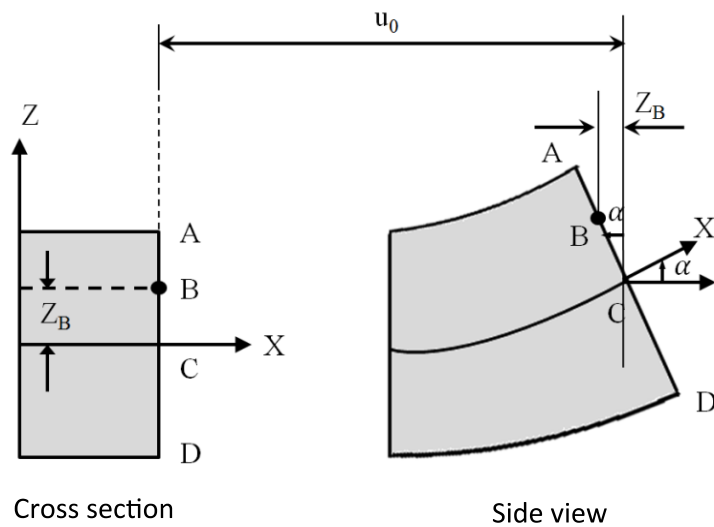
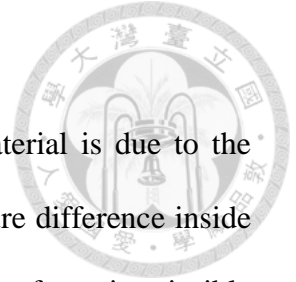


Figure 3-6. The unimorph piezoelectric plate (a) before and (b) after deformation.



### 3.2.2 Laplace pressure

A commonly observed interfacial curvature in an isotropic material is due to the interfacial tension. The Young-Laplace equation represents the pressure difference inside and outside the curvature (Figure 3-7) [128]. Considering an interface of two immiscible fluids at an equilibrium state, the net force (equation 3-16) of a segment  $S$  of the interface can be represented as the pressure difference plus the net surface tension along the closed curve  $C$ . Let  $\mathbf{t}$  and  $\mathbf{n}$  are the tangent and normal units of the curve.

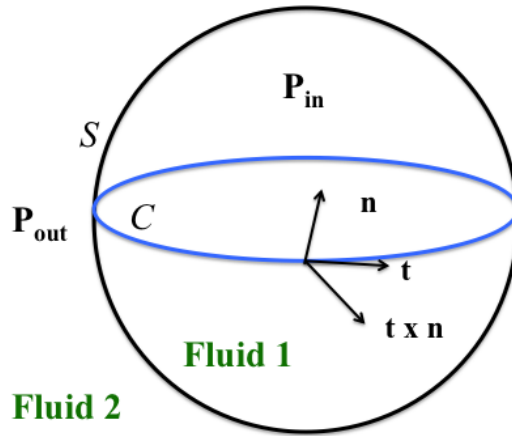
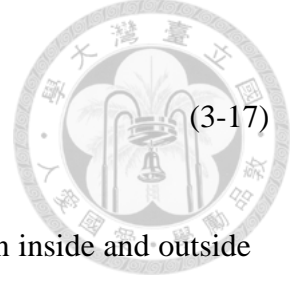


Figure 3-7. Interface between two immiscible fluids.

$$F = \int_S (P_{in} - P_{out}) \mathbf{n} dS + \gamma \oint_C \mathbf{t} \times \mathbf{n} dr \quad (3-16)$$

Because the interface has negligible volume, so the body forces can be ignored; and the viscous forces can be neglected, since both fluids are static. Thus the net force must be zero in (equation 3-16) where  $\gamma$  is surface tension. Applying Stokes' theorem to curve  $C$ , the net surface tension can be written as (equation 3-17):

$$\begin{aligned} \gamma \oint_C \mathbf{t} \times \mathbf{n} dr &= \gamma \int_S [(\nabla \mathbf{n}) \cdot \mathbf{n} - (\nabla \cdot \mathbf{n}) \mathbf{n}] dS \\ &= -\gamma \int_S (\nabla \cdot \mathbf{n}) \mathbf{n} dS \end{aligned} \quad (3-17)$$



Combining with (equation 3-16), the pressure difference between inside and outside of the interface can be solved in (equation 3-18). This relation is generally known as the Young-Laplace equation, and  $\nabla \cdot \mathbf{n}$  means the local mean curvature of the interface.

$$\begin{aligned} \int_S [(P_{in} - P_{out})] - \gamma (\nabla \cdot \mathbf{n}) \mathbf{n} dS &= 0, \\ P_{in} - P_{out} &= \gamma \nabla \cdot \mathbf{n} \end{aligned} \quad (3-18)$$

For a curved surface with radius  $R$ , the inward and outward pressure difference equals to  $2\gamma / R$ . For a bubble, the surface tension force downward around circle is twice the surface tension times the circumference, which is  $4\gamma / R$ , since there are two surfaces contribute to the force.

### 3.3 Simulation

In this chapter, we to design a worm trapper by two phases flow in microfluidic channels. For more understanding the fluidic phenomenon, some simulation results were discussed by using COMSOL Multiphysics® Modeling Software. At the beginning, we set a  $\pi$ -structure for analyzing the oil bulges expansion at the junction with different oil (FC-43) input pressures. The fluidic parameters are in (Table 3-3). The inlet and outlet pressures of the water were both set in an atmospheric condition, and the oil inlet pressure was from 103100 Pa to 104300 Pa. The trapping time was stop at 0.005 second, which is much faster than the *C. elegans* swimming velocity ( $\sim 0.2$  mm/s) [129, 130]. In (Figure

3-8), the expanding oil bulges pushed the water outward; and the bulges completely sealed the water channel if the oil inlet pressure is larger than 104300 Pa (Figure 3-9).

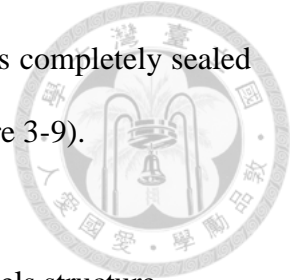
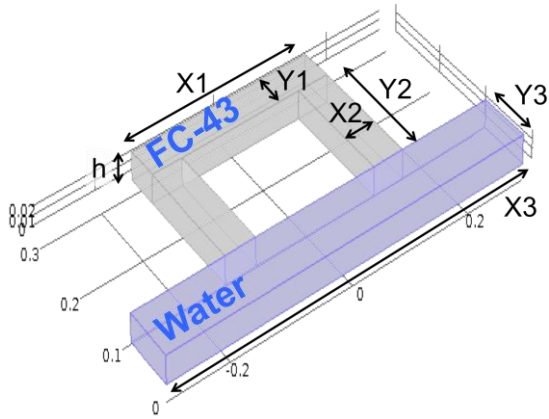


Table 3-3. Specifications and material properties of the  $\pi$ -channels structure.



Fluid properties	Symbol	Size (mm)
Water	X3	0.6
Density ( $\text{kg/m}^3$ ): 1000	Y3	0.08
Dynamic viscosity ( $\text{Pa}\cdot\text{s}$ ): 0.001	h	0.03
	X1	0.3
FC-43	X2	0.05
Density ( $\text{kg/m}^3$ ): 1860	Y1	0.05
Dynamic viscosity ( $\text{Pa}\cdot\text{s}$ ): 0.0047	Y2	0.17
	h	0.03

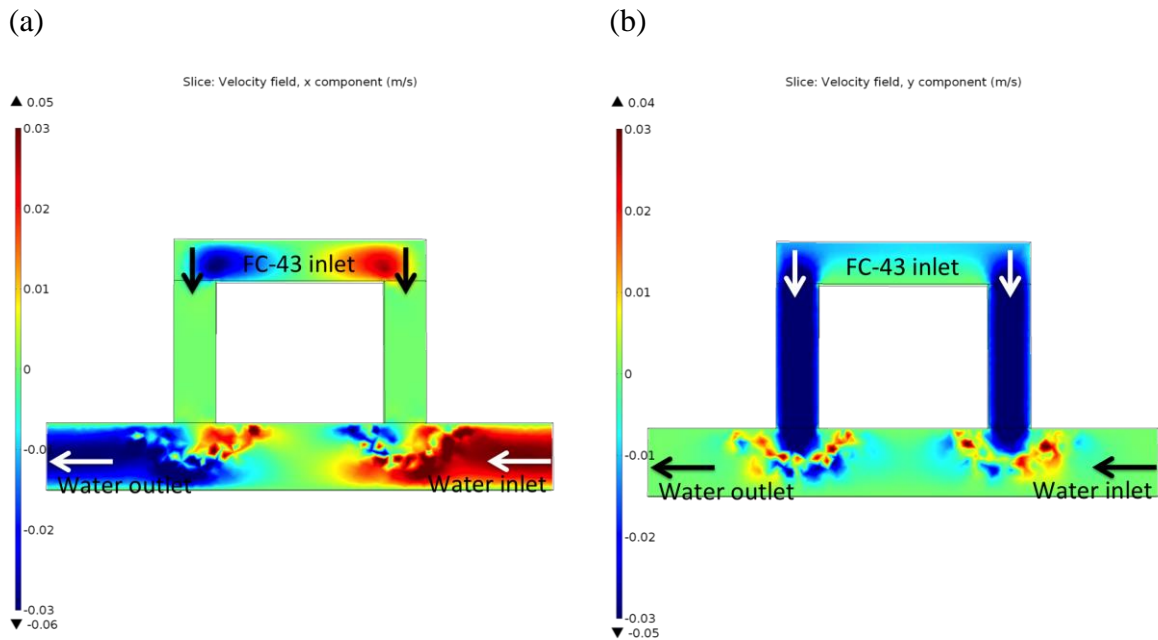
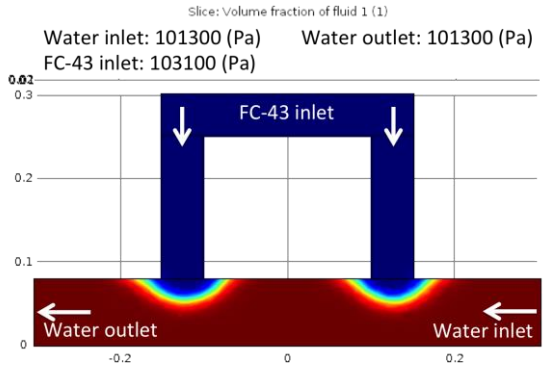
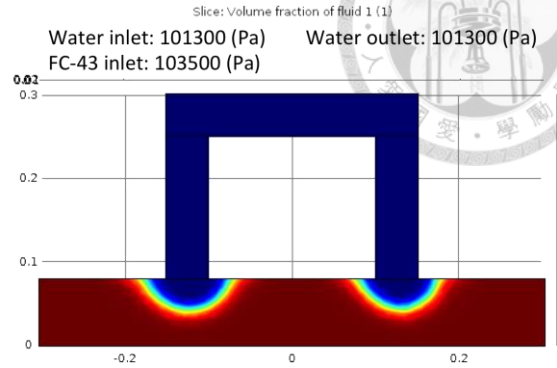


Figure 3-8. The  $x$ - and  $y$ -directional velocities, (a)  $u$  and (b)  $v$ , when the oil bulges expand from inlet pressure 103500 Pa at time=0.005s.

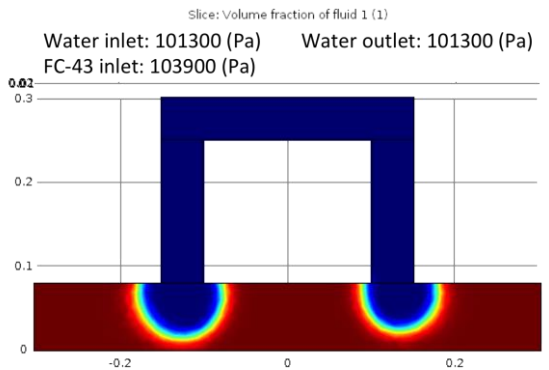
(a)



(b)



(c)



(d)

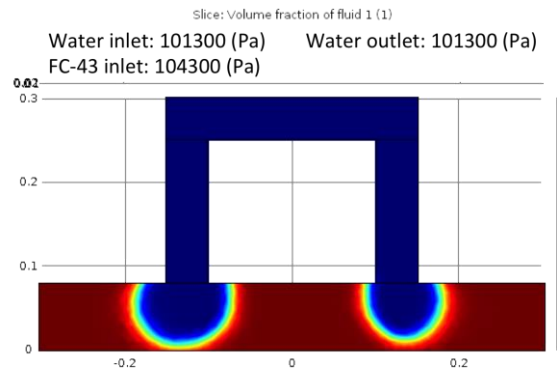


Figure 3-9. The volume fraction of water and oil bulges with different oil inlet pressures (103100 Pa, 103500 Pa, 103900 Pa, 104300 Pa) at 0.005 second.

In next simulation, we set the oil pressure as 104300Pa, which can totally block the static water channel. We then change the water inlet pressure from 102700 Pa to 105100 Pa. In a flowing water channel, the oil bulges are difficult to expand. If the water pressure is too high, the oil might even shrink back to the  $\pi$ -channels (Figure 3-10). Thus with the same oil inlet pressure, the biggest bulges can be made in a static water channel.

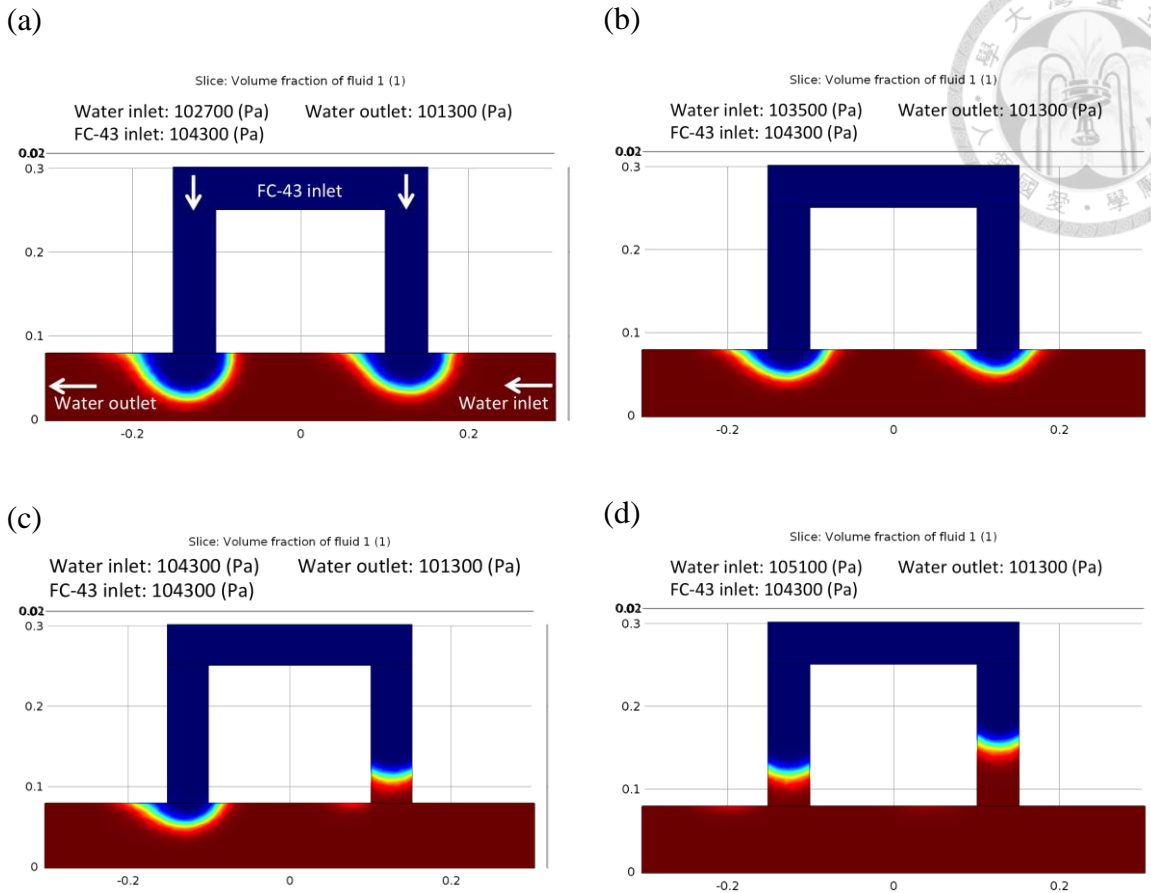


Figure 3-10. The volume fraction of water and FC-43 droplets with different water inlet pressures (102700, 103500 Pa, 104300 Pa, 105100 Pa) at 0.005 second.

However in a real case, the Laplace pressure theory should be considered. It happens when the roughness of the two parallel channels surfaces are different (Figure 3-11a). This difference makes one big and one small bulge at the beginning. Because the pressure is inversely proportional to the droplet curvature, the pressure is smaller in the larger droplet. Thus the oil flows from the small droplet to the big one. Finally, the big one unlimitedly expands until it blocks the water channel (Figure 3-11b).

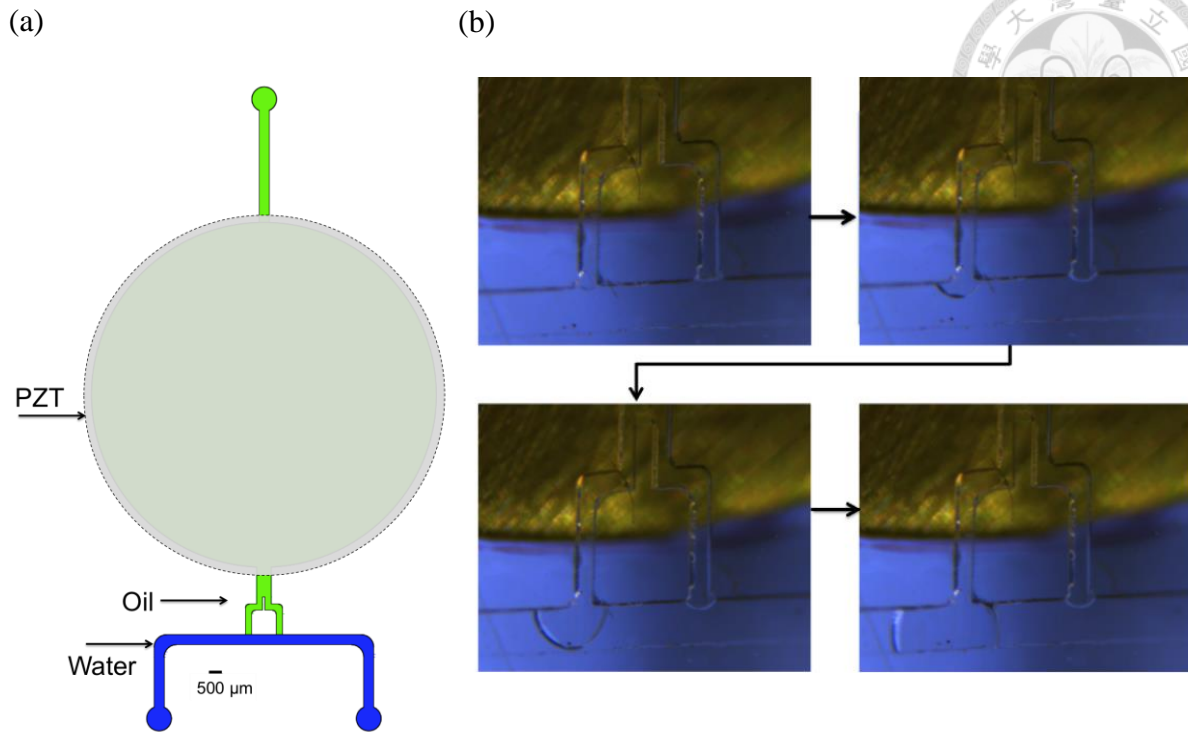


Figure 3-11. (a) The structure of the  $\pi$ -channel structure. (b) A real case of an extremely large bubble blocking the water channel due to Laplace pressure.

To solve the Laplace pressure issue, we modified the  $\pi$ -structure to be a donut shape. The pushing ability of a PZT plate, which can generate  $\sim 10^5$  Pa pressure with  $\sim 70$   $\mu\text{m}$  central deformation in one millisecond was simulated [131, 132]. (Figure 3-12) shows the central deformation at different applied voltages. (Figure 3-13a) shows the flow velocity after triggering the PZT. With a central pillar, the flow was separated from one to two streams when it hit the pillar. It is clear that these two streams are almost independent to push the water out of the channels. Finally, a water droplet was made at the bottom of the donut structure. However, in real testing, the response time is very short during the making of the water droplet (in millisecond scale). Sometimes the droplet shifted a little toward the left or the right side, it means the flow velocities are not symmetric in a few



milliseconds around the pillar (Figure 3-13b). This might pose a potential risk of losing the worm. To improve the donut structure, we added three symmetric fingers at the bottom (Figure 3-13c). When compared to the donut structure, the pushing velocity happened only at the upper half of the donut. In the fingers-donut structure, the pushing velocity went deeper toward the lower half of the donut. It means that we have more opportunity to keep a symmetric water droplet at the bottom (Figure 3-13d).

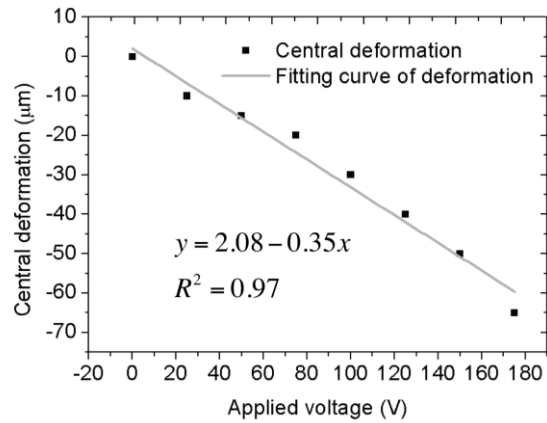
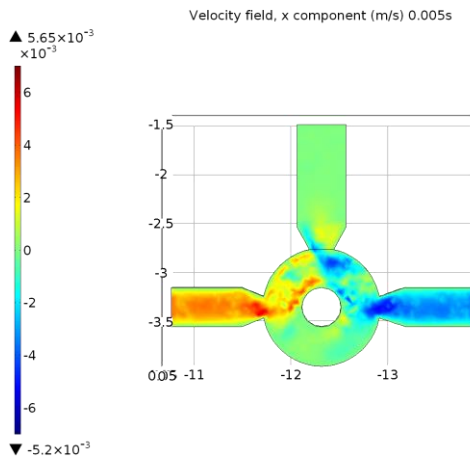


Figure 3-12. The deformation measurement from laser vibrometer (Keyence, LK-H080).

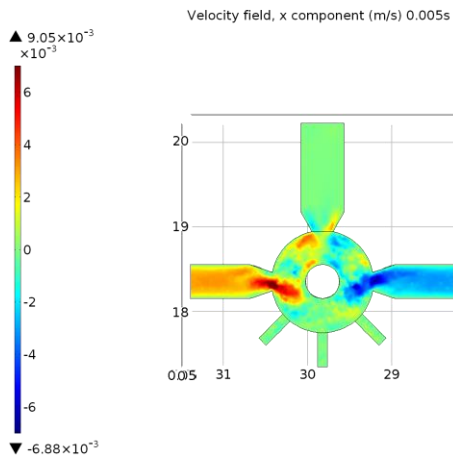
(a)



(b)



(c)



(d)

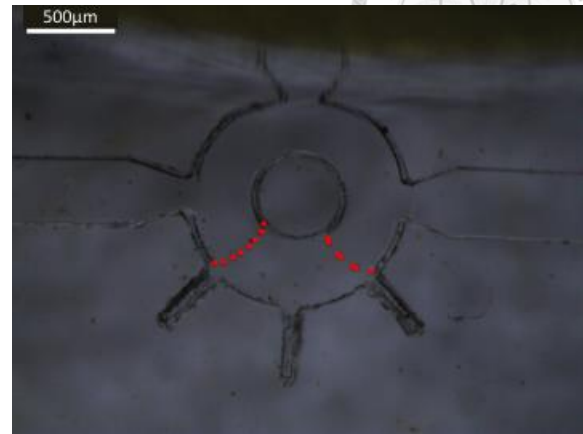


Figure 3-13. The x-directional velocity simulation of (a) the donut structure and (c) the fingers-donut structure with 150μm channel height. The water is static, and the oil inlet pressure is 261300 Pa. Figure (b) and (d) are the photos with water droplet at the bottom in the donut and 45° fingers-donut structure, respectively.

The time dependent water flow from 0.001 s to 0.005 s in the donut structure and the fingers-donut structure was simulated in (Figure 3-14 and 3-15). In the donut structure, the direction and the value of the flow velocity at the junctions were similar from start to 0.005 s. The water in the donut was continuously pushed outside, and it was almost static at the bottom. Because in microfluidic devices, the flow rate is zero at the channel walls, the lower half circle of the donut is almost static. Regarding the fingers-donut structure, besides the velocity was much larger; the flow was more active in the lower half donuts. The reason is that the flow rate is not zero at the opening end of these fingers. It's clear to see at the beginning, i.e.,  $t=0.001s$ , immediately after the pressure came from the oil inlet, the oil went outward and downward.

Considering the three fingers spread with  $30^\circ$ ,  $45^\circ$  and  $60^\circ$  in (Figure 3-15) for finding the optimal structure to make sure trapping *C. elegans* in the donut. In the  $30^\circ$  fingers-donut channel, although the flow went downward to the lower half of circle, making an active fluidic field around the fingers. The flow was still unstable at 0.005s might has difficulty forming water droplet with *C. elegans* inside. For the spreading angles of  $45^\circ$  and  $60^\circ$ , their flows were also active at beginning then tended to be stable finally. Furthermore, comparing these results at 0.005s, the flow went deeper in the  $45^\circ$  fingers-donut (Figure 3-16). Thus we verified that the  $45^\circ$  fingers-donut structure provides the best efficiency to trap *C. elegans*.

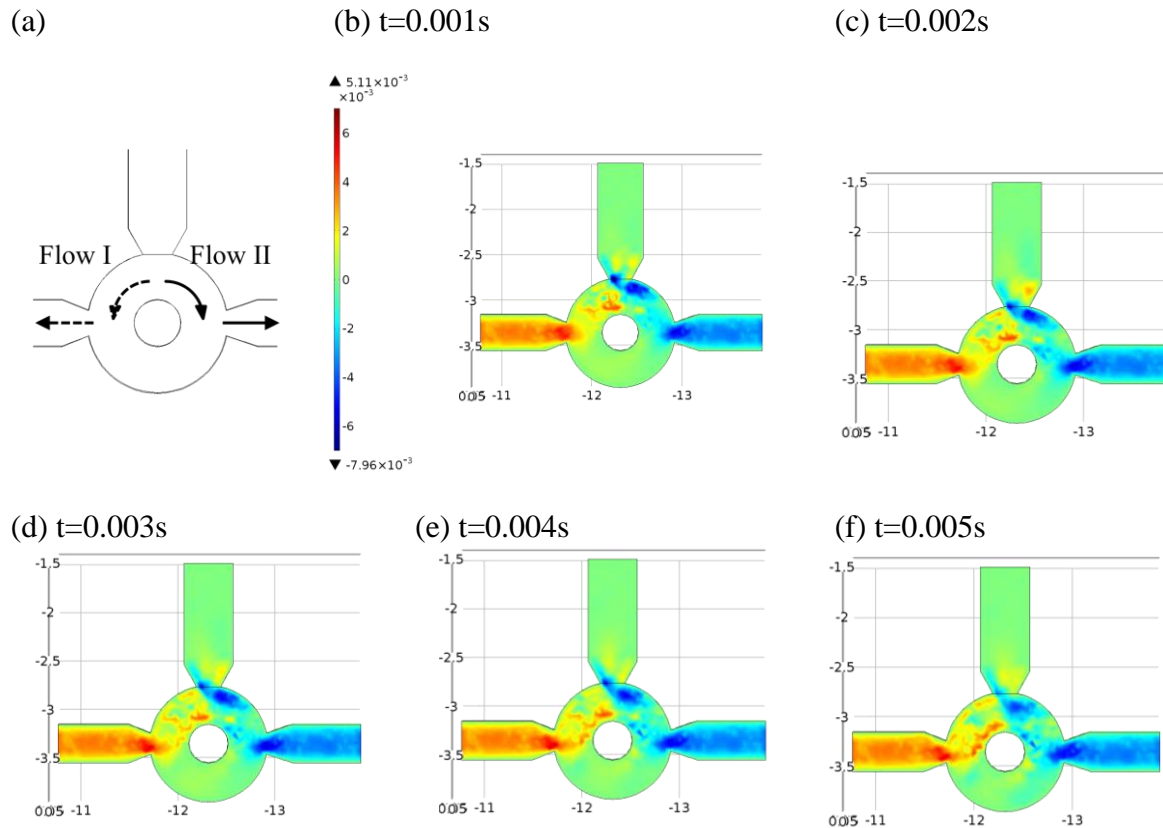
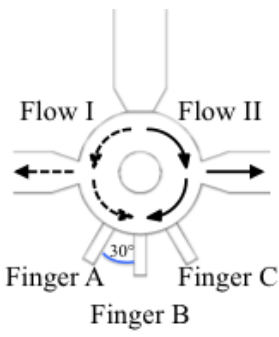
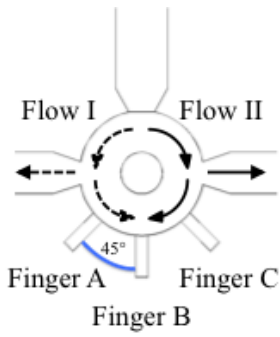
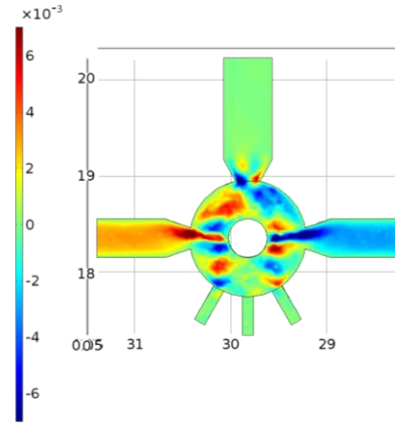


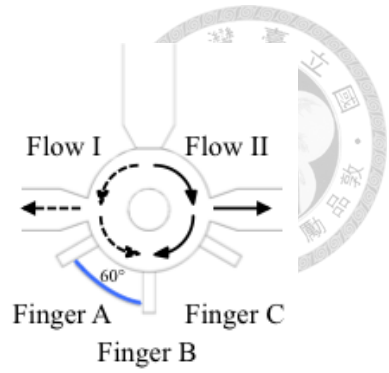
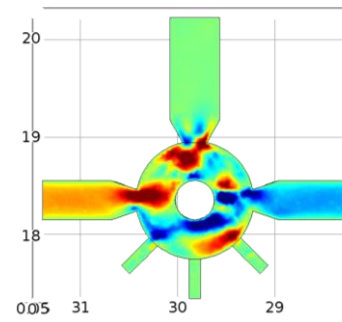
Figure 3-14. (a) The flow direction in the donat. (b)~(f) The pushing flow velocity of the donut structure from 0.001 s to 0.005 s.



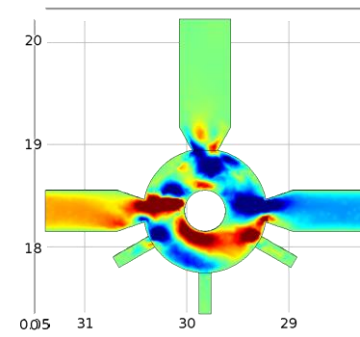
t=0.001s



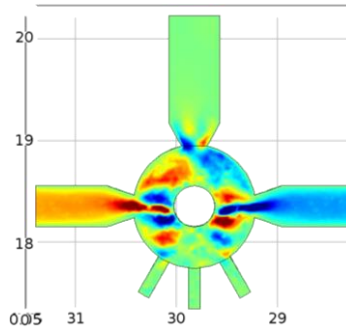
t=0.001s



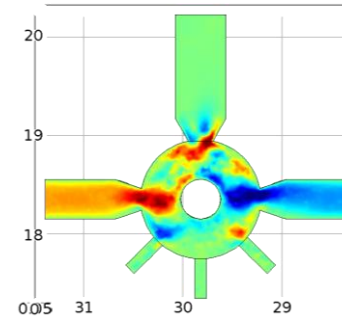
t=0.001s



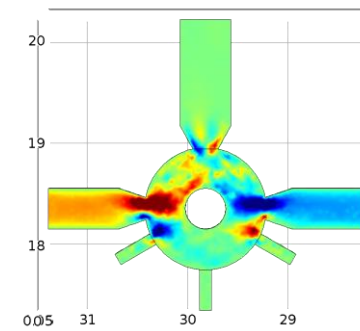
t=0.002s



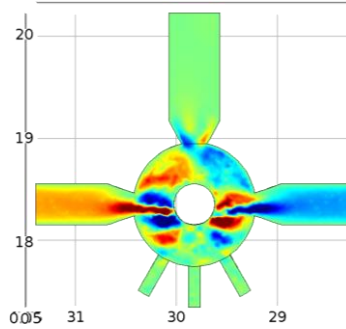
t=0.002s



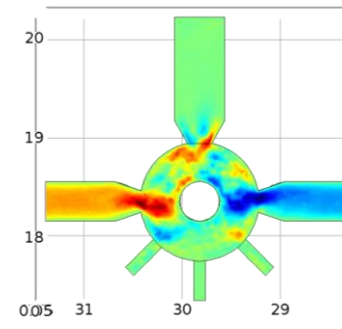
t=0.002s



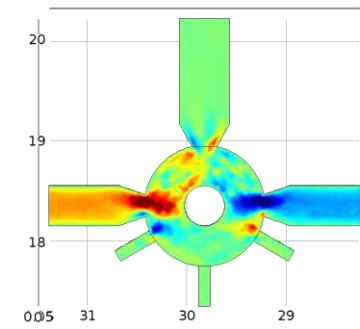
t=0.003s



t=0.003s



t=0.003s



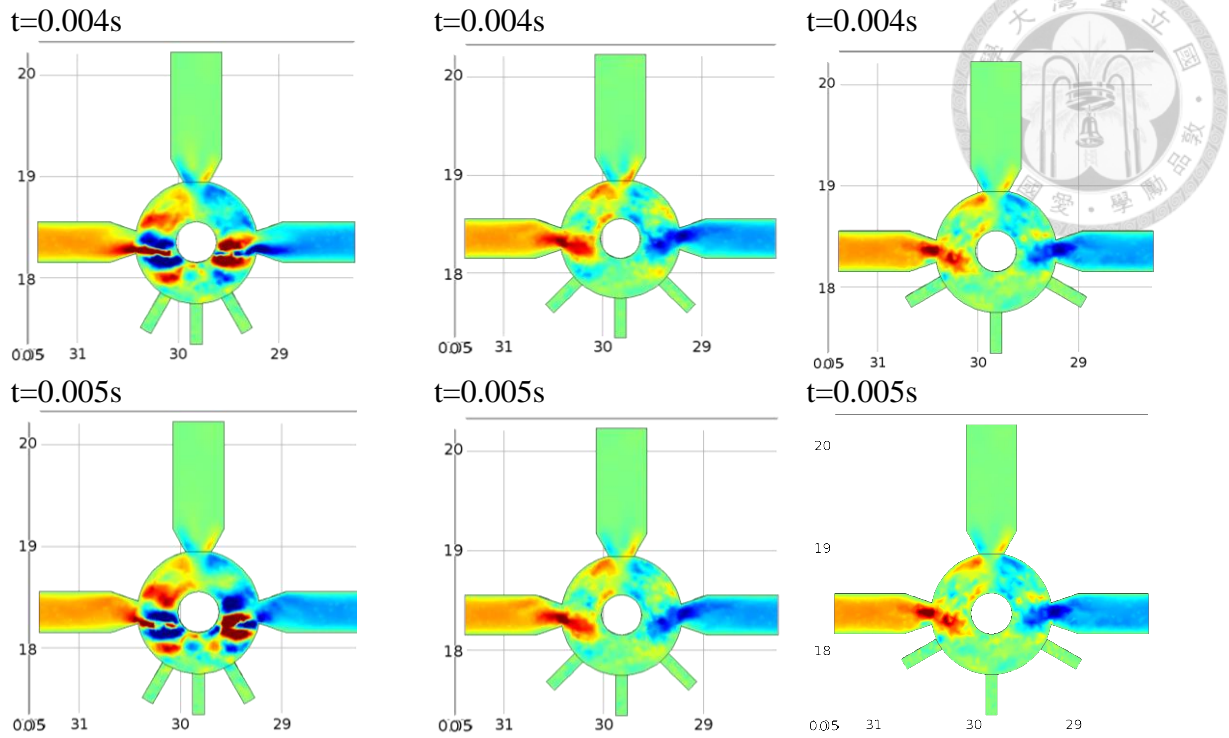


Figure 3-15. The flow direction in the donut. And the pushing flow x-directional velocity of the 30°, 45°, and 60° fingers-donut structures from 0.001 s to 0.005 s.

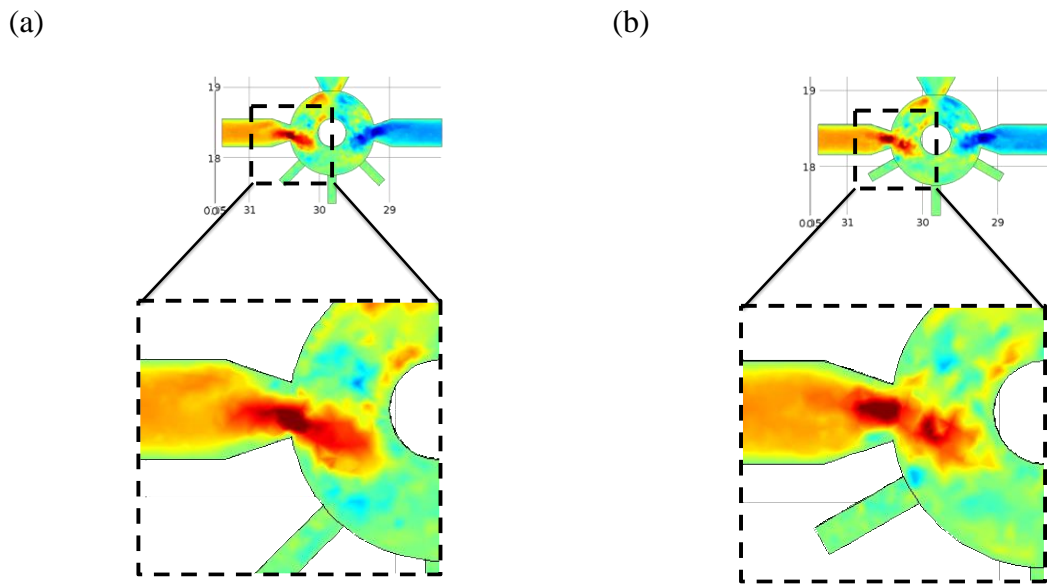


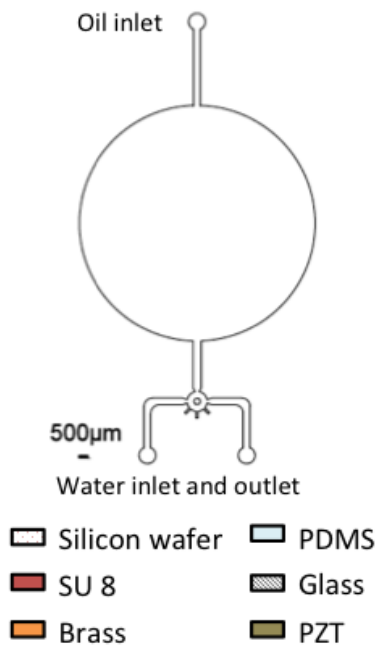
Figure 3-16. The comparison of the flow at the junctions of (a) 45° and (b) 60° fingers-donut structure at 0.005s.

### 3.4 Device fabrication

Based on the simulation results, a fingers-donut microfluidic structure was fabricated by using the photolithographic process (Figure 3-17). In this structure, there was one inlet for oil and a pair of inlet and outlet for water. The channel height was about 150  $\mu\text{m}$ , which was suitable for an adult worm with a 100  $\mu\text{m}$  diameter. In step 1, the microfluidic channel was made of a negative photoresist SU8-3050. The photolithographic processes were carried out using a conventional spin coating, a hotplate, and a mask aligner (MA6/BA6 mask aligner, Karl Suess Wetzlar GmbH, Germany). The fabrication parameters were taken from the Microchem Corp. manual (MA, USA). The surface was then modified by silane vapor as a releasing agent. Step 2 is the soft lithography of PDMS (Silgard 184 A&B, Biesterfeld Spezialchemie GmbH). A small amount of PDMS (A: B=10: 1) was mixed and vacuumed for a while before pouring slowly onto the negative channel mode. The PDMS turned to solid after two hours in a 60 degree C oven. In step 3, the PDMS was peeled off, and three  $\phi = 1$  mm inlet/ outlet holes and one  $\phi = 14$  mm, h= 2 mm chamber were drilled. In the last step, the PDMS was bonded onto a slice of glass substrate by oxygen plasma treatment. Finally, the PZT buzzer was glued onto the chamber with PDMS gel.



(a)



(b)

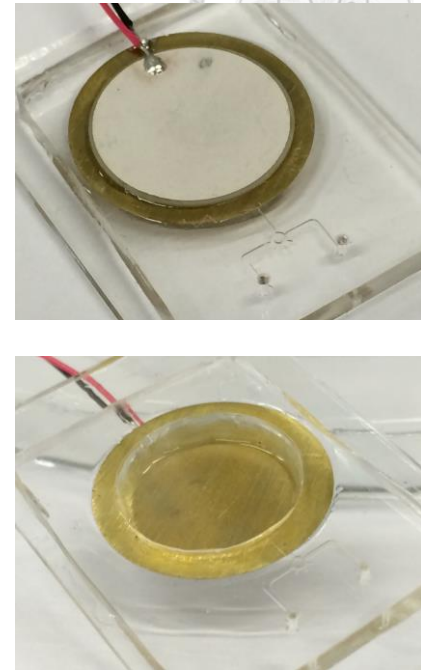


Figure 3-17. (a) The fabrication process to make a microfluidic channel device with the fingers-donut structure. (b) Photos of the front and back view of the fingers-donut structure with 150  $\mu$ m channel height.

### 3.5 Experimental results

For making the water/oil interface in the device, two syringe pumps separately pumped the oil and water into the device. The oil was first flow from the oil inlet. Including the big chamber, all channels and even the fingers structure were filled by oil due to PDMS's hydrophobic property (Figure 3-18a). Next, decreasing the oil flow rate while start pumping the water from the water inlet, leads to the situation that oil was pushed out of the outlet (Figure 3-18b). Next, slowly decrease the two pumping flow rates while all the plastic tubes were disconnected after the interface achieve balance. Finally a PDMS cylinder with a 1 mm diameter was used to block the oil inlet (Figure 3-18c).

The experiments were done under a microscope. The worm was carefully picked from the petri dish and was helped to swim into the channel by a pipette (Figure 3-19a). When it swam at the lower half of the circle, the voltage was switched on by a DC voltage amplifier (model 2210, Trek). Immediately the oil quickly pushed the water outside, and the worm was trapped inside the water droplet (Figure 3-19b). A little amount of oil should be dipped at the inlet and outlet before switch off the voltage supply. Finally, the water inlet and outlet by PDMS cylinders were blocked. The worm stayed still inside the water droplet, which is covered by oil (Figure 3-19c). Finally, all plastic fluidic tubes and electric connections were released. This device is convenient for further measurements in some instrument that is equipped with a narrow measurement space.

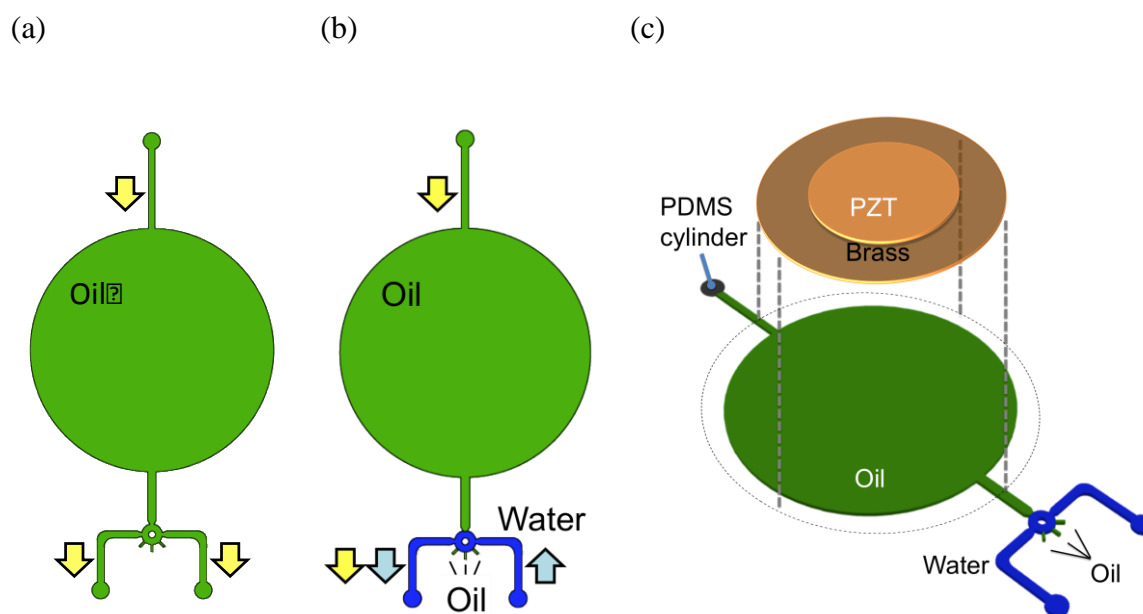
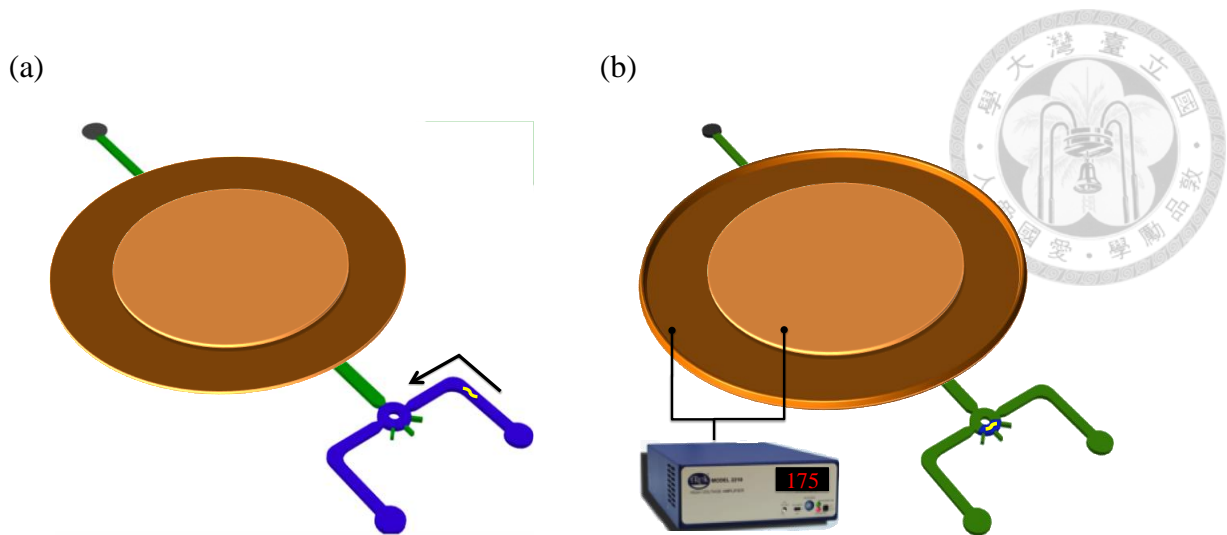


Figure 3-18. The steps of making oil/ water interface. (a) Let oil fill anywhere in the channel, and then (b) pumping water into the channel. (c) The schematic of the device and the initial oil/ water interface after blocking the oil inlet.





(c)

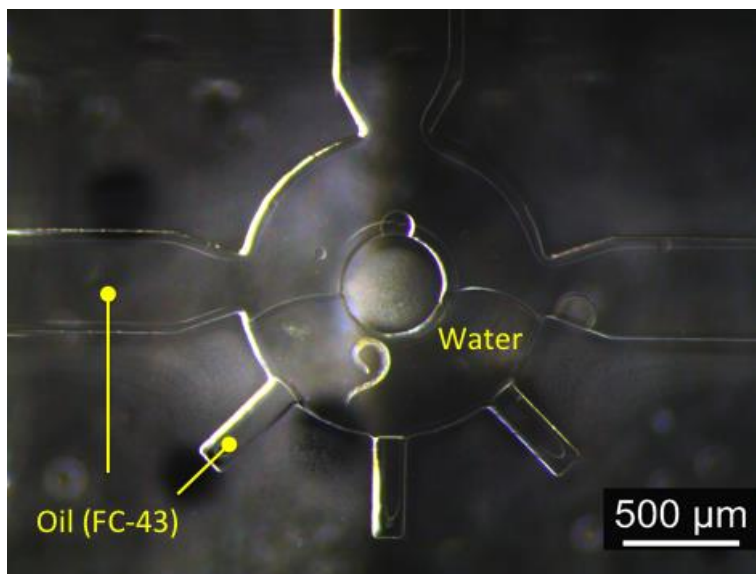


Figure 3-19. Schematic of the worm that was (a) pumped by the pipette and swam into the donut structure and (b) trapped inside the water droplet. (c) The microscope image of a trapped living worm in a water droplet.



### 3.6 Discussion and future work

In this study, an easily fabricated worm trapper was proposed by integrating PZT plate in a PDMS microfluidic device. The PZT plate provides large force in a short time, and without any outwards connection, the device is convenient for such equipment with limited measurement space. For example, this device is particular useful for the nuclear magnetic resonance (NMR) instrument as it has stringent space and material restrictions on the device and the holder. That is, the device and the holder must have negligible signal intensity, which provides an assurance that the spectrum signal only comes from the specimen. Unfortunately the PDMS has a strong peak in the NMR spectrum (Figure 3-20), thus this device presented can only be used to take NMR images. To make spectrum measurement, materials such as PMMA rather than PDMS must be used.

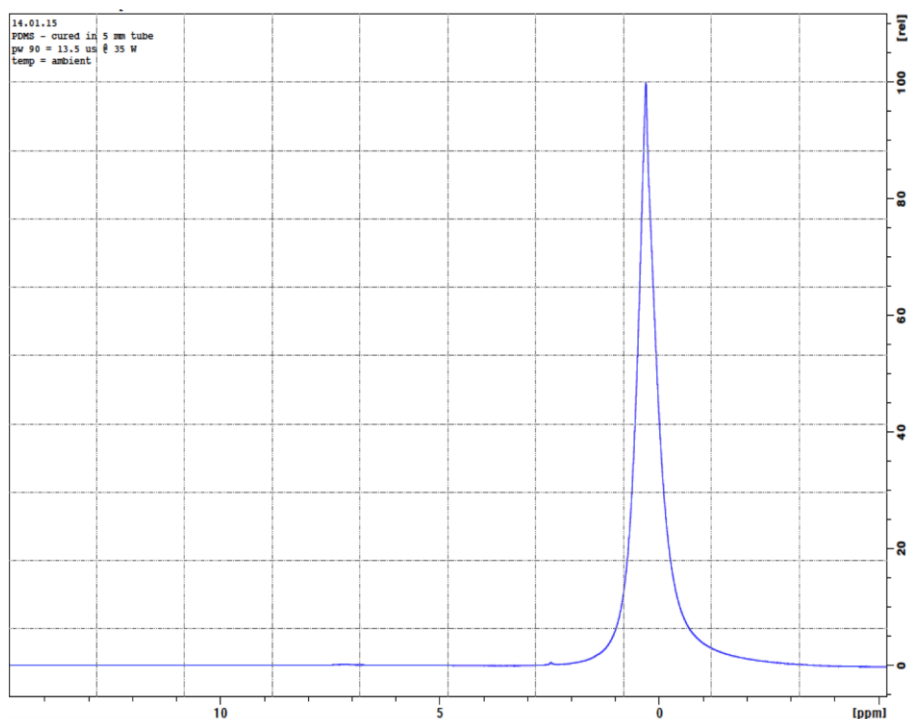


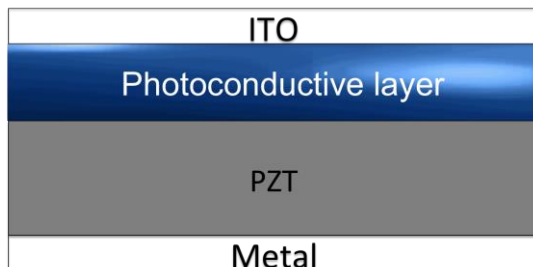
Figure 3-20. The NMR spectrum of a tube of cured PDMS.

## Chapter 4. Optopiezoelectric material



In this chapter, a novel photosensitive piezoelectric composite was proposed. The piezoelectric properties of this composite can be modulated by light. The material structures can be a “double-layers” configuration by coating photoconductive material onto a piezoelectric laminate, or a “single-layer” configuration by mixing photoconductive molecular inside piezoelectric polymer (Figure 4-1). For the double-layers structure, these fast response photosensitive materials films, such as spiropyran/ liquid (SP/ LC) and TiOPc, should be tightly attached onto the piezoelectric plates with an optimal film thickness. The thickness of these photoconductive films is closely related to their photoconductive response [73]. In the single-layer structure, the photoconductive powders are uniformly mixed within the polymeric films. This structure is flexible, thinner, lighter, and easier to fabricate than the two layers structure. However, the powders uniformity and the photoconductive response must be carefully controlled. This chapter will introduce the performance of an optopiezoelectric actuator, which made of SP/ LC and PZT double-layers structure. And the physical properties of an optopiezoelectric sensor, which composed of P(VDF-TrFE) and TiOPc in a single-layer structure configuration are also discussed.

(a)



(b)

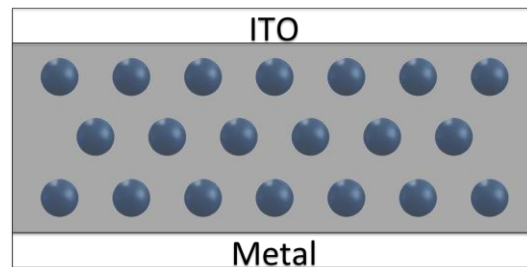




Figure 4-1. The (a) double-layers and (b) single-layer photoconductive piezoelectric composite structures.

## 4.1 Optopiezoelectric actuator

The deformation of a double-layers (SP/ LC - PZT) optopiezoelectric actuator can be modulated by light. Due to the chemical structure transition of spiropyran, this section shows the changes of optical absorbance spectra, electrical impedance and the deformation before and after UV illumination.

### 4.1.1 Experimental setup

The SP/ LC liquid was made of the spiropyran (Sigma-Aldrich Co.), which was oriented by the rod-like liquid crystals (type E7, Merck KGaA). The SP/ LC was filled into a square cell for measuring optical and electrical properties. The 50  $\mu\text{m}$  space is covered by a pair of top and bottom ITO electrodes (5 mm x 5 mm). With capillary attraction, the light purple color SP/ LC liquid expanded inside the space. The color turns darker with UV illumination from a medical UV lamp ( $\sim 4$  W) (Figure 4-2).

(a)



(b)

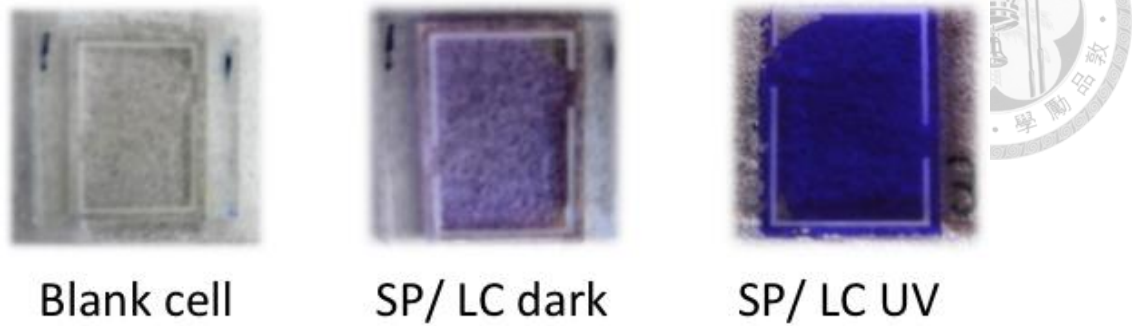


Figure 4-2. (a) The cell structure and (b) the SP/ LC color changes with UV illumination.

With the SP/LC changes its color, its optical and electrical properties also vary. The optical spectra were measured using a UV-Vis spectrometer (Lambda 900 spectrometer, PerkinElmer). The electrical impedance was obtained from an impedance analyzer (4294A, Agilent) at 1 volt input. Furthermore, the light modulated deformation was measured by a non-contact laser Doppler interferometers called Advanced Vibrometer/Interferometer Device (AVID) [133, 134].

AVID system was designed for single point vibration measurement (Figure 4-3). The linear polarized He-Ne laser beam (633nm) was split by the polarization beam splitter (PBS1). The reference beam passed through the quarter wave plate (QWP1) to be a right circularly polarized light beam. Another objective beam passed through a QWP2 to become left circularly polarized, which was orthogonal to the reference beam. When the two orthogonal circularly polarized light beams reflected back, they passed through the QWP1 and QWP2 again to become orthogonal linearly polarized beams. The two beams with same intensity passed through PBS1 again and then went into the quadrature detector.

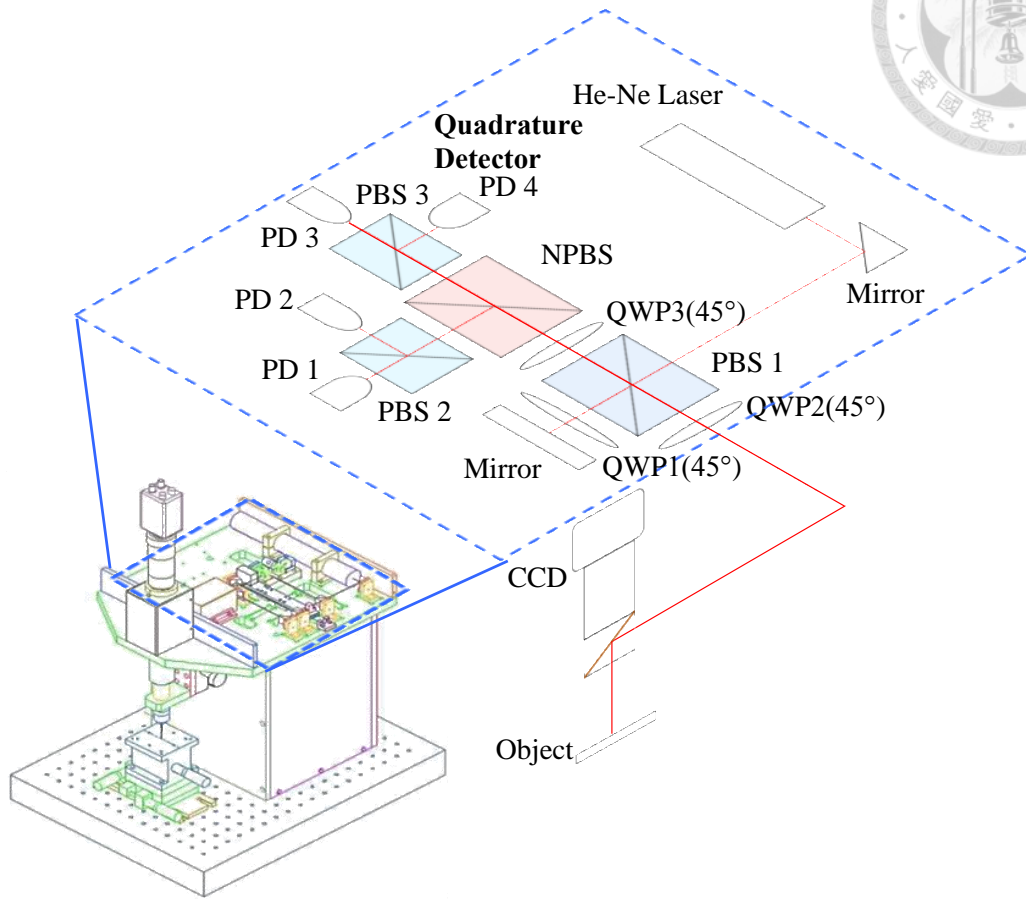


Figure 4-3. AVID system and its opto-mechanical setup.

The quadrature detector signals were analyzed by Jone's calculus below. In the quadrature detector, the electrical field  $E_a$  and  $E_b$  were the returning beams from mirror and the object,  $E$  is the recombination beam after the QWP3. And  $f$  is the frequency of the incident laser beam;  $f_{d1}$  and  $f_{d2}$  are caused by the specimen motion (equation 4-1).



$$E_1 = \begin{bmatrix} 1 \\ 0 \end{bmatrix} e^{i2\pi(f+f_{d1})t}$$

$$E_b = \begin{bmatrix} 1 \\ 0 \end{bmatrix} e^{i[2\pi(f+f_{d2})t+\phi]}$$

$$E = \left\{ \begin{bmatrix} 1 \\ -i \end{bmatrix} e^{i2\pi f_{d1}t} + \begin{bmatrix} i \\ 1 \end{bmatrix} e^{i(2\pi f_{d2}t+\phi)} \right\} e^{i2\pi ft} \propto \begin{bmatrix} \cos(\beta_1 - \beta_2)/2 \\ \sin(\beta_1 - \beta_2)/2 \end{bmatrix}$$

$$\text{where } (\beta_1 - \beta_2)/2 = [2\pi(f_{d1} - f_{d2})t + \Delta\phi]/2$$

The four beam signals  $E_{1,2,3,4}$  and intensities  $I_{1,2,3,4}$  were detected by PD1 to PD4 after splitting by the NPBS and PBSs (equation 4-2).

$$E_1 \propto \begin{bmatrix} 1 & 0 \\ 0 & 0 \end{bmatrix} \begin{bmatrix} \cos(\beta_1 - \beta_2)/2 \\ \sin(\beta_1 - \beta_2)/2 \end{bmatrix} = \begin{bmatrix} \cos(\beta_1 - \beta_2)/2 \\ 0 \end{bmatrix}$$

$$I_1 \propto E_1 \propto \cos^2[(\beta_1 - \beta_2)/2] \propto 1 + \cos(\beta_1 - \beta_2)$$

$$E_2 \propto \begin{bmatrix} 0 & 0 \\ 0 & 1 \end{bmatrix} \begin{bmatrix} \cos(\beta_1 - \beta_2)/2 \\ \sin(\beta_1 - \beta_2)/2 \end{bmatrix} = \begin{bmatrix} 0 \\ \sin(\beta_1 - \beta_2)/2 \end{bmatrix}$$

$$I_2 \propto E_2 \propto \sin^2[(\beta_1 - \beta_2)/2] \propto 1 - \cos(\beta_1 - \beta_2)$$

$$E_3 \propto \begin{bmatrix} 1 & 1 \\ 1 & 1 \end{bmatrix} \begin{bmatrix} \cos(\beta_1 - \beta_2)/2 \\ \sin(\beta_1 - \beta_2)/2 \end{bmatrix} = \begin{bmatrix} \cos(\beta_1 - \beta_2)/2 + \sin(\beta_1 - \beta_2)/2 \\ \cos(\beta_1 - \beta_2)/2 + \sin(\beta_1 - \beta_2)/2 \end{bmatrix}$$

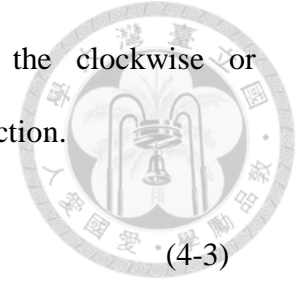
$$I_3 \propto E_3 \propto 1 + \sin(\beta_1 - \beta_2)$$

$$E_4 \propto \begin{bmatrix} 1 & -1 \\ -1 & 1 \end{bmatrix} \begin{bmatrix} \cos(\beta_1 - \beta_2)/2 \\ \sin(\beta_1 - \beta_2)/2 \end{bmatrix} = \begin{bmatrix} \cos(\beta_1 - \beta_2)/2 - \sin(\beta_1 - \beta_2)/2 \\ -\cos(\beta_1 - \beta_2)/2 + \sin(\beta_1 - \beta_2)/2 \end{bmatrix}$$

$$I_4 \propto E_4 \propto 1 - \sin(\beta_1 - \beta_2)$$

The signal difference between  $I_1$ ,  $I_2$ , and  $I_3$ ,  $I_4$  were solved to get P and Q signals, which form a Lissajous circle pattern on an oscilloscope (equation 4-3). The phase can be

obtained by the arc tangent function of P/ Q signal. And the clockwise or counterclockwise Lissajous circle can be used to decide the motion direction.

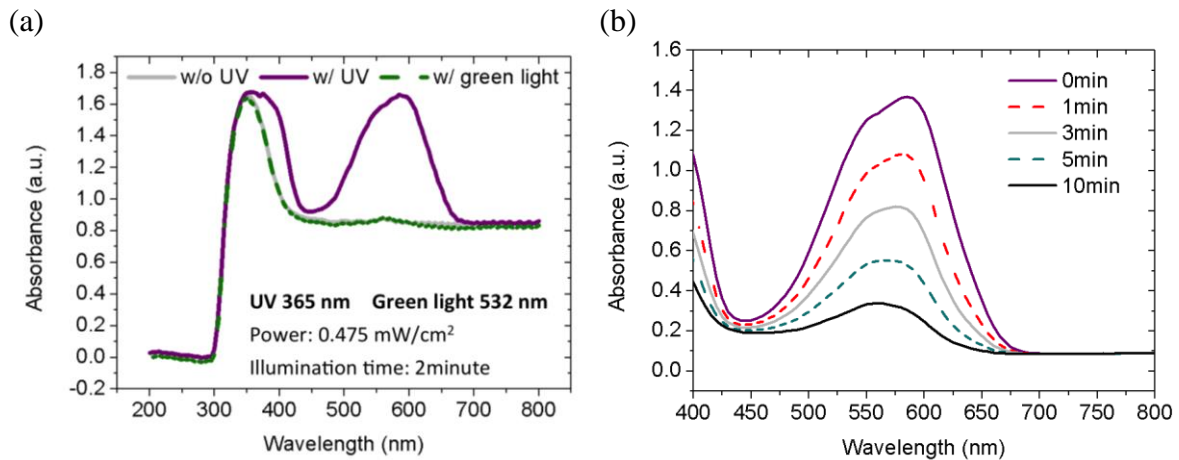


$$P \propto \cos[2\pi(f_{d1} - f_{d2})t + \Delta\phi]$$

$$Q \propto \sin[2\pi(f_{d1} - f_{d2})t + \Delta\phi] \quad (4-3)$$

### 4.1.2 Results

The optopiezoelectric actuator was studied with its optical, electrical properties, and light modulated deformation. The optical spectra of SP/LC at different states are shown in (Figure 4-4a). Before UV illumination, the SP/ LC is in SP state, which has the peak absorbance at about 330 nm (gray line). After two minutes of UV illumination (365 nm, 0.475 mW/cm<sup>2</sup>), the MC state shows another peak at about 600 nm appears (purple line). After switching off the UV light source, the molecular reverses to SP state while this 570 nm peak decays by time (Figure 4-4b). Afterwards, this peak quickly restores if the SP/LC was illuminated by an additional green light (532 nm, 0.475 mW/cm<sup>2</sup>) for two minutes (Figure 4-4c).





(c)

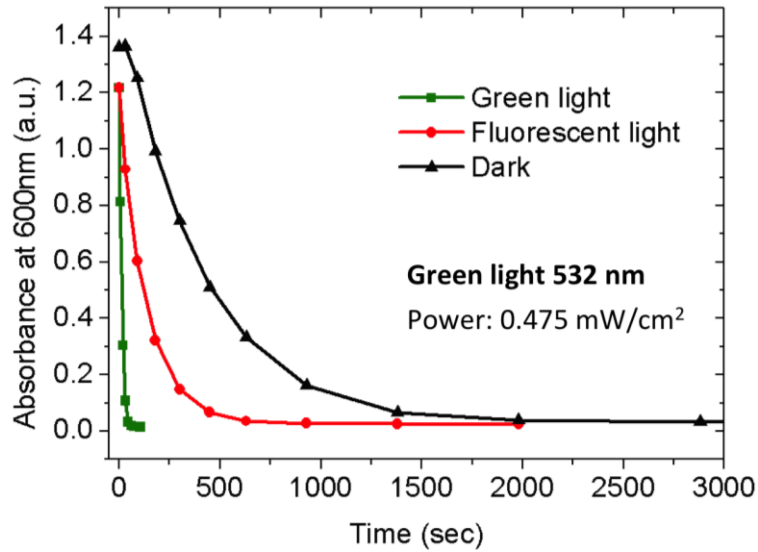
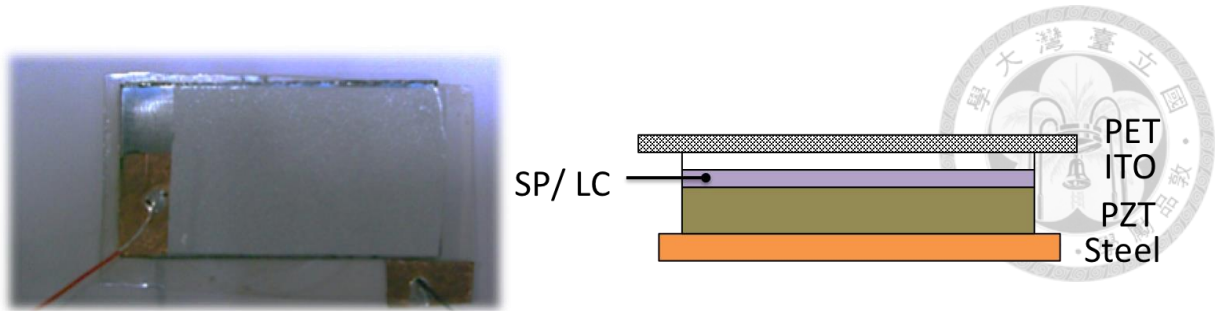


Figure 4-4. The spectra of SP/ LC with different light exposure. (a) The spectra before and after UV illumination. (b) The spectra at different time after switching off UV light source in a dark room. (c) The absorbance peak at 600 nm decays by time in a dark room, a fluorescent room, and with a green light illumination.

The double-layers actuator was fabricated by filling SP/ LC liquid into the space between the PZT and ITO PET sandwich (Figure 4-5). In previous work, the electrical impedance of SP/ LC varies in different states [71]. Because of the equivalent circuit modal, this also makes impedance ( $Z$ ) changes for the two layers optopiezoelectric actuator (SP/ LC- PZT). The variation was calculated by  $Z_{\text{after UV}}/ Z_{\text{before UV}}$  (Figure 4-6). Not only has the impedance dropped a lot after UV illumination (365 nm,  $0.7 \text{ mW/cm}^2$ ) for two minutes, the first resonant frequency also shifts from 336 Hz to 375 Hz. This resonant frequency shift might be attributed to the spiropyran chemical structure transformation from the SP state to the MC state after the UV illumination.



	Steel	PZT	SP/ LC	ITO	PET
Thickness	1.5mm	1mm	50 $\mu$ m	100nm	100 $\mu$ m
Size	4.5cm x 2cm	3.5cm x 2cm	3.5cm x 2cm		

Figure 4-5. The photo of the optopiezoelectric actuator (SP/ LC- PZT) and its structure specification.

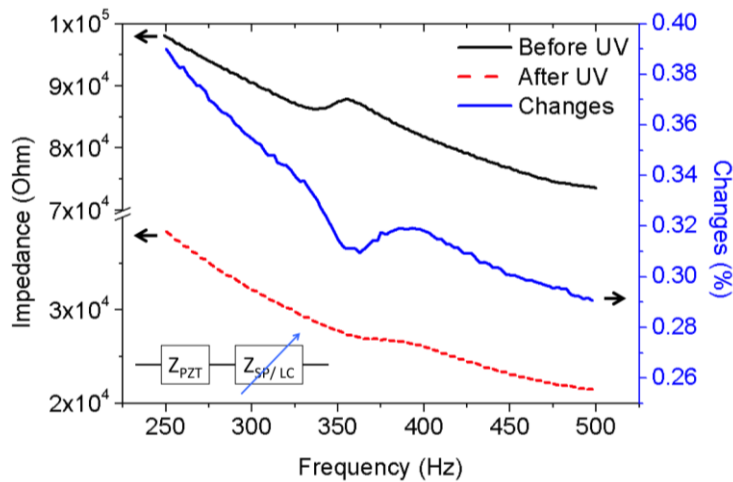


Figure 4-6. The impedance of the optopiezoelectric actuator (SP/ LC- PZT) before and after UV illumination. The insert scheme is the equivalent circuit of (SP/ LC – PZT) [71].

The actuator was fixed one end to be a cantilever beam and triggered by a 10V<sub>pp</sub> sinusoidal signal. Its peak-to-peak displacement at the free end was measured by AVID from 100 Hz to 500 Hz, with the same UV light source and duration (Figure 4-7). After

UV illumination, the frequency also shifts from 365 Hz to 400 Hz making a larger deformation when it approaches the resonant frequency.

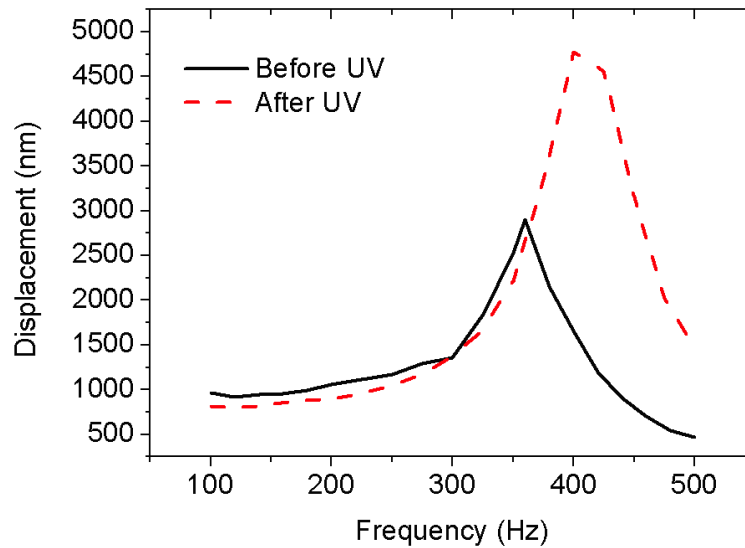


Figure 4-7. The free-end deformation of the SP/LC-PZT before and after UV illumination was measured by AVID.

### 4.1.3 Discussion

The performance of this optopiezoelectric actuator, SP/LC-PZT, can be controlled by UV light. After UV illumination, an absorbance peak in visible region is generated. The electrical impedance drops lead to the deformation increase with a resonant frequency shift. The impedance decreases because MC from is a molecular dipole that is easier to trap  $e^-/e^+$ . Thus a more intensive partial electric field across the PZT laminate, resulting a larger deformation at the illuminated area (Figure 4-8). And the frequency-shift comes from the stiffness change before and after UV irradiation [135]. The reason is the aggregated MC molecules have less effective partial molar volume than SP molecules. Thus they are

closer to each other makes a stronger inter-chain interaction, higher stiffness as well as resonant frequency.

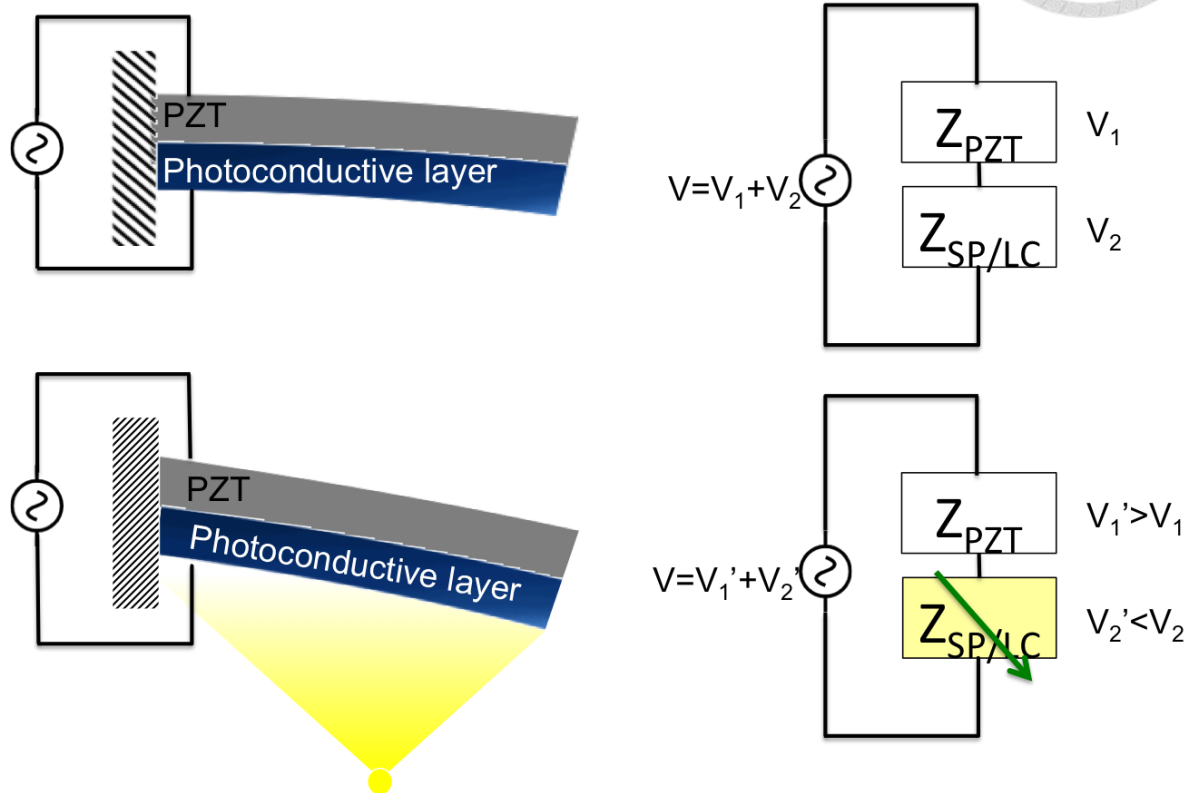


Figure 4-8. The scheme of the mechanism of a double-layers optopiezoelectric cantilever beam actuator.

The SP/ LC- PZT sensor may have good UV-modulated performance whose color, electrical and mechanical properties are reversible [135]. It can mimic spatial localized electrodes by using the illumination pattern (Figure 4-9) with DC voltage driven. But the liquid SP/ LC leakage sometimes flow out of the devices causes the amount and area of SP/ LC are difficult to control. Furthermore it is not suitable as a dynamic actuator, because the amplitude and frequency are not independent. The resonant frequency shift is

accompanied by the amplitude increment because of the spiropyran structure transformation. Thus for an appropriate optopiezoelectric actuator, the chemical structure of the photoconductive material should not be changed by the light illumination [74]. In this way, light only causes the deformation enhancement without varying the resonant frequency.

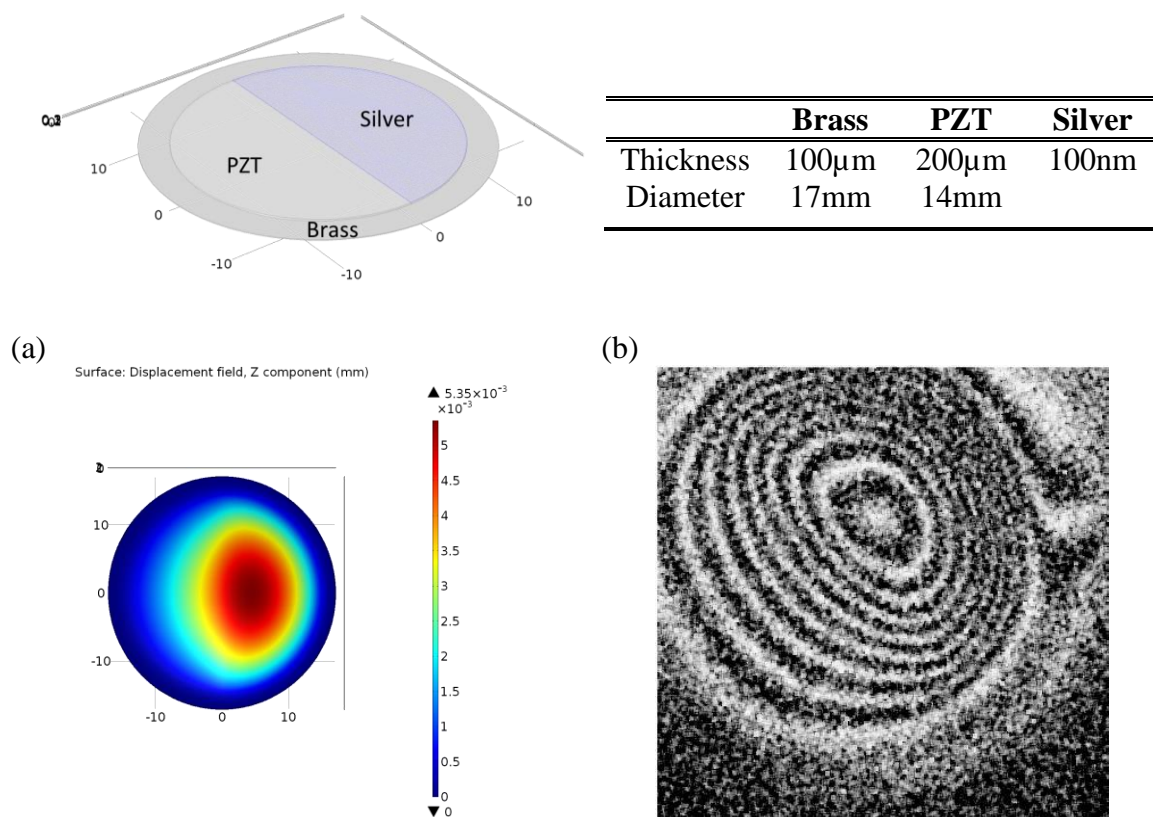
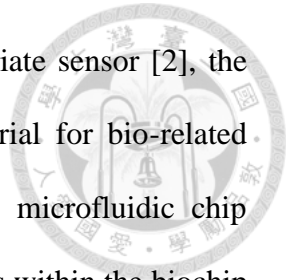


Figure 4-9. The deformation of a PZT buzzer with only right half electrode triggered with 20 DC voltage. (a) COMSOL simulation; (b) Electrical speckle pattern interferometry (ESPI) measurement.

## 4.2 Optopiezoelectric sensor

The localized sensing ability of an optopiezoelectric sensor could be modulated by



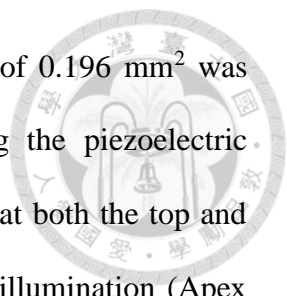
using the light illumination. Although the SP/ LC-PZT is an appropriate sensor [2], the short lifetime (few weeks) and the UV light source limits this material for bio-related studies. Also it is difficult to integrate PZT with a biocompatible microfluidic chip substrate. Furthermore, UV light will damage the biomolecules or cells within the biochip. Therefore, we set out to find an optical controlling piezoelectric material that can be extended to biological applications. Considering the application requirement, an one layer structure P(VDF-TrFE)/ TiOPc, which is a flexible, light, and easy to fabricate thin film. In this section, the physical characteristics of this composite were examined.

#### **4.2.1 Material and film preparation**

The powder copolymer P(VDF-TrFE) (70/ 30) was purchased from PiezoTech and the dimethylformamide (DMF) from Acros Organics Co. Titanyl phthalocyanine (TiOPc,  $C_{32}H_{16}N_8OTi$ ) powder was obtained from Sigmae Aldrich Co.

The P(VDF-TrFE) powder was dissolved in a DMF solvent at a concentration of 10 wt%. The solution underwent vigorous stirring at 70 °C for more than 24 hours then the TiOPc powder was added to the solution. The resulting mixture underwent an ultrasonic dispersion process. The composite P(VDF-TrFE)/ TiOPc was coated uniformly onto the ITO glass and the solvent volatilized at 60 °C on a hotplate for 1.5 hour to form the 40 μm thin film.

The film was then annealed twice at 135 °C for two hours and at 70 °C for an hour in a vacuum oven to increase its crystallinity before cooled to room temperature. The film was polarized by corona charging with a distance of 2.5 cm for two hours at 90 °C before slowly cooled to room temperature.



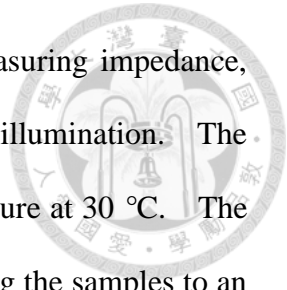
To measure the hysteresis loop (P-E loop), an Au top electrode of 0.196 mm<sup>2</sup> was deposited onto the film using a sputtering process. For measuring the piezoelectric constant ( $d_{33}$ ), the demolded film was deposited onto the Au electrode at both the top and bottom. For measuring the optoelectrical response under white light illumination (Apex Fiber Illuminator 70 531, 200 W Hg, Newport), an Au top electrode of 1 cm<sup>2</sup> size was deposited onto the film. All measurements were performed at room temperature.

#### 4.2.2 Characterization methods

The surface morphology of the P(VDF-TrFE) and P(VDFTrFE)/ TiOPc film was recorded using a scanning electron microscope (SEM) (S-4800, Hitachi). The chemical bonds of the P(VDFTrFE)/ TiOPc composite material were confirmed by Fourier transformed infrared spectroscopy (FTIR) (Nexus 470, Thermo Nicolet) with a DTGS detector. The FTIR transmission was collected using 32 scans at a resolution of 2 cm<sup>-1</sup>. The crystalline phases were analyzed using a  $\theta/\theta$  X-ray diffractometer (XRD) (X'Pert PRO Diffractometer, Panalytical) from 10 ° to 50 °.

The hysteresis loops (P-E loops) were measured using a ferroelectric analyzer (aixACCT, TF2000). The maximum electric field was triggered at 115 MV/m, 1 mA current and 100 Hz frequency. The piezoelectric constant ( $d_{33}$ ) of the film was obtained from the  $d_{33}$  piezoelectric meter (KCF Technologies) with 0.25 N at 110 Hz. The  $d_{33}$  value was calculated as  $[+d_{33}-(-d_{33})]/2$ , where  $+d_{33}$  and  $-d_{33}$  were the parallel and opposite parallel measurements to the poling direction.

The absorbance spectra of the P(VDF-TrFE) and P(VDFTrFE)/ TiOPc film was taken using an UV-Vis spectroscope (Lambda 900 spectrometer, PerkinElmer) from 300 nm to



900 nm wavelength. The optoelectrical response was studied by measuring impedance, capacitance and resistance values before and after 5 minutes white light illumination. The light power on the sample was about 112 klux with a localized temperature at 30 °C. The impedance was measured from frequency 40 Hz to 10 kHz by connecting the samples to an impedance analyzer (4294A, Agilent). The capacitance and resistance values were measured independently using a RLC meter (RCL Meter PM6303, Phillips) at 1 kHz.

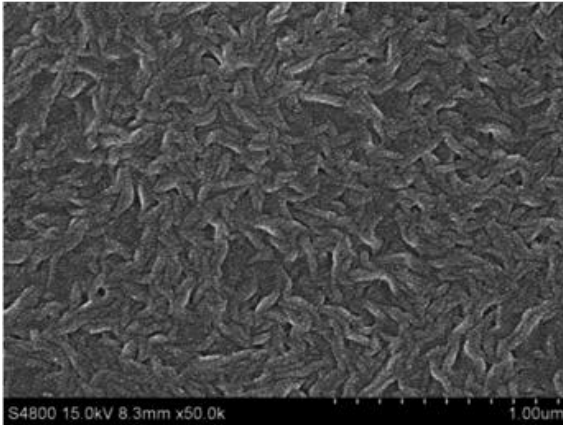
### **4.2.3 Physical properties**

The composite thin film P(VDF-TrFE)/ TiOPc contained 0 wt%, 0.5 wt%, 2.5 wt%, 5 wt%, 10 wt% and 20 wt% TiOPc particles in the P(VDF-TrFE) solution were designated as Samples 1 to 6, respectively. The surface morphologies of sample 1~4 and TiOPc powders were analyzed by SEM images (Figure 4-10). The P(VDF-TrFE) copolymer grew along the TiOPc particles when the solvent DMF evaporated. From a morphology point of view, it was expected that the piezoelectric properties of the P(VDF-TrFE)-based composite thin film would be strongly governed by the TiOPc content. These particles without piezoelectric properties result in a weaker piezoelectric effect of the P(VDF-TrFE) film.

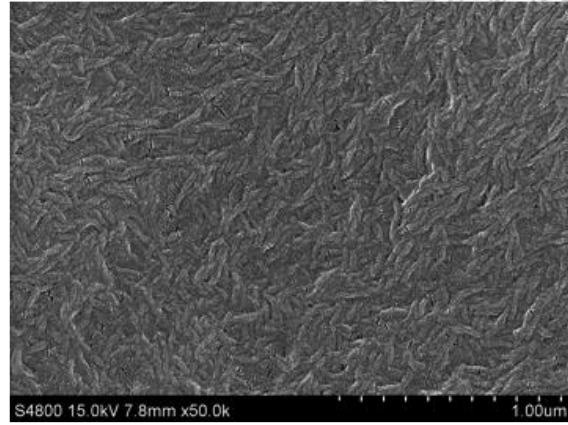




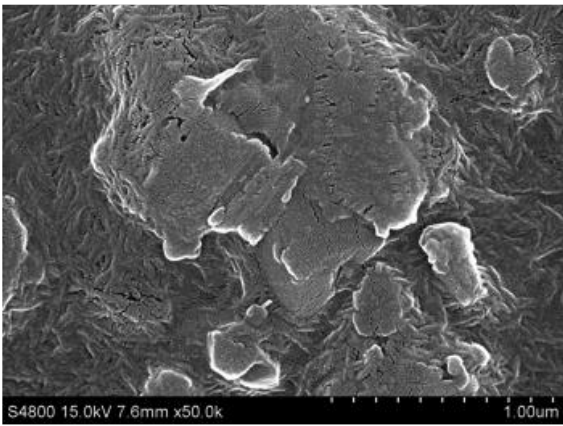
(a)



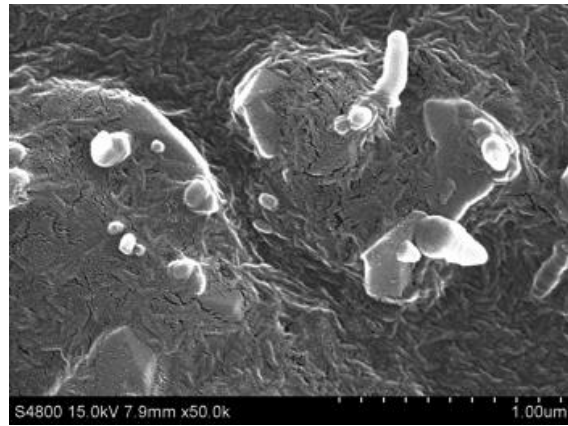
(b)



(c)



(d)



(e)

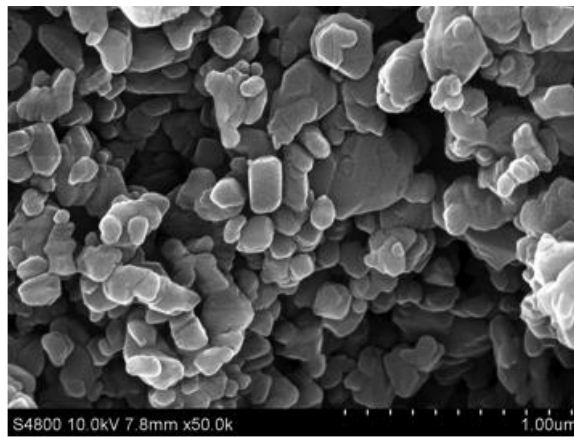
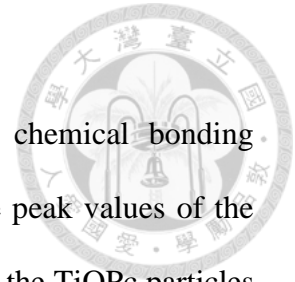


Figure 4-10. SEM images of (a) P(VDF-TrFE) and (b)-(d) P(VDF-TrFE)/ 0.5 wt%, 2.5 wt%, 5 wt% TiOPc powder surface morphology. (e) TiOPc powder.



A FTIR transmission spectrum was used to demonstrate the chemical bonding between the TiOPc and P(VDF-TrFE) copolymer (Figure 4-11). The peak values of the P(VDF-TrFE) and TiOPc are listed in (Table 4-1). Spectra shows that the TiOPc particles were simply blended into the P(VDF-TrFE) copolymer without chemical bonding. It was evident that the amount of TiOPc increased, the TiOPc and P(VDF-TrFE) peak intensities also increased and decreased, respectively [136~ 139].

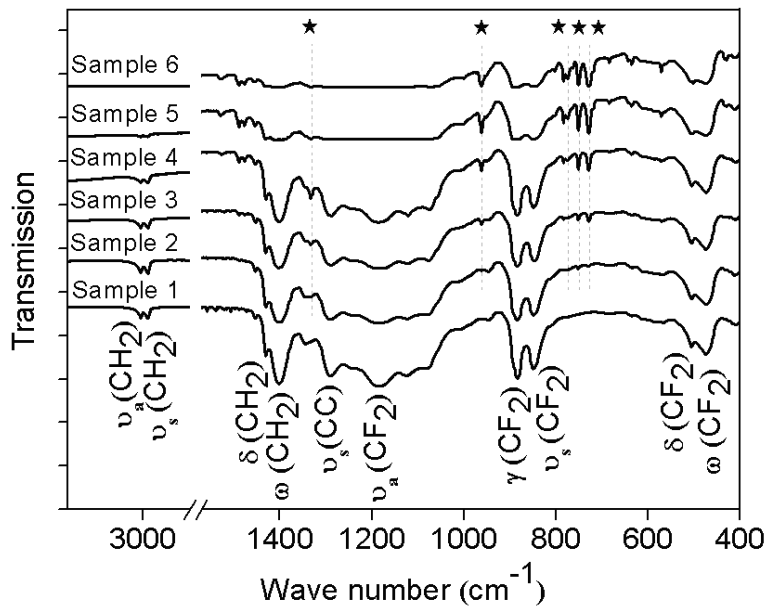


Figure 4-11. FTIR transmission spectra of P(VDF-TrFE) and P(VDF-TrFE)/ TiOPc composite film. The symbol “★” marks the peaks of the TiOPc particles. (Note:  $\nu_s$  and  $\nu_a$  represent symmetric and anti-symmetric stretching modes;  $\omega$ ,  $\delta$ , and  $\gamma$  represent wagging, bending and rocking modes).



Table 4-1. Infrared active modes of P(VDF-TrFE) and TiOPc.

<b>P(VDF-TrFE) Peak Values (cm<sup>-1</sup>)</b>	<b>Attribution</b>	<b>TiOPc Peak Values (cm<sup>-1</sup>)</b>	<b>Attribution</b>
3011	$\nu_a(\text{CH}_2)$	1333	Pyrrole stretch
2974	$\nu_s(\text{CH}_2)$	961	Ti=O
1430	$\delta(\text{CH}_2)$	777	$\nu(\text{CN})$
1402	$\omega(\text{CH}_2)$	752	$\delta(\text{C}_6\text{-H}_6)$
1289	$\nu_s(\text{CC})$	729	$\gamma(\text{CH})$
1184	$\nu_a(\text{CF}_2)$		
884	$\gamma(\text{CF}_2)$		
849	$\nu_s(\text{CF}_2)$		
506	$\delta(\text{CF}_2)$		
472	$\omega(\text{CF}_2)$		

The piezoelectric properties of P(VDF-TrFE) were closely related to its crystallinity and phase distribution. A  $\beta$ -phase P(VDF-TrFE) is known for its high piezoelectric efficiency. It was evident from the XRD pattern that the crystallization of the  $\beta$ -phase can be greatly improved with annealing (Figure 4-12a). After annealing, the  $\beta$ -phase peak at  $2\theta = 20.4^\circ$  moved slightly to  $19.7^\circ$  with increased intensity and the amorphous region disappeared. As for the composite films, the  $\beta$ -phase peak of P(VDF-TrFE) was still the dominant peak (Figure 4-12b). The peaks at  $13.2^\circ$ ,  $26.2^\circ$  and  $27.1^\circ$  were from the TiOPc particles. These particles has negligible effect of P(VDF-TrFE) crystallization. This is understandable since TiOPc particles, which are about the size of a few hundred nanometers, are too large to interfere with the microstructure of the crystalline P(VDF-TrFE) lamella (possessing only a few angstroms spacing) during annealing.

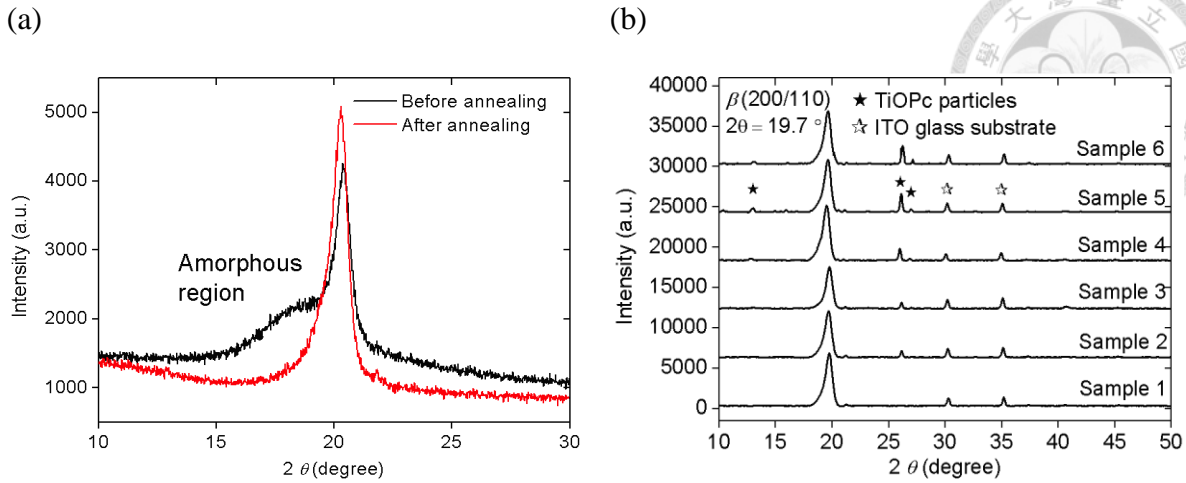


Figure 4-12. XRD patterns of (a) P(VDF-TrFE) film before and after annealing. (b) P(VDF-TrFE) and P(VDF-TrFE)/ TiOPc composite film.

Polarization hysteresis of P(VDF-TrFE)/ TiOPc provides direct information on how much polarization can be induced and retained by the material during electrical poling. The measured hysteresis loops show that the surface charge ( $P$ ) and coercive field ( $E_c$ ) are highly dependent on the TiOPc content (Figure 4-13). Both  $P$  and  $E_c$  increased with increased TiOPc concentration. The movement of the P(VDF-TrFE) molecules and their crystalline lamellae were inhibited by the presence of the TiOPc particles. This phenomenon means that a larger electrical field is required to re-orientate (i.e. switch) the crystalline dipole structure, which can increase  $E_c$  with increased TiOPc content. Moreover, the simultaneous increase in surface charges is due to the semi-conducting characteristics of the TiOPc after charged with an electrical field. The polarization hysteresis loops also indicate there is current leakage at high electric fields for samples with high TiOPc content. In our study, the composite films with TiOPc percentages higher than 30 wt% showed electrical breakdown before reaching the maximum (e.g. saturation)

electric field. It was expected that the optimal TiOPc percentage would be less than 10 wt% to ensure a stable poling behavior and efficient piezoelectric characteristics.

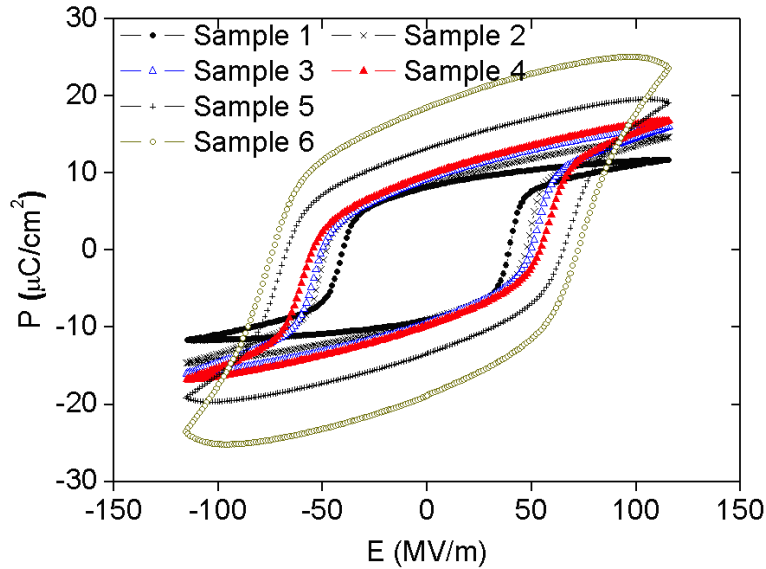
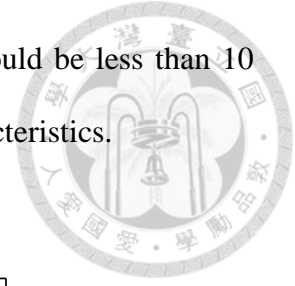


Figure 4-13. Hysteresis loops of P(VDF-TrFE) and P(VDF-TrFE)/ TiOPc composite film.

The piezoelectric coefficient,  $d_{33}$  (C/N), represents the mechanical and electrical transferring ability of a “piezoelectric material” under its maximal poling voltage. In the “composite P(VDF-TrFE)/ TiOPc films”, these non-piezoelectric TiOPc powders inhibit P(VDF-TrFE) achieving its highest  $d_{33}$  value. It means, the maximal poling voltage ( $PV_M$ ) for the composites must be smaller than for pure P(VDF-TrFE) film [111]. And the mechanical/ electrical transferability of the composite should be redefined as quasi- $d_{33}$ ,  $d_{33}^{(q)}$  (Table 4-2). These constants are smaller than  $d_{33}$  values in the pure P(VDF-TrFE) film. And this constant decreased with the TiOPc increment. This phenomenon also confirms the SEM images which show that too much TiOPc in the composite can possibly destroy

the crystallization of the P(VDF-TrFE). Thus, it can be expected that a high piezoelectric efficiency can be obtained when the TiOPc percentage is less than 10 wt%.

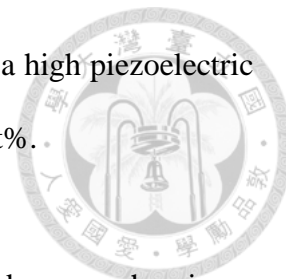
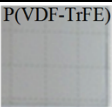
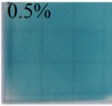
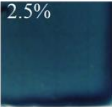
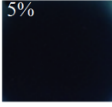
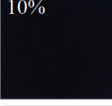
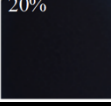


Table 4-2. Relationship between piezoelectric efficiency  $d_{33}$  values and corona charging voltage of P(VDF-TrFE) and P(VDF-TrFE)/ TiOPc composite film.

Sample	Photo	$PV_M$ (kV)	$d_{33}^{(9)}$ (pC/N)
1		17.5	31.7
2		17.5	26.0
3		17.5	21.4
4		16.0	20.4
5		15.0	18.6
6		15.0	9.2

A visible light spectra can provide the absorbance band of the composite P(VDF-TrFE)/ TiOPc films (Figure 4-14). Pure P(VDF-TrFE) films have a weak ability to absorb visible light. For the composite P(VDF-TrFE)/ TiOPc, the absorbance ability in the range between visible light and infrared. We found that the absorbance intensity of Samples 4, 5, 6 were similar which confirms that the absorbance reached saturation when the TiOPc content was higher than 5 wt%. Based on the spectra results, we can conclude that our composite material possesses a high and broad sensitivity to visible light.

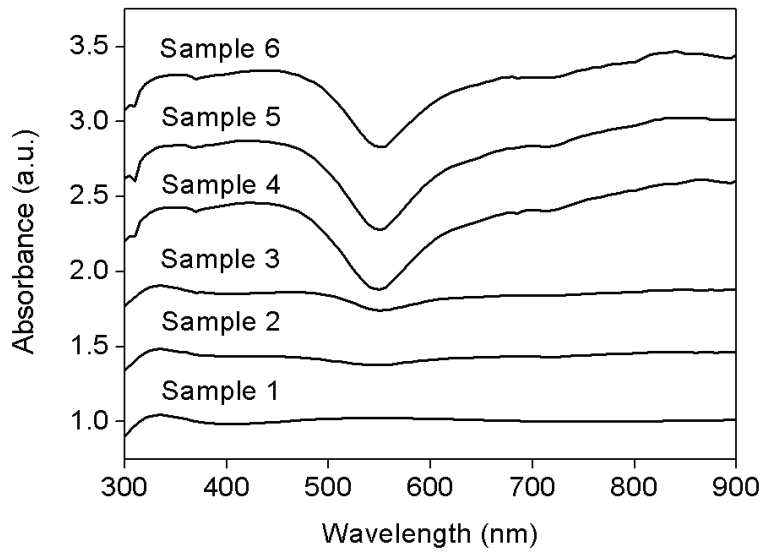


Figure 4-14. UV-Vis spectra of P(VDF-TrFE) and P(VDF-TrFE)/ TiOPc composite film.

For piezoelectric materials, the electrical displacement (**D**) and strain (**S**) tensor have a direct relationship, e.g.  $\mathbf{D} = \mathbf{eS}$ . The piezoelectric stress/ charge tensor,  $\mathbf{e}$ , which is closely related to the crystalline structure, is a constant. For an optopiezoelectric sensor film, the strain on the specimen can be calculated from the electrical displacement (**D**), which changes due to the light illumination pattern. We found that the material impedance values are closely related to TiOPc content. (Figure 4-15a) shows the impedance variation of the P(VDF-TrFE)/ TiOPc composite films. The variation,  $(Z-Z_0)/Z_0$ , decreased more for films with higher TiOPc content since more excited  $e^-/e^+$  pairs traveling inside (Figure 4-15b). Furthermore, the variation was more obvious at low frequencies but tended to be constant after 5 kHz. Our experimental results confirm that the composite P(VDF-TrFE)/TiOPc material works well at low frequencies.

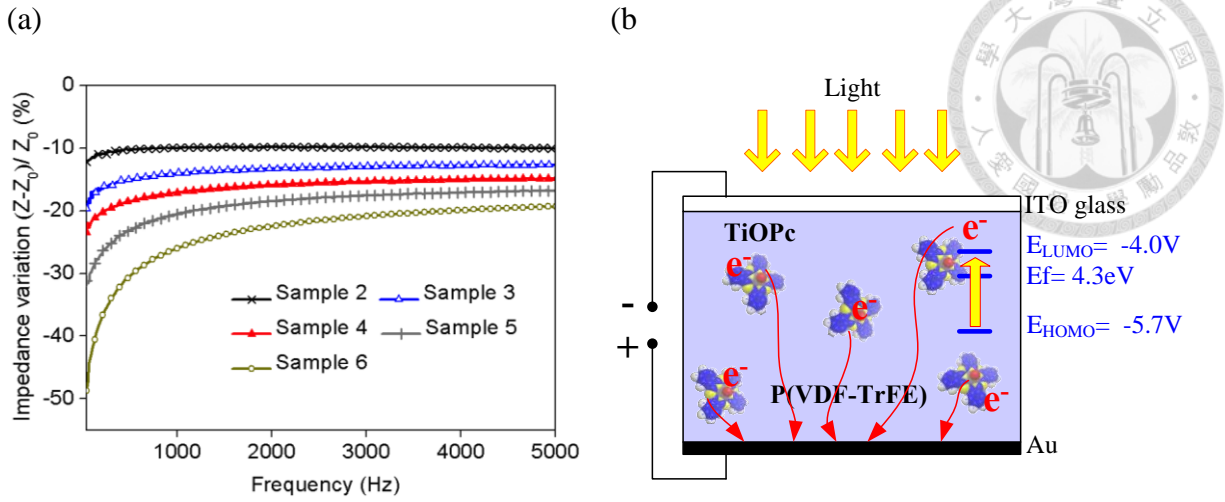
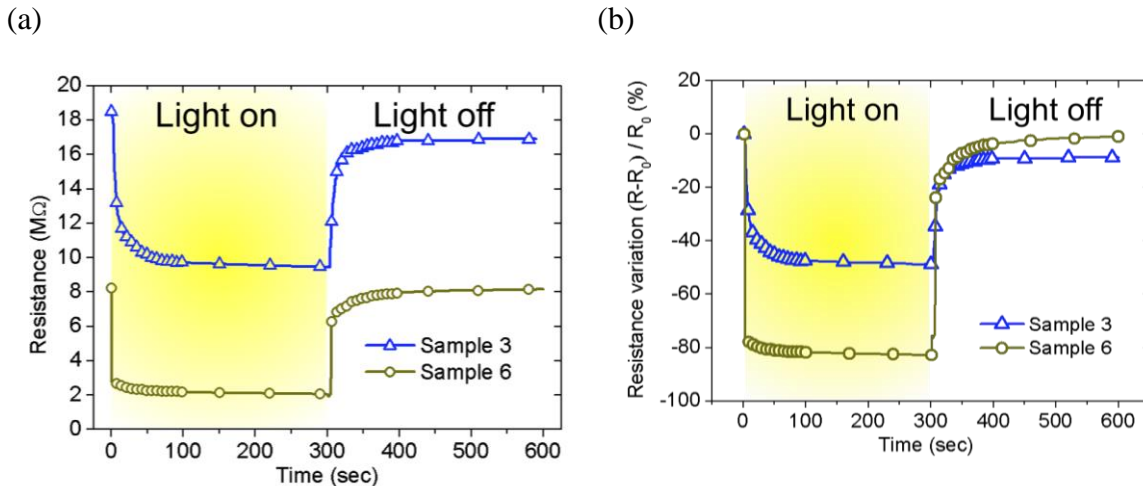


Figure 4-15. (a) Impedance variation of P(VDF-TrFE)/ TiOPc composite film. (b) Schematic of the stimulated electrons cause the impedance variation.

The capacitance and resistance changes are shown in (Figure 4-16). The capacitance increment was clearly smaller than the decreased resistance after light illumination. At a 20 wt% of the composite film, the capacitance variation increased 25 % while the resistance dropped 80 %. This result confirms that the impedance variation decreases at higher frequencies when a capacity effect dominates the equivalent circuit.





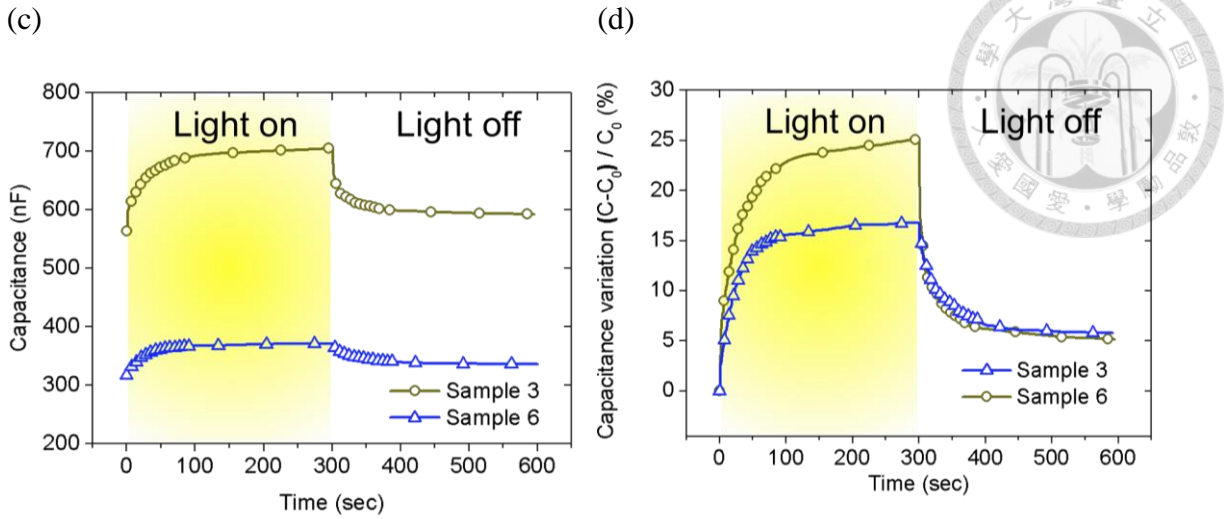


Figure 4-16. The (a) resistance and (c) capacitance values of Sample 3 and Sample 6, as well as (b, d) their variation before and after illumination.

A further optoelectrical effect with 450 nm and 750 nm light illumination was discussed because their absorbance are similar. The same white light mercury lamp (Apex Fiber Illuminator 70531, 200W Hg, Newport) was filtered to 450 nm and 750 nm. The impedance changes of a P(VDF-TrFE)/ 10% TiOPc film was measured before and after five minutes at  $0.025 \text{ W/cm}^2$  intensity light illumination (Figure 4-17). The electrical response at 450 nm wavelength illumination was larger than that at 750 nm wavelength illumination. For example at 100 Hz, the impedance variation as follows: -15.58 % at 450 nm and -12.58 % at 750 nm light illumination. It might because the  $e^-/e^+$  pairs have more kinetic energy after they absorb 450 nm wavelength. Thus the impedance decrement is more obvious with 450 nm than 750 nm light illumination.

Based on the optoelectrical response, the equivalent circuit of our composite was established to be a resistor parallel to a capacitor (Figure 4-18a). Both the resistor and capacitor were light adjustable. The impedance variation at 750 nm was simulated based

on the experimental results shown in (Figure 4-18b).

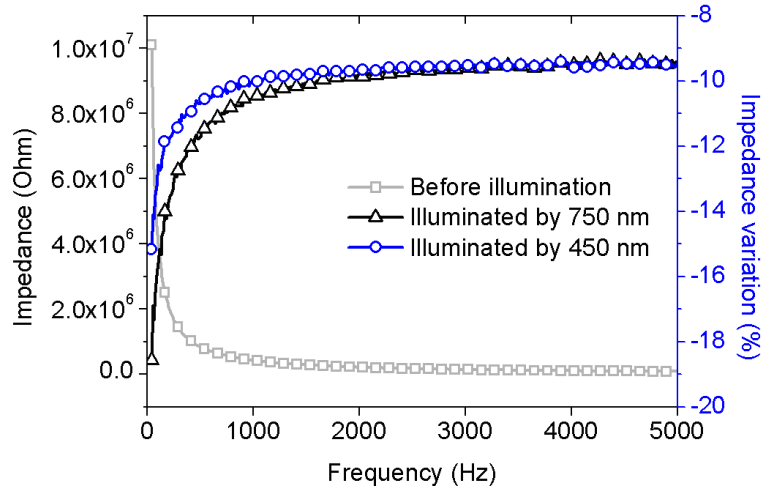
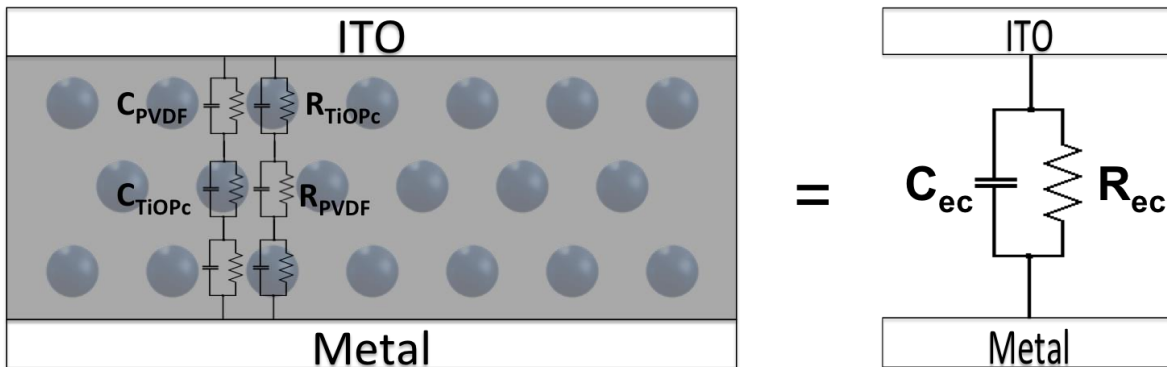


Figure 4-17. Impedance of P(VDF-TrFE)/ 10% TiOPc at 750nm and 450nm.

(a)



(b)

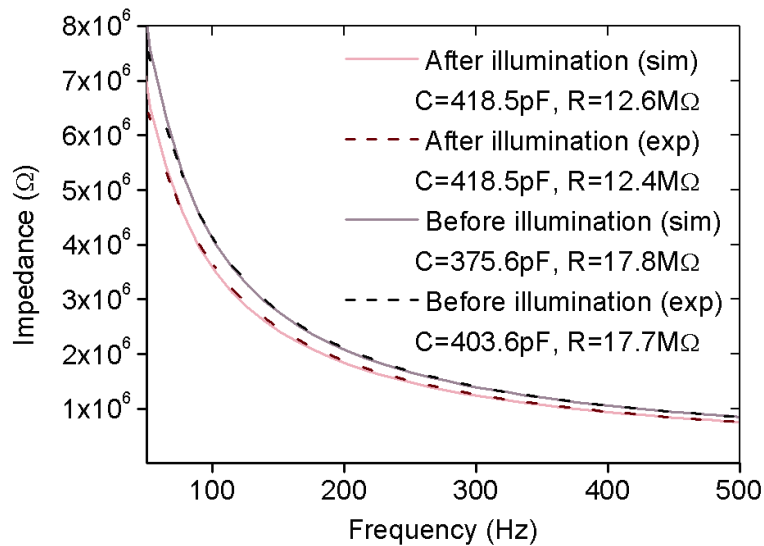
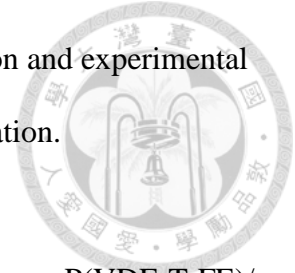


Figure 4-18. (a) The equivalent circuit of the composite. (b) Simulation and experimental results of the impedance before and after 750nm illumination.



Above all, the optical response of this optopiezoelectric sensor, P(VDF-TrFE)/TiOPc, was coated to form a thin film using solution processing and which makes it possible to integrate with MEMS processing. The characteristics of P(VDF-TrFE)/TiOPc composite appears that it is a good potential material for dynamic light-spatial controlling applications.

#### **4.2.4 Sensing performance**

The performance of the optopiezoelectric sensor can be examined in a cantilever beam system (Figure 4-19). A resonant frequency was obtained using a dynamic signal analyzer (SR780, Stanford Research Systems). The resonant frequencies of the beam were the same before and after white light illumination in (Figure 4-20). A 12 cm x 2 cm x 0.15 cm spring steel cantilever beam was clamped onto the shaker (small vibration exciter type 4808, Brüel & Kjær) which was triggered at 2 V<sub>rms</sub>, 538 Hz by connecting to a function generator (3314A, Hewlett Packard) with a power amplifier (HSA4052, NF Corporation). The sensed charges from the composite film were measured using a charge amplifier (Kistler Type 5011B, Intertechnology) with an oscilloscope (TDS3034B, Tektronix). The 2.5 cm x 2 cm x 60 μm P(VDF-TrFE)/10% TiOPc composite film was then illuminated by a projector.

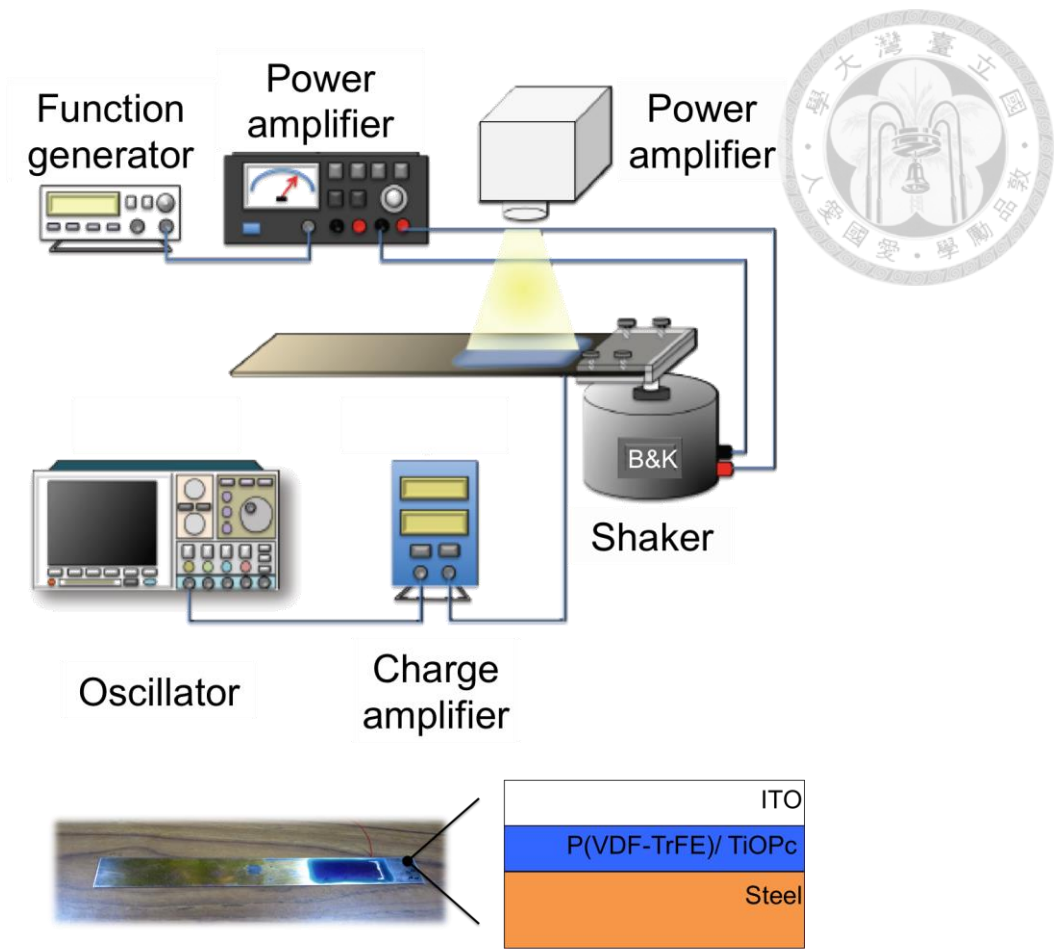


Figure 4-19. Experimental set-up of photosensitive piezoelectric system.

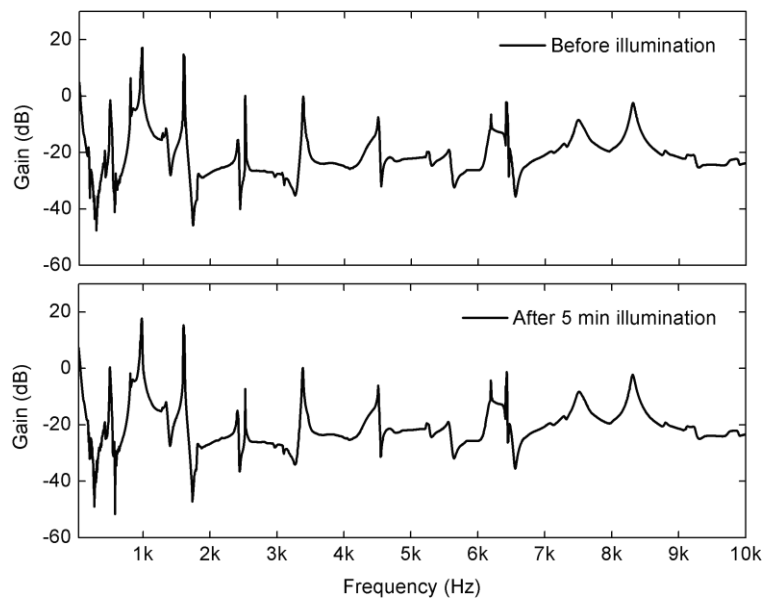
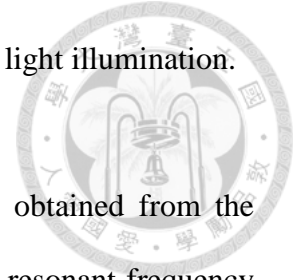
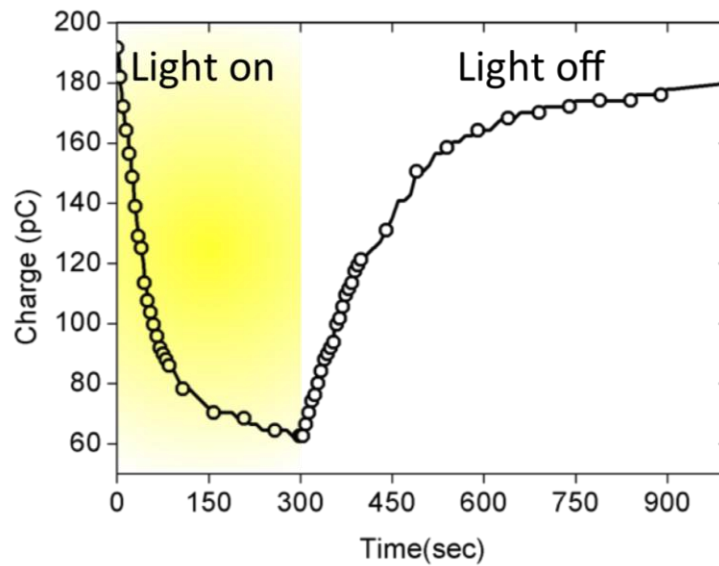


Figure 4-20. Frequency spectra of the cantilever beam before and after light illumination.



In (Figure 4-21a), before light illumination, the charges were obtained from the piezoelectric effect when the cantilever beam was triggered at the first resonant frequency (538 Hz). With light illumination, the  $e^-/e^+$  pairs were excited in TiOPc. And they would travel in the composite with an opposite direction to the internal electric field, canceling the charges generated from piezoelectric effect (Figure 4-21b). Our experimental results confirm that our composite has good response as a photosensitive piezoelectric sensor in mechanical systems.

(a)



(b)

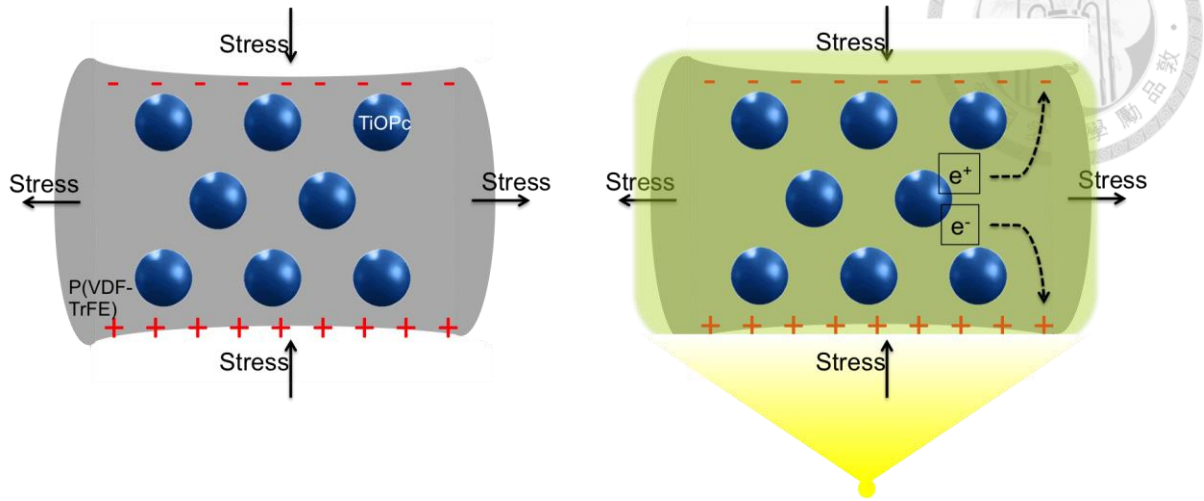
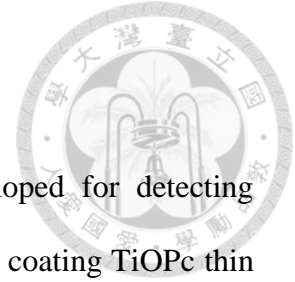


Figure 4-21. (a) Obtained charges from the photosensitive composite piezoelectric sensor with white light illumination. (b) Scheme of charge cancellation after light illumination.

#### 4.2.5 Discussion

In the experimental results, the single layer optopiezoelectric composite can be an efficient sensor with obvious response in a short time. This composite provides a potential application for spatial light modulated controlling in a dynamic vibration system. But the charge becomes smaller after illumination, meaning it's hard to be an optopiezoelectric sensor with instinctive control. Furthermore, the experimental results show the piezoelectric effect was destroyed by the TiOPc particles. Thus the mechanical and electrical transferring effect became weaker, and the sensibility is smaller than pure P(VDF-TrFE). For increasing the sensibility of the optopiezoelectric sensors, in chapter 5, a modified double-layers structure PZT-TiOPc/resin, is more practical to be an optopiezoelectric sensor for bending measurement.

## Chapter 5. Optopiezoelectric bending sensor



In this chapter, a modified optopiezoelectric sensor was developed for detecting bending signals in dynamic vibrating systems. It is fabricated by spin coating TiOPc thin film onto PZT plate, which has a larger piezoelectric stress constant. Comparing to the composite film, P(VDF-TrFE)/ TiOPc, the bending slope (or bending angle) are easier to obtain from illumination patterns of the double-layers sensor, PZT-TiOPc. The mechanism, optical and optoelectrical properties of this double-layers optopiezoelectric sensor is analyzed. Furthermore, the sensing performance of this sensor are designed and experimentally verified by using a dynamic one-dimensional cantilever plate system. The experimental results matched well with the numerical simulation results.

### 5.1 Device fabrication and experimental setup

A double-layers optopiezoelectric sensor was made of PZT lamina and TiOPc thin film (Figure 5-1a). The PZT (QA type)-brass beam was custom-made by Eleceram Technology Co., Ltd. The silver top electrode was etched in a mixture solution (methanol: hydrogen peroxide: ammonium hydroxide =4: 1: 1) for 3~5 minutes.

The  $\gamma$ -TiOPc power was distributed in 1-Butanol solvent in weight ratio 1: 6 and then stirred for more than 48 hours. This solution was then stirred and mixed into the resin (copolyamide, Platamid® M 1276) in 40% w.t. ( $\frac{m_{TiOPc}}{m_{resin} + m_{TiOPc}}\%$ ) on a 75°C hotplate for another 48 hours. The gel-like TiOPc/ resin was spun coated on the PZT laminate and baked at 70°C for half an hour to form a film of 30 $\mu$ m thick or so. Finally

the ITO top electrode was sputtered with RF Sputter System in Tze-Chiang Foundation of Science and Technology (TCSFST).

In a double-layers sensor, the mechanically induced piezoelectric charge signal increases after TiOPc was illuminated by light due to its impedance drop (Figure 5-1b). For a vibrational system (Figure 5-2), the PZT lamina generates charges on its surface. The TiOPc layer serves as a voltage divider, which reduces the charges propagating through the ITO electrode. Once illuminated by light in a pre-specified pattern locally, the impedance under of the bright area (light illuminated area) drops that in turn enhances the charges obtain from the bright area. This spatial tailoring mechanism can thus be used to create various different distributed sensor in-situ real time by changing the illumination patterns. For example, illuminated the overall area leads to bending angle measurement at the tip of a cantilever beam. Illuminated TiOPc in triangular pattern provides us with an opportunity to measure the tip displacement at the tip of the triangular pattern. All of which will be explored in detail herein.

In our measurement, the beam was set up in a one-dimensional cantilever plate configuration [140], i.e., fixed-free boundary conditions, and tested by mounting the overall structure onto a vibration shaker (Measurement Exciter Type 4810, Brüel & Kjær). The vibration signal was supplied by using a power amplifier (4005 High Speed Power Amplifier, NF electronic instruments) to amplify the signal generated from a function generator (3314A, Hewlett-Packard). The acceleration was measured by an accelerometer (Brüel & Kjaer, Type 4381). The vibrating forces were set to be 0.04, 0.09, 0.13, 0.18, 0.22 mN. A series of different light patterns were illuminated by using a LCD projector to send the corresponding light images from a connected computer. The light intensity at the



beam was 30 klux and the temperature was kept at room temperature. In addition, the illumination time was set to be less than 5 seconds in order not to raise the temperature around the one-dimensional cantilever plate under testing. The piezoelectric induced charges were amplified and transferred to output voltage by the charge amplifier (Type 5011B, Kistler).

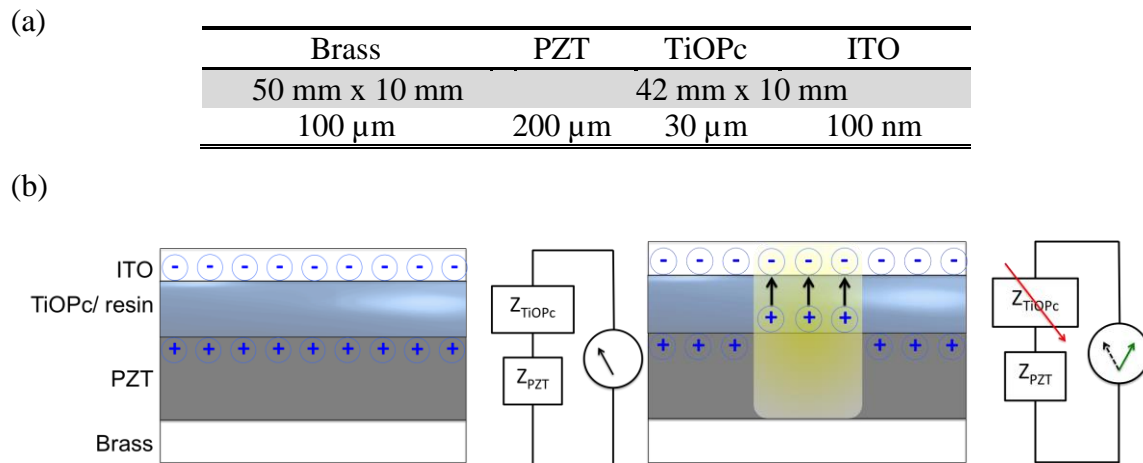


Figure 5-1. (a) The structure and (b) mechanism of PZT-TiOPc double layers optopiezoelectric sensor.

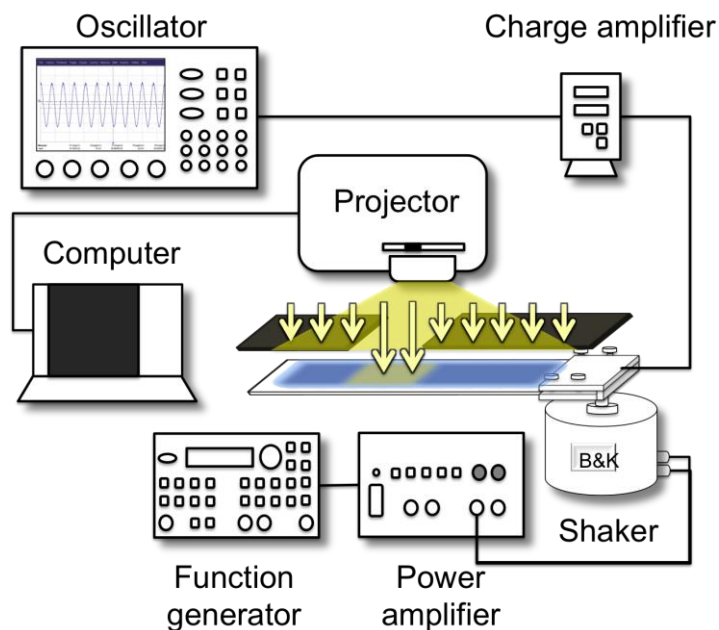


Figure 5-2. The experimental setup of an optopiezoelectric sensor for measuring bending angle.



## 5.2 Experimental results

Our experimental results demonstrate that the charges with different illumination areas are correlated to the theoretically predicted bending slope. Furthermore, we calculated the charges by using an empirical formula to verify the newly proposed PZT-TiOPc sensor to be a convenient and efficient optopiezoelectric sensor for dynamic system applications.

### 5.2.1 Material characteristics

The optical and optoelectrical properties of the TiOPc thin film were discussed in detail in some previous works [73, 74]. The electric equivalent circuit of TiOPc can be represented as a parallel resistor and capacitor (Table 5-1). The impedance of an approximate 30  $\mu\text{m}$  thick film can be calculated by (equation 5-1), and the impedance-frequency curves with frequency range between 20 to 1000 Hz is shown in (Figure 5-3).

Table 5-1. The resistor and capacitor changes of a 40% TiOPc in resin of different thicknesses [73].

Thickness ( $\mu\text{m}$ )	No light		Light illumination	
	$R_d$ ( $\text{M}\Omega$ )	$C_d$ (pF)	$R$ ( $\text{M}\Omega$ )	$C$ (pF)
31.6	305.5	24.8	147.8	27.6
14.1	58.0	37.2	12.8	73.3
9.2	50.2	43.7	9.5	86.9



$$Z(j\omega) = \frac{1}{j\omega C + \frac{1}{R}} = \frac{R^2}{1 + \omega^2 R^2 C^2} \left( \frac{1}{R} - j\omega C \right)$$

$$|Z(j\omega)| = \frac{R}{\sqrt{1 + \omega^2 R^2 C^2}}$$

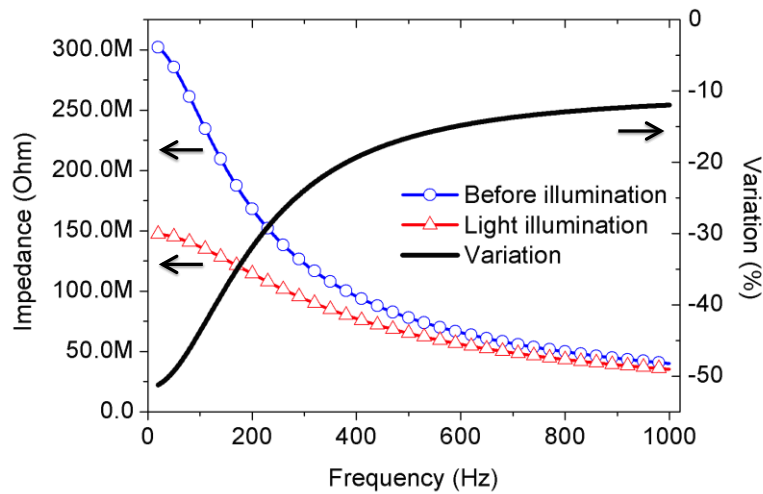


Figure 5-3. The calculated impedance of a 40% TiOPc film from equation 5-1 with parameters in Table 5-1.

### 5.2.2 Bending sensor

The one-dimensional cantilever plate was driven into resonance at its resonant frequency of 28.3 Hz. The tip vibrating displacement was measured and shown in (Figure 5-4).

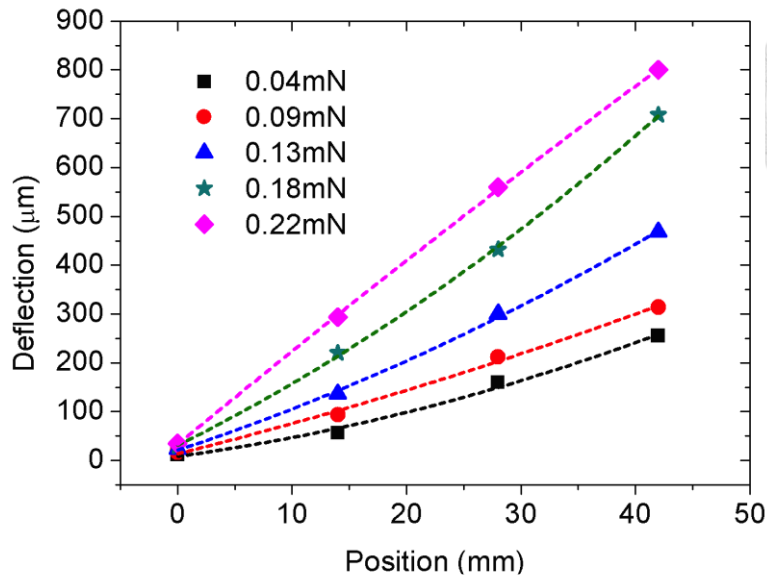


Figure 5-4. The free end deflection of the one-dimensional cantilever plate under different driving forces.

To examine the sensing performance of the PZT-TiOPc laminate, the spatial light patterns were illuminated onto the beam (Figure 5-5a~c). When the static beam was illuminated by white light, the TiOPc excitons were detected and the amount only depends on the brightly illuminated area and the light intensity. (Figure 5-5d) demonstrates a static beam which was illuminated at 0~14 mm; 0~28 mm and 0~42 mm with illuminating frequency of 2 Hz. After a long-term repeating cycles, the wave clearly shifts a little downward because of the TiOPc fatigue. For a vibrating beam, during illumination, the peak-to-peak charge increases with an offset. The peak-to-peak charge enhancement is because of the TiOPc impedance drops, making more piezoelectric charges arrive the ITO electrode. The offset comes from the TiOPc excitons (Figure 5-5e). The detail peak-to-peak charges are measured with different trigger force and patterns (Figure 5-6).

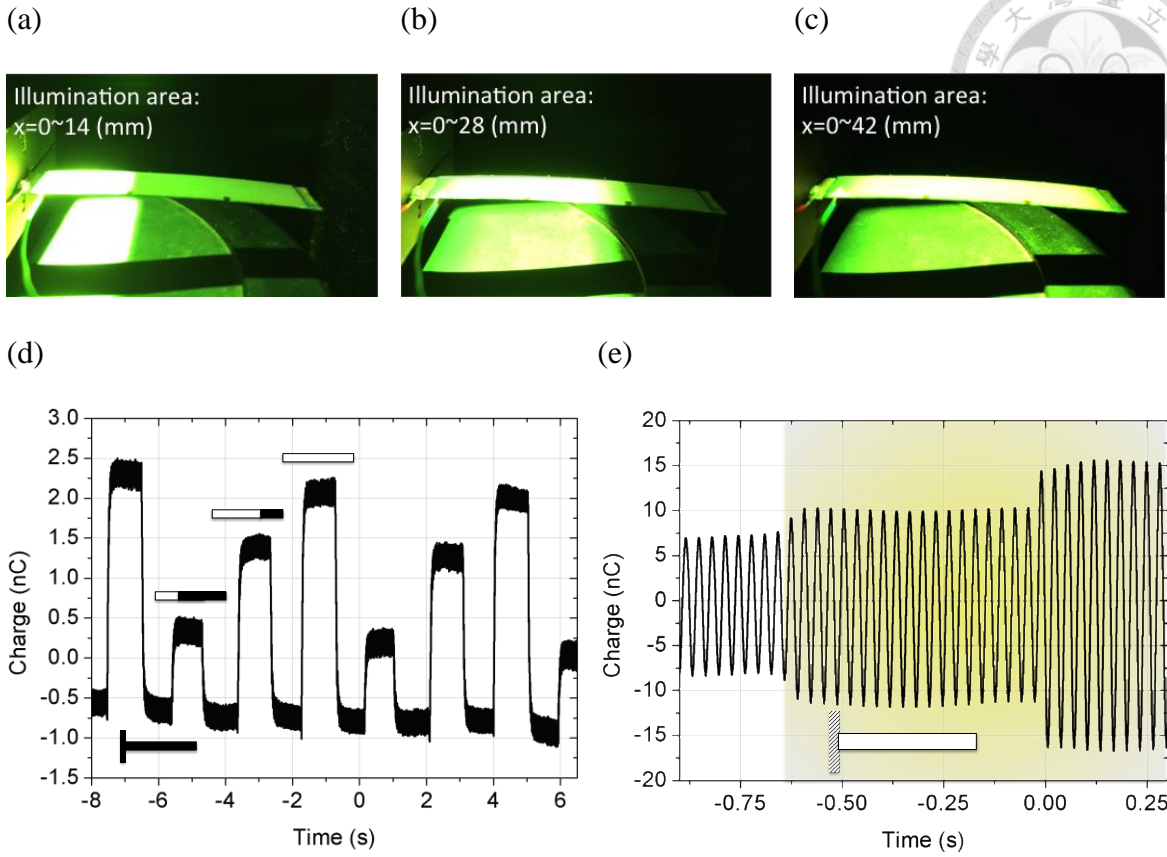


Figure 5-5. The illuminated beam from (a) 0~14 mm, (b) 0~28 mm, and (c) 0~42 mm. (d) The excitons of the static beam with light intensity (120 klux). (e) The charges of a vibration beam at 28.6 Hz, 0.22m N with light intensity (30 klux).

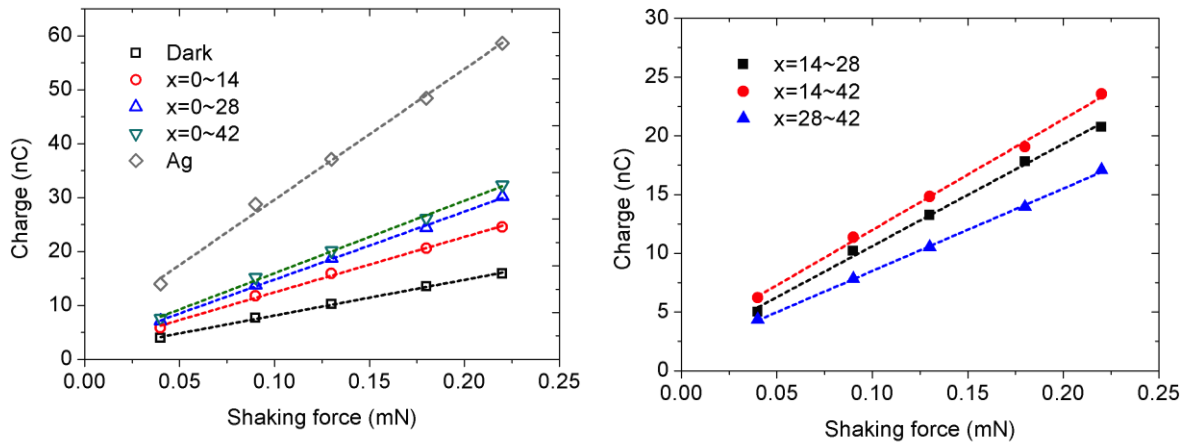
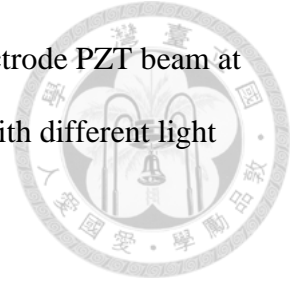


Figure 5-6. The obtained peak-to-peak charges coming from an Ag-electrode PZT beam at different shaking forces, and also charges from a PZT-TiOPc beam with different light illumination patterns.



### 5.3 Numerical calculation and curve fitting

For a general piezoelectric sensor (brass-PZT-Ag) mounted onto an one-dimensional cantilever plate configuration, the charges can be calculated by using (equation 5-2) [141, 142]. Symbol  $H$  and  $h$  are the thickness of the brass and PZT;  $b$  and  $L$  are the beam width and length;  $e_{31}$  is piezoelectric stress/ charge constant ( $5.3 \text{ C/m}^2$ );  $w$  is the displacement in x-direction; and  $s$  dielectric constant of PZT (2700). The strain of the one-dimensional plate induced corresponding charges through the piezoelectric constitutive law. In the ideal situation the sensing measurement is performed in a short-circuit situation ( $V=0$ ) [143], which means all of the charges can completely flow from one electrode to the other. But on the surfaces, the detected open-circuit voltage refers that some charges are prohibited from traveling from one electrode to the other.

$$\begin{aligned}
 Q &= -b \int_{l_0}^{l_1} e_{31} \frac{H+h}{2} \frac{\partial^2 w}{\partial x^2} dx + b \int_{l_0}^{l_1} \epsilon_r E_z dz \\
 &= \frac{b(H+h)e_{31}}{2} [\varphi(l_0) - \varphi(l_1)] - bL\epsilon_r \frac{V}{h}
 \end{aligned} \tag{5-2}$$

The simulation result shows at different sections, the “slop variation” and the “surface potential times area” are almost in the same ratio (Table 5-2). It is clear from (equation 2), the charge also follows this ratio that can be set as their average value for calculating charges from the measured  $Q_{0\sim 42}$  (Table 5-3) (Figure 5-7).

Table 5-2. Simulation of the ratio of the slope variation, surface potential at different sections.

Area (mm~mm)	0~14	0~28	0~42	14~28	14~42	28~42
Slope variation	4.38	7.23	8.08	2.85	3.85	1
Surface potential	4.72	3.53	2.69	2.63	1.88	1
Surface potential*Area	4.72	7.06	8.06	2.63	3.75	1
Average ratio	4.55	7.15	8.07	2.74	3.8	1

Table 5-3. The calculated charge at each section from measured  $Q_{0-42}$  with shaking forces 0.04 mN to 0.22 mN.

Calculated and measured charge (nC)	$Q_{0-14}$	$Q_{0-28}$	$Q_{0-42}$ (exp)	$Q_{14-28}$	$Q_{14-42}$	$Q_{28-42}$
Force= 0.04 mN	7.88	12.39	13.98	4.75	6.58	1.73
Force= 0.09 mN	16.23	25.50	28.78	9.77	13.55	3.57
Force= 0.13 mN	20.91	32.86	37.09	12.59	17.46	4.60
Force= 0.18 mN	27.31	42.92	48.44	16.45	22.81	6.00
Force= 0.22 mN	33.05	51.94	58.62	19.90	27.60	7.26

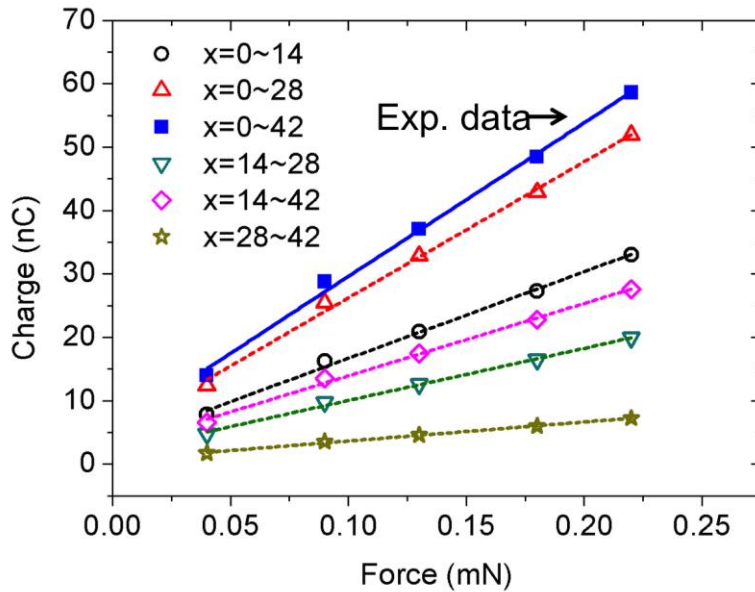


Figure 5-7. The calculated charge at each section of a piezoelectric sensor (brass-PZT-Ag).

For an optopiezoelectric sensor (brass-PZT-TiOPc/resin-ITO), the charges of each illuminated pattern can be represented by an empirical formula (equation 5-3). As TiOPc is a dielectric material, we can still get piezoelectric charges without light illumination (dark condition). The charges of the dark TiOPc/resin-ITO and silver are in a ratio of  $\alpha$ ; and  $\beta$  is the ratio of bright TiOPc/resin-ITO and silver. From (Figure 5-6), we can get  $\alpha=0.27$  and  $\beta=0.55$  ( $\beta/\alpha=2.03$ ). Moreover  $\beta/\alpha$  represents the value of impedance variation between illumination switching ( $Z_{bright}/Z_{dark}=2.05$ ) as indicated in (Figure 5-3). We thus can calculate the charges at different positions from (Table 5-3) and (Table 5-4) with  $\alpha=0.27$  and  $\beta=0.55$ , then also compared to experimental measurement (Figure 5-6) in (Figure 5-8).

$$Q_{TiOPc} = \beta \cdot Q_{Ag, \text{bright region}} + \alpha \cdot Q_{Ag, \text{dark region}} \quad (5-3)$$

Table 5-4. The piezoelectric peak-to-peak charges of a general sensor and PZT-TiOPc sensor.

Area (mm~mm)	Brass-PZT-Ag	Brass-PZT-TiOPc/ resin-ITO
Dark		$\alpha \cdot Q_{0\sim42}$
x=0~14	$Q_{0\sim14}$	$\beta \cdot Q_{0\sim14} + \alpha \cdot Q_{14\sim42}$
x=0~28	$Q_{0\sim28}$	$\beta \cdot Q_{0\sim28} + \alpha \cdot Q_{28\sim42}$
x=0~42	$Q_{0\sim42}$	$\beta \cdot Q_{0\sim42}$
x=14~28	$Q_{14\sim28}$	$\beta \cdot Q_{14\sim28} + \alpha \cdot (Q_{0\sim14} + Q_{28\sim42})$
x=14~42	$Q_{14\sim42}$	$\beta \cdot Q_{14\sim42} + \alpha \cdot Q_{0\sim14}$
x=28~42	$Q_{28\sim42}$	$\beta \cdot Q_{28\sim42} + \alpha \cdot Q_{0\sim28}$



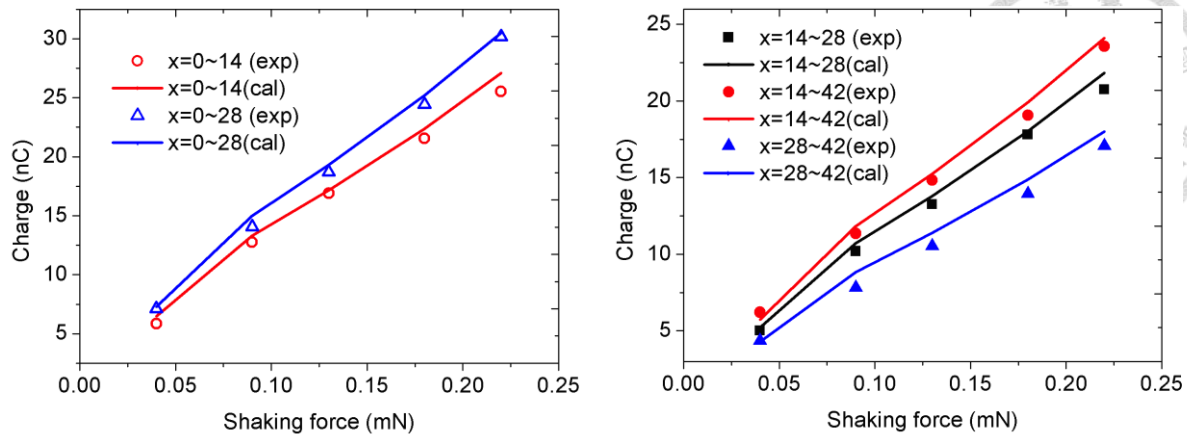


Figure 5-8. The charge from measurement and expectation with  $\alpha=0.27$  and  $\beta=0.55$ .

## 5.4 Discussion

For measuring the mechanical signal at certain position, the conventional strain gauge or bending sensor needs to be precisely pasted on the specimen surface. Our experimental results clearly demonstrated that the developed optopiezoelectric sensor (PZT-TiOPc) provides a more convenient and efficient measurement process to measure the bending slope (bending angle). Reducing the error coming from manual gluing those point sensors, this whole field optopiezoelectric sensor on the beam can act either as distributed sensor or a point sensor simply by changing the light illumination pattern. The charges coming from a light pattern can be inversely calculated to the signal coming from a piezoelectric sensor (PZT-metal) with parameters  $\alpha$  and  $\beta$ .

For example, (Table 5-5) shows the charges at the same position of a piezoelectric sensor can be calculated from the experimental optopiezoelectric charge, which is shown in (Figures 5-8) through (equation 5-3). Based on (equation 5-2) with the relative dielectric constant of PZT-TiOPc ( $\epsilon_r=812$ ) and the measured voltage (Table 5-6), the bending slope

can be calculated and compared to the simulation result listed in (Table 5-7) with a reasonable error.

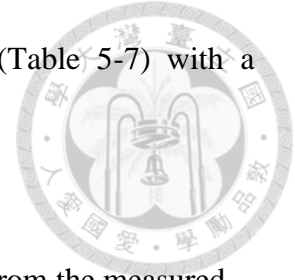


Table 5-5. The inversely calculated charges of a piezoelectric sensor from the measured charges of optopiezoelectric sensor.

<b>Charge (nC)</b>	<b>Q<sub>0-14</sub></b>	<b>Q<sub>0-28</sub></b>	<b>Q<sub>0-42</sub></b>	<b>Q<sub>14-28</sub></b>	<b>Q<sub>14-42</sub></b>	<b>Q<sub>28-42</sub></b>
Force= 0.04 mN	6.70	11.94	13.75	5.01	7.99	2.04
Force= 0.09 mN	15.76	23.75	27.64	9.31	11.46	2.57
Force= 0.13 mN	21.11	32.39	36.61	12.24	15.86	3.25
Force= 0.18 mN	26.83	42.13	47.52	16.03	21.48	4.66
Force= 0.22 mN	32.28	52.18	58.80	21.09	25.18	5.43

Table 5-6. The measured surface potential of the optopiezoelectric sensor in dark.

<b>Shaking force (mN)</b>	<b>Surface potential (mV)</b>
0.04	627
0.09	626
0.13	1021
0.18	1366
0.22	1680

Table 5-7. Comparison of the calculated and simulated bending slope.

<b>Slope difference</b> $\varphi(l_1) - \varphi(l_0)$	$\varphi(14) - \varphi(0)$		<b>Error</b> (%)	$\varphi(28) - \varphi(0)$		<b>Error</b> (%)
	<b>(Cal.)</b>	<b>(Sim.)</b>		<b>(Cal.)</b>	<b>(Sim.)</b>	
Force= 0.04 mN	1.50E-3	1.63E-3	7.98	2.45E-3	2.64E-3	7.20
Force= 0.09 mN	2.07E-3	2.21E-3	6.33	3.19E-3	3.56E-3	10.39
Force= 0.13 mN	3.09E-3	3.12E-3	2.83	4.80E-3	5.04E-3	6.61
Force= 0.18 mN	4.04E-3	4.39E-3	7.97	6.35E-3	7.08E-3	10.31
Force= 0.22 mN	4.93E-3	5.31E-3	7.16	7.84E-3	8.59E-3	8.73

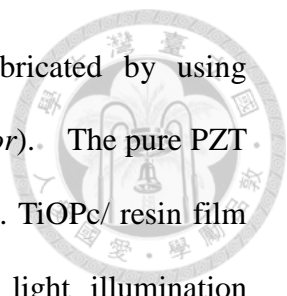
In conclusion, this newly developed PZT-TiOPc optopiezoelectric sensor is useful to measure the difference in bending slopes for various different bright sections. The bending angle can also be obtained if the slope starts from zero.

## Chapter 6. Conclusion and future work



### 6.1 Conclusion

Since 2011, the optopiezoelectric material and mechanism have been developed. Many studies continuously pursue material with fast and efficient responses with an attempt to identify more innovative applications. In this dissertation, I have tried to set a clear path for bridging microfluidic control and optopiezoelectric effect for optofluidics development. In *Chapter 3, A Living Worm Trapper by PZT Actuator*, the PZT efficiently control the two-phase fluidic field. The PZT plate was triggered with 175 DC voltage for pumping oil into water. The fingers-donut microfluidic channel was designed to enhance the opportunity of trapping *C. elegans* in water droplet. From the flow velocity simulation, the three fingers should spread in 45 degrees for the best PZT pumping efficiency. Then in *Chapter 4 and 5*, we discussed the optopiezoelectric performance with the developed composite materials in detail. In *Chapter 4, Optopiezoelectric Material*, the composite cantilever beam actuator, spiropyran/ liquid crystal- PZT, can be dynamic modulated with UV irradiation. The beam vibrating amplitude and resonant frequency were simultaneously increase and shift, respectively. Considering the system controllability and the compatibility with biological microfluidic device, we proposed the P(VDF-TrFE)/TiOPc as optopiezoelectric sensor. It's material physical properties; optical modulated piezoelectric effect and performance were discussed to get the optimal TiOPc content (10% w.t.). Although this single-layer sensor can be modulated by white light illumination, its sensing ability is not as good as pure P(VDF-TrFE) because TiOPc does not have piezoelectric effect. For getting a better sensing ability and increasing the light-



modulated effect, a double-layers optopiezoelectric sensor was fabricated by using PZT-TiOPc/ resin laminate (*Chapter 5, Optopiezoelectric Bending Sensor*). The pure PZT laminate performs sensing ability well, and the higher content 40% w.t. TiOPc/ resin film demonstrates better light-modulated ability. With localized white light illumination pattern, the bending slope or bending angle were measured and calculated by employing the proposed empirically calibrated theoretical model.

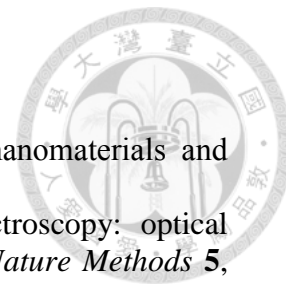
Overall, in this dissertation, the performance of piezoelectric sensors and actuators in microfluidic devices was investigated and verified. The optopiezoelectric effect was studied and its application was explored by examining the materials properties within the laminate. The actuator and sensor performance made from optopiezoelectric laminate were also examined and verified. These results provide us with useful and powerful suggestions for future optopiezoelectric fluidic development.

## **6.2 Future work**

The optopiezoelectric material provides us with an opportunity to explore many potential application in actuators and sensors. The most attractive advantage lies on the fact that they can be modulated by changing the illuminated light patterns. It is also clear that the photoconductivity and photosensitivity are important for the development of the laminates. Although TiOPc performs with appropriate efficiency, some electrons/ holes transition materials could be added for making larger impedance difference before and after illumination. Furthermore in the double-layers bending sensor, a flexible piezoelectric polymer such as PVDF might support the measurement on a non-flat surface in future applications. With this study and many expected future modification, we expect the

optopiezoelectric material can provide us with some innovative optopiezoelectric applications in mechanical, fluidic, and acoustic controlling systems.





## Reference

- [1] K. Ariga, T. Mori and J. P. Hill, "Mechanical control of nanomaterials and nanosystems," *Advanced Materials* **24**, 158-176 (2012).
- [2] K. C. Neuman and A. Nagy, "Single-molecule force spectroscopy: optical tweezers, magnetic tweezers and atomic force microscopy," *Nature Methods* **5**, 491-505 (2008).
- [3] D. Dulin, J. Lipfert, M. C. Moolman *et al.*, "Studying genomic processes at the single-molecule level: introducing the tools and applications," *Nature Reviews / Genetics* **14**, 9-22 (2013).
- [4] S. Vahabi, B. N. Salman and A. Javanmard "Atomic Force Microscopy Application in Biological Research: A Review Study," *Iranian Journal of Medical Sciences* **38**, 76-83 (2013).
- [5] D. J. Müller and Y. F. Dufre<sup>ne</sup>, "Atomic force microscopy: a nanoscopic window on the cell surface," *Trends in Cell Biology* **21**, 461-469 (2011).
- [6] F. Rico, A. Rigato, L. Picas *et al.*, "Mechanics of proteins with a focus on atomic force microscopy," *Journal of Nanobiotechnology* **11**, Suppl 1: S3-1-12 (2013).
- [7] T. Ando, T. Uchihashi and N. Kodera, "High-Speed AFM and Applications to Biomolecular Systems," *Annual Review of Biophysics* **42**, 393-414 (2013).
- [8] A. Alessandrini and P. Facci, "AFM: a versatile tool in biophysics," *Measurement Science And Technology* **16**, R65-R92 (2005).
- [9] C. Bustamante, S. B. Smith, J. Liphardt *et al.*, "Single-molecule studies of DNA mechanics," *Current Opinion in Structural Biology* **10**, 279-285 (2000).
- [10] F. Etoc, D. Lisse, Y. Bellaiche *et al.*, "Subcellular control of Rac-GTPase signalling by magnetogenetic manipulation inside living cells," *Nature Nanotechnology* **8**, 193-198 (2013).
- [11] Y. Seol and K. C. Neuman, "Magnetic tweezers for single-molecule manipulation," *Methods in Molecular Biology* **783**, 265-293 (2011).
- [12] J. Lipfert, J. W. J. Kerssemakers, T. Jager *et al.*, "Magnetic torque tweezers: measuring torsional stiffness in DNA and RecA-DNA filaments," *Nature Methods* **7**, 977-980 (2010).
- [13] T. R. Strick, J. F. Allemand, D. Bensimon *et al.*, "The elasticity of a single supercoiled DNA molecule," *Science* **271**, 1835-1837 (1996).
- [14] X. Li, C. C. Cheah, S. Hu *et al.*, "Dynamic trapping and manipulation of biological cells with optical tweezers," *Automatica* **49**, 1614-1625 (2013).
- [15] T. Asahi, T. Sugiyama and H. Masuhara, "Laser fabrication and spectroscopy of organic nanoparticles," *Accounts of Chemical Research* **41**, 1790-1798 (2008).
- [16] H. Misawa, M. Koshioka, K. Sasaki *et al.*, "Three-dimensional optical trapping and laser ablation of a single polymer latex particle in water," *Journal of Applied Physics* **70**, 3829-3836 (1991).
- [17] M. Geiselmann, M. L. Juan, J. Renger *et al.*, "Three-dimensional optical manipulation of a single electron spin," *Nature Nanotechnology* **8**, 175-179 (2013).
- [18] G. K. Kurup and A. S. Basu, "Optofluidic tweezers: manipulation of oil droplets with  $10^5$  greater force than optical tweezers," in *International Conference on Miniaturized Systems for Chemistry and Life Sciences*, ( $\mu$ TAS, Seattle, USA,

- 2011), pp. 263-265.
- [19] V. Pratap, N. Moumen and S. Subramanian, "Thermocapillary Motion of a Liquid Drop on a Horizontal Solid Surface," *Langmuir* **24**, 5185-5193 (2008).
- [20] K. D. Barton and S. Subramanian, "The Migration of Liquid Drops in a Vertical Temperature Gradient," *Journal of Colloid and Interface Science* **133**, 211-222 (1989).
- [21] H. Kasumi, Y. E. Solomentsev, S. A. Guelcher *et al.*, "Thermocapillary Flow and Aggregation of Bubbles on a Solid Wall," *Journal of Colloid and Interface Science* **232**, 111-120 (2000).
- [22] P. Y. Chiou, T. H. Wu, S. Park *et al.*, "Pulse Laser Driven Ultrafast Micro and Nanofluidic System," *Proceeding of SPIE* **7759**, 77590Z-1-8 (2010).
- [23] T. H. Wu, Y. Chen, S. Y. park *et al.*, "Pulsed laser triggered high speed microfluidic fluorescence activated cell sorter," *Lab on a Chip* **12**, 1378-1383 (2012).
- [24] Y. Xie, C. Zhao, Y. Zhao *et al.*, "Optoacoustic tweezers: a programmable, localized cell concentrator based on opto-thermally generated, acoustically activated, surface bubbles," *Lab on a Chip* **13**, 1772-1779 (2013).
- [25] S. Y. Park, T. H. Wu, Y. Chen *et al.*, "High-speed droplet generation on demand driven by pulse laser-induced cavitation," *Lab on a Chip* **11**, 1010-1012 (2011).
- [26] A. Q. Jian, K. Zhang, Y. Wang *et al.*, "Microfluidic flow direction control using continuous-wave laser," *Sensors and Actuators A* **188**, 329-334 (2012).
- [27] P. Y. Chiou, A. T. Ohta and M. C. Wu, "Massively parallel manipulation of single cells and microparticles using optical images," *Nature* **436**, 370-372 (2005).
- [28] P. Y. Chiou, H. Moon, H. Toshiyoshi *et al.*, "Light actuation of liquid by optoelectrowetting," *Sensors and Actuators A: Physical* **104**, 222-228 (2003).
- [29] P. Y. Chiou, Z. Chang and M. C. Wu, "Droplet Manipulation With Light on Optoelectrowetting Device," *Journal of Microelectromechanical Systems* **17**, 133-138 (2003).
- [30] T. M. Yu, S. M. Yang, C. Y. Fu *et al.*, "Integration of organic opto-electrowetting and poly(ethylene) glycol diacrylate (PEGDA) microfluidics for droplets manipulation," *Sensors and Actuators B* **180**, 35-42 (2013).
- [31] F. Krogmann, H. Qu, W. Mönch *et al.*, "Push/pull actuation using opto electrowetting," *Sensors and Actuators A* **141**, 499-505 (2008).
- [32] N. Inui, "Relationship between contact angle of liquid droplet and light beam position in optoelectrowetting," *Sensors and Actuators A* **140**, 123-130 (2007).
- [33] M. Vallet, B. Berge and L. Vovelle, "Electrowetting of water and aqueous solutions on poly (ethylene terephthalate) insulating films," *Polymer* **37**, 2465-2470 (1996).
- [34] H. S. Chuang, A. Kumar and S. Wereley, "Open optoelectrowetting droplet actuation," *Applied Physics Letters* **93**, 064104-1-3 (2008).
- [35] S. Y. Park, M. A. Teitell and E. P. Y. Chiou, "Single-sided continuous optoelectrowetting (SCOEW) for droplet manipulation with light patterns," *Lab on a Chip* **10**, 1655-1661 (2010).
- [36] Y. H. Lin, Y. W. Yang and M. H. Wu, "The assembly of cell-encapsulated microparticles in a microfluidic system using optically induced dielectrophoretic

- (ODEP) force for structurally-controllable cartilage tissue engineering,” in *International Symposium on Microchemistry and Microsystems*, (Seoul, Korea, 2011).
- [37] S. B. Huang, J. Chen, J. Wang *et al.*, “A New Optically-Induced Dielectrophoretic (ODEP) Force-Based Scheme for Effective Cell Sorting,” *International Journal of Electrochemical Science* **7**, 12656-12667 (2012).
- [38] S. M. Yang, S. Y. Tseng, H. P. Chen *et al.*, “Cell patterning via diffraction-induced optoelectronic dielectrophoresis force on an organic photoconductive chip,” *Lab on a Chip* **13**, 3893-3902 (2013).
- [39] C. H. Wang, Y. H. Lee, H. T. Kuo *et al.*, “Dielectrophoretically-assisted electroporation using light-activated virtual microelectrodes for multiple DNA transfection,” *Lab on a Chip* **14**, 592-601 (2014).
- [40] S. B. Huang, S. L. Liu, J. T. Li *et al.*, “Label-free Live and Dead Cell Separation Method Using a High-Efficiency Optically-Induced Dielectrophoretic (ODEP) Force-based Microfluidic Platform,” *International Journal of Automation and Smart Technology* **4**, 83-91 (2014).
- [41] J. K. Valley, S. N. Pei, A. Jamshidi *et al.*, “A unified platform for optoelectrowetting and optoelectronic tweezers,” *Lab on a Chip* **11**, 1292-1297 (2011).
- [42] P. H. Cazorla, O. Fuchs, M. Cochet *et al.*, “Piezoelectric micro-pump with PZT thin film for low consumption microfluidic devices,” *Procedia Engineering* **87**, 488-491 (2014).
- [43] A. Bransky, N. Korin, M. Khoury *et al.*, “A microfluidic droplet generator based on a piezoelectric actuator,” *Lab on a Chip* **9**, 516-520 (2009).
- [44] W. Zhang and Richard E. Eitel, “An integrated multilayer ceramic piezoelectric micropump for microfluidic systems,” *Journal of Intelligent Material Systems and Structures* **24**, 1637-1646 (2013).
- [45] Y. B. Ham, W. S. Seo, S. J. Oh *et al.*, “Development of a Piezoelectric Pump for a Highly-precise Constant Flow Rate,” *Journal of the Korean Physical Society* **57**, 873-876 (2010).
- [46] E. Nakamachi, H. Hwang, N. Okamoto *et al.*, “Development of a micropump for Bio-MEMS using a new biocompatible piezoelectric material  $MgSiO_3$ ,” *Journal of Micro/Nanolithography, MEMS, and MOEMS* **10**, 033013-1-7 (2011).
- [47] C. H. Chen, S. H. Cho, F. Tsai, *et al.*, “Microfluidic cell sorter with integrated piezoelectric actuator,” *Biomed Microdevices* **11**, 1223-1231 (2009).
- [48] T. A. House, V. H. Lieu and D. T. Schwartz, “A model for inertial particle trapping locations in hydrodynamic tweezers arrays,” *Journal of Micromechanics and Microengineering* **24**, 045019-1-8 (2014).
- [49] R. H. W. Lam and W. J. Li, “A Digitally Controllable Polymer-Based Microfluidic Mixing Module Array,” *Micromachines* **3**, 279-294 (2012).
- [50] D. Ahmed, X. Mao, J. Shi *et al.*, “A millisecond micromixer via single-bubble-based acoustic streaming,” *Lab on a Chip* **9**, 2738-2741 (2009).
- [51] J. Sirohi and I. Chopra, “Fundamental Understanding of Piezoelectric Strain Sensors,” *Journal of Intelligent Material Systems and Structures* **11**, 246-257 (2000).
- [52] K. Takashima, S. Horie, T. Mukai *et al.*, “Piezoelectric properties of



- vinylidene fluoride oligomer for use in medical tactile sensor applications,” *Sensors and Actuators A* **144**, 90-96 (2008).
- [53] F. Li, W. Liu, C. Stefanini *et al.*, “A Novel Bioinspired PVDF Micro/Nano Hair Receptor for a Robot Sensing System,” *Sensors* **10**, 994-1011 (2010).
- [54] J. S. Lee, K. Y. Shin, O. J. Cheong *et al.*, “Highly Sensitive and Multifunctional Tactile Sensor Using Free-standing ZnO/ PVDF Thin Film with Graphene Electrodes for Pressure and Temperature Monitoring,” *Scientific Reports* **5**, 7887-1-8 (2015).
- [55] W. Park, J. H. Yang, C. G. Kang *et al.*, “Characteristics of a pressure sensitive touch sensor using a piezoelectric PVDF-TrFE/MoS<sub>2</sub> stack,” *Nanotechnology* **24**, 475501-1-6 (2013).
- [56] E. F. Crawley, “Intelligent Structures for Aerospace: A Technology Overview and Assessment,” *AIAA Journal* **32**, 1689-1699 (1994).
- [57] D. Sun, L. Tong, and S. N. Atluri, “Effects of piezoelectric sensor/actuator debonding on vibration control of smart beams,” *International Journal of Solids and Structures* **38**, 9033-9051 (2001).
- [58] H. S. Tzou, “Distributed sensing and controls of flexible plates and shells using distributed piezoelectric elements,” *Journal of Wave-Material Interface* **4**, 11-29 (1989).
- [59] J. Qiu and J. Tani, “Vibration control of a cylindrical shell using distributed piezoelectric sensors and actuators,” *Journal of Intelligent Material System and Structures* **6**, 474-481 (1995).
- [60] E. K. Dimitriadis and C. R. Fuller, “Active Control of Sound Transmission Through Elastic Plates Using Piezoelectric Actuators,” *AIAA Journal* **29**, 1771-1777 (1991).
- [61] M. S. Kozie ń and Jerzy Wiciak, “Reduction of Structural Noise Inside Crane Cage by Piezoelectric Actuators-FEM Simulation,” *Archives of Acoustics* **33**, 643-652 (2008).
- [62] F. dell’Isola, F. Vestroni and S. Vidoli, “Structural-Damage Detection by Distributed Piezoelectric Transducers and Tuned Electric Circuits,” *Research in Nondestructive Evaluation* **16**, 101-117 (2010).
- [63] D. F. Wang, Y. Suzuki, Y. Suwa *et al.*, “Integrated piezoelectric direct current sensor with actuating and sensing elements applicable to two-wire dc appliances,” *Measurement Science and Technology* **24**, 125109-1-5 (2013).
- [64] C. K. Lee, “Theory of laminated piezoelectric plates for the design of distributed sensors and actuators-part one,” *The Journal of the Acoustical Society of America* **87**, 1144-1158 (1990).
- [65] C. K. Lee and F. C. Moon, “Modal Sensors/Actuators,” *Journal of Applied Mechanics* **57**, 434-441 (1990).
- [66] C. K. Lee, W. W. Chiang and T. C. O’Sullivan, “Piezoelectric modal sensor/actuator pairs for critical active damping vibration control,” *The Journal of the Acoustical Society of America* **90**, 374-384 (1991).
- [67] A. Donoso and J. C. Bellido “Distributed piezoelectric modal sensors for circular plates,” *Journal of Sound and Vibration* **319**, 50-57 (2009).
- [68] Y. H. Hsu and C. K. Lee, “Miniature Free-fall Sensors,” *Journal of Intelligent Material Systems and Structures* **12**, 223-228 (2001).

- [69] Y. H. Hsu and C. K. Lee, "On the Autonomous Gain and Phase Tailoring Transfer Functions of Symmetrically Distributed Piezoelectric Sensors," *Journal of Vibration and Acoustics* **126**, 528-536 (2004).
- [70] S. Oberti, A. Neild, R. Quach *et al.*, "The use of acoustic radiation forces to position particles within fluid droplets," *Ultrasonics* **49**, 47-52 (2009).
- [71] K. T. Chen, C. K. Chang, H. L. Kuo *et al.*, "Optically Defined Modal Sensors Incorporating Spiropyran-Doped Liquid Crystals with Piezoelectric Sensors," *Sensors* **11**, 1810-1818 (2011).
- [72] K. T. Chen, S. D. Huang, Y. H. Chien *et al.*, "Development of an optically modulated piezoelectric sensor/actuator based on titanium oxide phthalocyanine thin film," *Smart Materials and Structures* **21**, 115025-1-8.
- [73] 黃旭鐸, "以 TiOPc/ 壓電圓板設計可撓鏡的研發," 國立台灣大學工程科學及海洋工程研究所碩士論文, 2013.
- [74] P. W. Wang, T. C. Chang and C. K. Lee, "Acoustic Research and Control of Piezoelectric Speakers Using A Spatially Modulated TiOPc/Piezo Buzzer Actuator," in *International Symposium on Optomechatronic Technologies*, (Seattle, USA, 2014).
- [75] H. Li, Z. D. Deng, Y. Yuan *et al.*, "Design Parameters of a Miniaturized Piezoelectric Underwater Acoustic Transmitter," *Sensors* **12**, 9098-9109 (2012).
- [76] C. C. Chang and T. E. Hsu, "The Study of Micro-bridge Structure PZT Underwater Ultrasonic Sensors with Al Sacrificial Layer," *Oceans*, (Taipei, Taiwan, 2014).
- [77] L. Su, L. Zou, C. C. Fong *et al.*, "Detection of cancer biomarkers by piezoelectric biosensor using PZT ceramic resonator as the transducer," *Biosensors and Bioelectronics* **46**, 155-161(2013).
- [78] I. H. Hwang and J. H. Lee, "Self-actuating biosensor using a piezoelectric cantilever and its optimization," *Journal of Physics: Conference Series* **34**, 362-367 (2006).
- [79] C. Dagdeviren, B. D. Yang, Y. Su *et al.*, "Conformal piezoelectric energy harvesting and storage from motions of the heart, lung, and diaphragm," *Proceedings of the National Academy of Sciences of the United States of America* **111**, 1927-1932 (2014).
- [80] S. C. Lin, B. S. Lee, W. J. Wu *et al.*, "Multi-cantilever piezoelectric MEMS generator in energy harvesting," *IEEE International Ultrasonics Symposium Proceedings*, 755-758 (2009).
- [81] Measurement Specialties, Inc., "Piezo Film Sensors Technical Manual," (1999).
- [82] M. Nasir, H. Matsumoto, M. Minagawa *et al.*, "Preparation of PVDF/PMMA Blend Nanofibers by Electrospray Deposition: Effects of Blending Ratio and Humidity," *The Society of Polymer Science* **41**, 402-406 (2009).
- [83] C. Seoul, Y. T. Kim and C. K. Baek, "Electrospinning of Poly(vinylidene fluoride)/ Dimethylformamide Solutions with Carbon Nanotubes," *Journal of Polymer Science: Part B: Polymer Physics* **41**, 1572-1577 (2003).
- [84] J. B. Lando, H. G. Olf and H. G. Peterlin, "Nuclear magnetic resonance and x-ray determination of the structure of poly(vinylidene fluoride)," *Journal of*

- Polymer Science Part A-1: Polymer Chemistry* **4**, 941-951 (1966).
- [85] R. Hasegawa, Y. Takahashi, Y. Chatani *et al.*, “Crystal Structures of Three Crystalline Forms of Poly(vinylidene fluoride),” *Polymer Journal* **3**, 600-610 (1972).
- [86] B. P. Neese “Investigations of Structure-Property Relationships to Enhance the Multifunctional Properties of PVDF-Based Polymers,” The Pennsylvania State University, Department of Materials Science and Engineering, Doctor of Philosophy, 2009.
- [87] E. D. Weil, *Phosphorus-Containing Polymers and Oligomers- Encyclopedia of Polymer Science and Technology*. (J. Wiley & Sons, Inc.; New York, 2006).
- [88] C. A. Nguyen, P. S. Lee, W. A. Yee *et al.*, “Enhanced functional and structural characteristics of poly(vinylidene-trifluoroethylene) copolymer thin films by corona poling,” *Journal of The Electrochemical Society* **154**, G224-G228 (2007).
- [89] Z. G. Zeng, G. D. Zhu, L. Zhang *et al.*, “Effect of crystallinity on polarization fatigue of ferroelectric P(VDF-TrFE) copolymer films,” *Chinese Journal of Polymer Science* **27**, 479-485 (2009).
- [90] T. Furukawa, M. Date, E. Fukada *et al.*, “Ferroelectric behavior in the copolymer of vinylidene fluoride and trifluoroethylene,” *Japanese Journal of Applied Physics* **19**, L109-L112 (1980).
- [91] Z. Chen, K. Y. Kwon and X. Tan, “Integrated IPMC/PVDF sensory actuator and its validation in feedback control,” *Sensors and Actuators A: Physical* **144**, 231-241 (2008).
- [92] B. Ploss, W. Y. Ng, H. L. W. Chan *et al.*, “Poling study of PZT/ P(VDF-TrFE) composites,” *Composites Science and Technology* **61**, 957-962 (2001).
- [93] E. Mele, D. Pisignano, M. Varda *et al.*, “Smart photochromic gratings with switchable wettability realized by green-light interferometry,” *Applied Physics Letters* **88**, 203124-1-3 (2006).
- [94] A. Athanassiou, M. Lygeraki, D. Pisignano *et al.*, “Photocontrolled variations in the wetting capability of photochromic polymers enhanced by surface nanostructuring,” *Langmuir* **22**, 2329-2333 (2006).
- [95] H. B. Laurent and H. Dürr, “Organic photochromism,” *Pure and Applied Chemistry* **73**, 639-665 (2001).
- [96] R. Byrne and D. Diamond, “Chemo/bio-sensor networks,” *Nature Materials* **5**, 421-424 (2006).
- [97] Q. Shen, Y. Cao, S. Liu *et al.*, “Conformation-induced electrostatic gating of the conduction of spiropyran-coated organic thin-film transistors,” *The Journal of Physical Chemistry C* **113**, 10807-10812 (2009).
- [98] Z. Walsh, S. Scarmagnani, F. B. López *et al.*, “Photochromic spiropyran monolithic polymers: Molecular photo-controllable electroosmotic pumps for micro-fluidic devices,” *Sensors and Actuators B* **148**, 569-576 (2010).
- [99] X. Zhang, Q. Zhou, H. Liu *et al.*, “UV light induced plasticization and light activated shape memory of spiropyran doped ethylene-vinyl acetate copolymers,” *Soft Matter* **10**, 3748-3754 (2014).
- [100] F. B. Lopez, S. Scarmagnani, Z. Walsh *et al.*, “Spiropyran modified micro-fluidic chip channels as photonically controlled self-indicating system for metal ion accumulation and release,” *Sensors & Actuators: B. Chemical* **140**,

- 295-303 (2009).
- [101] M. Mayukh, "Near-IR Absorbing Phthalocyanine Derivatives As Materials For Organic Solar Cells," The University of Arizona, Department of Chemistry and Biochemistry, Doctor of Philosophy (2011).
- [102] L. Li, Q. Tang, H. Li *et al.*, "An Ultra Closely  $\pi$ -Stacked Organic Semiconductor for High Performance Field-Effect Transistors," *Advanced Materials* **19**, 2613–2617 (2007).
- [103] W. Chao, X. Zhang, C. Xiao *et al.*, "An excellent single-layered photoreceptor composed of oxotitanium phthalocyanine nanoparticles and an insulating resin," *Journal of Colloid and Interface Science* **325**, 198-202 (2008).
- [104] K. Y. Law, "Organic photoconductive materials: recent trends and developments," *Chemical Reviews* **93**, 449-486 (1993).
- [105] C. J. Lee, J. H. Park and J. Park, "Synthesis of bamboo-shaped MWCNT using thermal CVD," *Chemical Physics Letters* **323**, 560-565 (2000).
- [106] K. Ogawa, J. Yao, H. Yonehara *et al.*, "Chemical behaviour of oxotitanium(IV) phthalocyanine (OTiPc) solutions associated with the preparation of OTiPC monolayers and multilayers," *Journal of Materials Chemistry* **6**, 143-147 (1996).
- [107] S. M. Yang, T. M. Yu, H. P. Huang *et al.*, "Dynamic manipulation and patterning of microparticles and cells by using TiOPc-based optoelectronic dielectrophoresis," *Optics Letters* **35**, 1959-1961 (2010).
- [108] S. M. Yang, T. M. Yu, M. H. Liu *et al.*, "Moldless PEGDA Based Optoelectrofluidic Platform for Microparticle Selection," *Advances in Optoelectronics* **2011**, 1-8 (2011).
- [109] S. M. Yang, T. M. Yu, H. P. Huang *et al.*, "Dynamic Pico-Liter Bubble Manipulation via Tiopc-Based Light-Induced Dielectrophoresis," in *14<sup>th</sup> International Conference on Miniaturized Systems for Chemistry and Life Sciences*, (Groningen, The Netherlands, 2010).
- [110] L. Heng, D. Tian, L. Chen *et al.*, "Local photoelectric conversion properties of titanyl-phthalocyanine (TiOPc) coated aligned ZnO nanorods," *Chemical Communications* **46**, 1162-1164 (2010).
- [111] M. G. Walter, A. B. Rudine and C. C. Wamser, "Porphyrins and phthalocyanines in solar photovoltaic cells," *Journal of Porphyrins and Phthalocyanines* **14**, 759-792 (2010).
- [112] K. Vasseur, B. P. Rand, D. Cheyons *et al.*, "Correlating the Polymorphism of Titanyl Phthalocyanine Thin Films with Solar Cell Performance," *The Journal of Physical Chemistry Letters* **3**, 2395-2400 (2012).
- [113] <https://tuebingen.mpg.de/en/news-press/press-releases/detail/how-the-modular-structure-of-proteins-permits-evolution-to-move-forward.html>.
- [114] R. Kerr, V. Lev-Ram, G. Baird *et al.*, "Optical imaging of calcium transients in neurons and pharyngeal muscle of *C. elegans*," *Neuron* **26**, 583-594 (2000).
- [115] M. B. Goodman, D. H. Hall, L. Avery *et al.*, "Active currents regulate sensitivity and dynamic range in *C. elegans* neurons," *Neuron* **20**, 763-772 (1998).
- [116] J. A. Lewis, C. H. Wu, H. Berg *et al.*, "The Genetics of Levamisole Resistance in the Nematode *CAENORHABDITIS ELEGANS*," *Genetics* **95**, 905-928 (1980).
- [117] K. Chung, M. Zhan, J. Srinivasan *et al.*, "Microfluidic chamber arrays for whole-organism behavior-based chemical screening," *Lab on a Chip* **11**,

- 3689-3697 (2011).
- [118] X. Ai, W. Zhuo, Q. Liang *et al.*, “A high-throughput device for size based separation of *C. elegans* developmental stages,” *Lab on a Chip* **14**, 1746-1752 (2014).
- [119] K. Chung, M. M. Crane and H. Lu, “Automated on-chip rapid microscopy, phenotyping and sorting of *C. elegans*,” *Nature Methods* **5**, 637-643 (2008).
- [120] C. L. Gilleland, C. B. Rohde, F. Zeng *et al.*, “Microfluidic immobilization of physiologically active *Caenorhabditis elegans*,” *Nature Protocols* **5**, 1888-1902 (2010).
- [121] T. V. Chokshi, A. Ben-Yakar and N. Chronis, “CO<sub>2</sub> and compressive immobilization of *C. elegans* on-chip,” *Lab on a Chip* **9**, 151-157 (2009).
- [122] S. E. Hulme, S. S. Shevkoplyas, J. Apfeld *et al.*, “A microfabricated array of clamps for immobilizing and imaging *C. elegans*,” *Lab on a Chip* **7**, 1515-1523 (2007).
- [123] H. S. Chuang, D. M. Raizen, A. Lamb *et al.*, “Dielectrophoresis of *Caenorhabditis elegans*,” *Lab on a Chip* **11**, 599-604 (2011).
- [124] X. Ding, S. C. S. Lin, B. Kiraly *et al.*, “On-chip manipulation of single microparticles, cells, and organisms using surface acoustic waves,” *Proceedings of the National Academy of Sciences of the United States of America (PNAS)* **28**, 11105-11109 (2012).
- [125] A. H. Meitzler, H. F. Tiersten, A. W. Warner *et al.*, “ANSI/IEEE Std 176-1987 IEEE Standard on Piezoelectricity.” (Piscataway, NJ: The Institute of Electrical and Electronics Engineers) (1987).
- [126] N. N. Rogacheva, *The theory of piezoelectric shells and plates.* (CRC Press; England, 1994).
- [127] J. Yang, *The mechanics of piezoelectric structures.* (World Scientific Publishing Co Pte Ltd; Singapore, 2006).
- [128] D. A. Edwards, H. Brenner, and D. T. Wasan, *Interfacial Transport Processes and Rheology.* (Butterworth-Heinemann; Massachusetts, 1991).
- [129] J. Sznitman, X. Shen, P. K. Purohit *et al.*, “Swimming Behavior of the Nematode *Caenorhabditis elegans*: Bridging Small-Scale Locomotion with Biomechanics,” *IFMBE Proceedings* **31**, 29-32 (2010).
- [130] A. Vidal-Gadea, S. Topper, L. Young *et al.*, “*Caenorhabditis elegans* selects distinct crawling and swimming gaits via dopamine and serotonin,” *Proceedings of the National Academy of Sciences of the United States of America (PNAS)* **108**, 17504–17509 (2011).
- [131] K. Uchino, “Introduction to Piezoelectric Actuators and Transducers.” (International Center for Actuators and Transducers, Penn State University) (2003).
- [132] M. Deshpande, and L. Saggere, “An analytical model and working equations for static deflections of a circular multi-layered diaphragm-type piezoelectric actuator,” *Sensors and Actuators A: Physical* **136**, 673-689 (2007).
- [133] C. K. Lee, G. Y. Wu, Thomas C. T. *et al.*, “A High Performance Doppler Interferometer for Advanced Optical Storage Systems,” *Japanese Journal of Applied Physics* **38**, 1730-1741 (1999).
- [134] W. J. Wu, C. K. Lee, and C. T. Hsieh, “On the Signal Processing Algorithms for

- Doppler Effect Based Nanometer Positioning Systems,” *Japanese Journal of Applied Physics* **38**, 1725-1729 (1999).
- [135] E. Samoylova, L. Ceseracciu, M. Allione *et al.*, “Photoinduced variable stiffness of spiropyran-based composites,” *Applied Physics Letters* **99**, 201905-1-3 (2011).
- [136] L.O. Faria and R.L. Moreira, “Infrared spectroscopic investigation of chain conformations and interactions in P(VDF-TrFE)/PMMA blends,” *Journal of Polymer Science Part B: Polymer Physics* **38**, 34-40 (2000).
- [137] Z.Y. Wang, H.Q. Fan, K.H. Su *et al.*, “Structure, phase transition and electric properties of poly(vinylidene fluoride-trifluoroethylene) copolymer studied with density functional theory,” *Polymer* **48**, 3226-3236 (2007).
- [138] H.J. Lee, W.S. Kim, S.H. Park *et al.*, “Effects of nanocrystalline porous TiO<sub>2</sub> films on interface adsorption of phthalocyanines and polymer electrolytes in dye-sensitized solar cells,” *Macromolecular Symposia* **235**, 230-236 (2006).
- [139] D. Dündar, H. Can, D. Atilla *et al.*, “Photoconductive novel mesomorphic oxotitanium phthalocyanines,” *Polyhedron* **27**, 3383-3390 (2008).
- [140] C. K. Lee, “Piezoelectric Laminates for Torsional and Bending Modal Control: Theory and Experiment,” Cornell University, Department of Theoretical and Applied Mechanics, Doctor of Philosophy, 1987.
- [141] F. Lu, H. P. Lee and S. P. Lim, “Modeling and analysis of micro piezoelectric power generators for micro- electromechanical-systems applications,” *Smart Materials and Structures* **13**, 57-63 (2004).
- [142] A. T. Mineto, M. P. de S. Braun, H. A. Navarro *et al.*, “Modeling of a One-dimensional cantilever plate for Piezoelectric Energy Harvesting,” *Proceedings of the 9th Brazilian Conference on Dynamics Control and their Applications*, 599-605 (2010).
- [143] S. Yang and B. Ngoi, “General sensor equation and actuator equation for the theory of laminated piezoelectric plates,” *Smart Materials and Structures* **8**, 411-415 (1999).



## List of Publications

### Journal paper

1. Chih-Kung Lee\*, Po-Cheng Lai, **Wen-Chi Chang**, Yi-Ching Kuo, Pei-I Tsai, Ming-Han Chung and Julie T. Lee, "Interdisciplinary Research Drivers and Serendipity Factor: An Applied Mechanics Perspective," *International Journal of Automation and Smart Technology* **4**, 228-237 (2014).
2. **Wen-Chi Chang**, Wen-Ching Ko, Jay Shieh, Chih-Ting Lin, An-Bang Wang, Chih-Kung Lee\*, "A photo-sensitive piezoelectric composite material of poly(vinylidene fluoride- trifluoroethylene) and titanium oxide phthalocyanine," *Materials Chemistry and Physics* **149-150**, 254-260 (2014).
3. **Wen-Chi Chang**, Wen-Ching Ko, Han-Lung Chen, Chih-Ting Lin, An-Bang Wang, Chih-Kung Lee\*, "Photoconductive Piezoelectric Polymer Made From a Composite of P(VDF-TrFE) and TiOPc," *Ferroelectrics* **446**, 9-17 (2013).
4. Kuan-Ting Chen, Shiu-Duo Huang, Ying-Heng Chien, **Wen-Chi Chang**, Chih-Kung Lee\*, Development of an optically modulated piezoelectric sensor/actuator based on titanium oxide phthalocyanine thin film, *Smart Material Structures* **21**, 115025.1-115025.8 (2012).

### Conference paper

1. **Wen-Chi Chang**, Jan. G. Korvink, Chih-Kung Lee\*, "A living worm trapper by PZT actuator," *19<sup>th</sup> Nano Engineering and Microsystem Technology Conference*, Taipei, Taiwan (Aug. 2015)
2. **Wen-Chi Chang**, Po-Han Chen, Chih-Ting Lin, An-Bang Wang, and Chih-Kung Lee\*, "Development of a Photoresponsive and Electrostrictive Material from P(VDF- TrFE- CFE) and TiOPc Composite," *Materials Research Society*, Boston, USA. (Dec. 2013).
3. **Wen-Chi Chang**, Wen-Ching Ko, Han-Lung Chen, Chih-Ting Lin, An-Bang Wang, Chih-Kung Lee\*, Development of a Photoconductive Piezoelectric Material Made from Composite of P(VDF-TrFE) and TiOPc, *International Symposium on Applications of Ferroelectrics*, Aveiro, Portugal (Jul. 2012).
4. **Wen-Chi Chang**, Yu-Chi Chen, Chih-Jen Chien, An-Bang Wang, Chih-Kung Lee\*, "Integrating single-point vibrometer and full-field electronic speckle pattern interferometer to evaluate a micro-speaker," *SPIE Smart Structures/NDE*, San Diego, USA. (Mar. 2011).
5. Yu-Chi Chen, Te-Hsun Chen, Chih-Jen Chien, **Wen-Chi Chang**, Chih-Chiang Cheng, Wen-Ching Ko, Kuang-Chong Wu, Chih-Kung Lee\*, "Simulation and experimental study of flexible electret-based loudspeaker vibration modes by electronic speckle pattern interferometry," *SPIE The International Society for Optics and Photonics*, San Francisco, USA. (Aug. 2010).
6. Yu-Chi Chen, Chih-Jen Chien, **Wen-Chi Chang**, Wen-Ching ko, Chang-Ho Liou, Wen-Jong Wu, Pei-Zen Chang, Chih-Kung Lee\*, "Design and experimental verification of cell actuators in a flexible electret-based loudspeaker system," *21st International Conference on Adaptive Structures and Technologies (ICAST)*, Pennsylvania, USA. (Oct. 2010).